Doctoral Dissertations

Student Scholarship

Winter 2011

Statistical study of oxygen+ transport from the cusp to the plasmasheet

Jing Liao
University of New Hampshire, Durham

STATISTICAL STUDY OF O$^+$ TRANSPORT FROM THE CUSP TO THE PLASMASHEET

BY

Jing Liao

B.S. Physics, Nanjing University (2005)

DISSERTATION

Submitted to the University of New Hampshire

in Partial Fulfillment of

the Requirements for the Degree of

Doctor of Philosophy

in

Physics

December, 2011

UMI Number: 3500788

UMI®

Dissertation Publishing
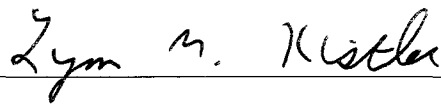
ProQuest®

This dissertation has been examined and approved.

Thesis Director, Lynn M. Kistler

Professor, Department of Physics

Eberhard Möbius

Professor, Department of Physics

Richard Kaufmann

Emeritus Professor, Department of Physics

Terry Forbes

Research Professor, Department of Physics

Karsten Pohl

Associate Professor, Department of Physics

10 August 2011

Date

DEDICATION

To my husband Lorenzo Zana, my son Leonardo Zana, my mother Tan Xiuying and my father Liao Ping

.

ACKNOWLEDGMENTS

TABLE OF CONTENTS

LIST OF TABLES

LIST OF FIGURES

ABSTRACT

STATISTICAL STUDY OF O^+ TRANSPORT FROM THE CUSP TO THE PLASMASHEET

by

Jing Liao

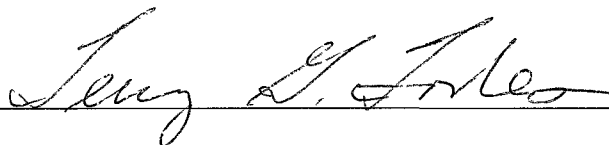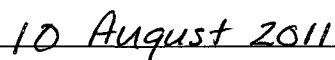University of New Hampshire, December, 2011

Using Cluster/CODIF data, we have determined the occurrence frequency of the cusp-source O^+ in the magnetotail to determine where and when it is observed. The results show that the probability to observe O^+ along the transport path is high even during nonstorm times, although, as expected, the highest probability is found during storm times. In addition to the outflow rate increasing, the transport path itself also changes during storm times, bringing more O+ to the near-earth plasma sheet. Interplanetary magnetic field (IMF) magnitude is the most effective driver for bringing O^+ into the near-Earth lobes. It was also found that when IMF By is positive, O^+ from the northern cusp/cleft tends to stream towards the dawnside while O^+ from the south is observed on the duskside. The transport path for negative IMF By is more symmetric, but shows some evidence for a reversed asymmetry when IMF By is strongly negative. The asymmetry most likely results from the combination of the convection driven by the solar wind and the coupling with the ionosphere. By comparing the normalized distributions of the cusp outflow and the streaming O^+ in the magnetotail we show that the increase in the energy of the streaming O^+ in the tail lobes is mainly due to the velocity filter effect, not due to acceleration. O^+ entering from the lobe into the plasma sheet boundary layer, however, has been accelerated. A case study shows that most of the velocity increase is due to $E \times B$ drift, but additional acceleration along the electric field is also found. The probability to observe streaming O^+ decreases steeply during the declining phase of solar cycle 23 and increases again at the

start of solar cycle 24. The reduction factor is much larger in the tail lobes than in the polar cap, due to a change in the transport path.

Chapter 1

INTRODUCTION

The plasma in the Earth's magnetosphere comes from two major sources, the solar wind and the ionosphere. Studies have shown that O^+ from the ionosphere not only is an important source for magnetosphere plasma but also plays a significant, even controlling, role in the magnetosphere dynamics. In this thesis, we will discuss how O^+ ions are transported from the cusp into the lobes and then enter the plasmasheet using a statistical study of the streaming O^+ observations. We will discuss the theoretical background in this chapter and give a brief introduction to the instrumentation in chapter 2. In chapter 3, we will present the methodology of the automated identification program for the streaming O^+ and the statistics of the identification results. In chapters 4, 5 and 6, we will present our discussion about the spatial distribution of the transport path and its dependence on geomagnetic activity, the acceleration of O^+ along the transport path, and the transport path dependence on the solar cycle. A brief summery will be given in chapter 7.

1.1 Background

Solar wind is a flow of energetic ionized particles, mainly H^+ and He^{++}, that streams continuously from the Sun at a speed of 400 km/s on average. The interplanetary magnetic field (IMF) is a part of the Sun's magnetic field that is then carried into interplanetary space by the solar wind. Hence, IMF is said to be "frozen in" to the solar wind plasma, which is usually around several nT but can reach tens of nT occasionally.
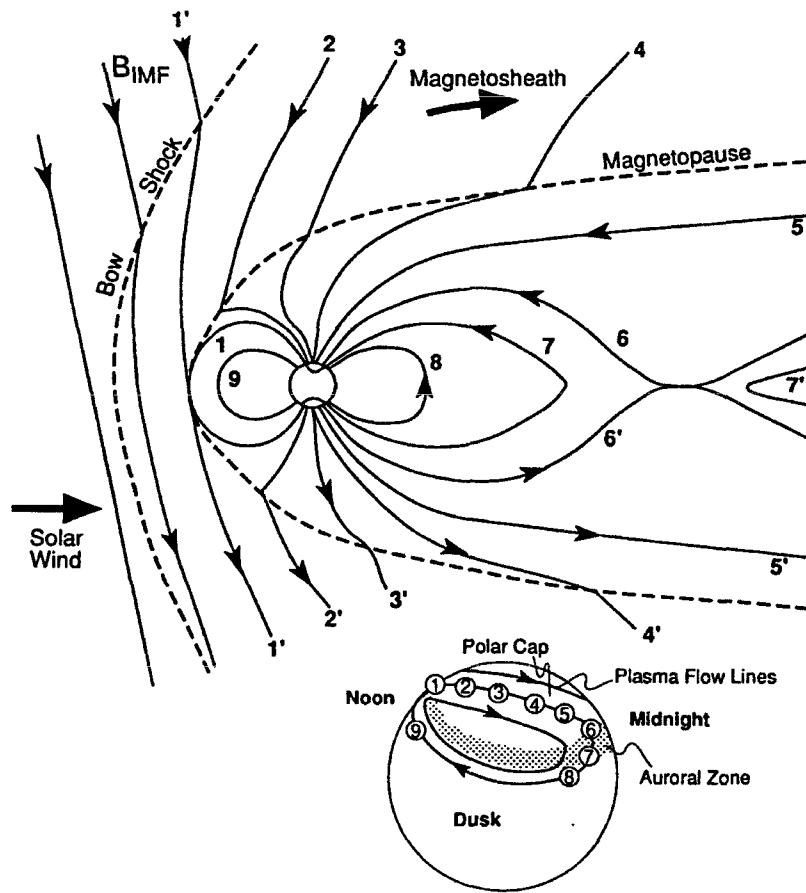
Figure 1-1: Graph is figure 9.11 of "Introduction to space physics" by Kivelson and Russell [43], showing reconnection and convection of the magnetic field lines in the magnetosphere. The numbered field lines show the sequence of reconnections and convection, starting with southward IMF 1' reconnect with the Earth's dayside closed field line 1. Then, the newly reconnected field line that has its root on the Earth convects tailward from line 2 to line 5. The night side reconnection happens between open field line in the north lobe 6 and the south lobe 6' and forms the closed field line 7. The newly closed field line, line 8, on the nightside then further convects toward the Earth and finally moves back to the dayside as line 9 after passing either the dawn or dusk side of the Earth. The small graph on the bottom right showing the foot points of all the labeled magnetic field lines on the north hemisphere of the ionosphere and the corresponding plasma flows: antisunward flows in higher latitudes and sunward flows at lower latitudes. Copyright belongs to the authors and Cambridge University Press publication. Figure is reprinted with permission.

The Earth's intrinsic magnetic field is approximately a dipole field. Thanks to this strong magnetic field, solar wind particles do not directly impinge on the Earth. Instead, the solar wind compresses the Earth's magnetic field on the dayside, and the vast majority of the solar particles are deflected around the Earth's magnetic field. In some cases, when the IMF orientation is right, the IMF can "reconnect" with the Earth's magnetic field. Magnetic reconnection, as it was named, is a physical process during which antiparallel magnetic field lines that are very close disconnect from themselves and then reconnect with each other. Energy stored in the magnetic field will be then transferred to the plasma in the form of kinetic and thermal energy.

Figure 1-1 shows the flow of the magnetic field lines within the magnetosphere driven by the magnetic reconnection on the dayside and nightside (figure 9.11 from [43]). The reconnection between southward IMF (line 1') and the northward dayside magnetic field lines of the Earth (line 1) is believed to be the major process that brings the solar wind particles, momentum and energy into the magnetosphere. After the reconnection, the initially closed dayside field lines are now open with one end rooted at the pole of the Earth and the other end connecting with the IMF, such as line 2 in figure 1-1. The continuous streaming of the solar wind then drags the open field lines antisunward and forms an area called the lobe, as shown in figure 1-1, with field lines moving tailward from line 2 to line 3 and all the way to line 5. As the open field line sweeps tailward, it creates an electric field through $\mathbf{E} = \mathbf{V_{SW}} \times \mathbf{B_{SW}}$. This dawn-dusk direction electric field is usually called the convection field. This electric field can be sensed along the open magnetic flux tubes, because the magnetic field lines are equipotentials. At its ionospheric end, the convection of the magnetic field lines drive the ions flowing from noon toward the midnight and form the famous double-vortex flow pattern, which we usually refer to as the high-latitude convection pattern as shown in the bottom right in figure 1-1. The direction on the convection pattern shows the plasma flow direction and the number shows the foot points of the magnetic field lines. In the magnetosphere, it leads to the $\mathbf{E} \times \mathbf{B}$ drift that is the main drift bringing the magnetospheric plasma toward the equatorial plane. In the far tail, the open

3

field lines in the south and north lobes can then reconnect again and form new closed field lines at the nightside of the Earth. This is indicated as in figure 1-1, with field line 6 and 6' reconnecting to form a new closed field line such as line 7. This newly formed closed field line then convects earthward and moves to the dayside, shown as line 9 in figure 1-1, from either the dusk or the dawn side of the Earth. This process brings the magnetic flux that was lost through the dayside reconnection back to the Earth. As a result, the convection pattern observed at the high-latitude polar cap is connected to the magnetotail through the magnetic field lines and can be used to estimate the basic shape of the magnetotail. The Earth's magnetosphere is defined as the reshaped Earth's magnetic field, which contains a dipole-like inner region and a tail region that extends many hundreds of R_E antisunward, as well as all the plasma population inside. It has been shown that northward IMF can reconnect with the open field lines at the poleward point of the cusp [47]. However, this reconnection is much weaker than the one triggered by the southward IMF.

The magnetic field strength in the lobe is very strong, around 20~30 nT, compared with other regions inside the magnetosphere but the plasma density overall is relatively low. The direction of the magnetic field is sunward in the north lobe and antisunward in the south lobe. Between the two lobes is a region called the plasmasheet, which has a much lower magnetic field but a highly concentrated hot, keV range, plasma, including H^+, He^{++}, He^+ and O^+. The plasmasheet boundary layer (PSBL) is the region between the plasmasheet and the lobes. The plasmasheet is the nightside closed field lines region of the Earth. Although there is a cross-tail current in the equatorial plane of the plasmasheet, the effect of the current is not strong in the near-Earth magnetosphere.

The inner magnetosphere refers the region relatively close to the Earth, roughly from 1 R_E to 6 R_E, where the field remains nearly dipolar. It consists of a number of overlapping particle populations, including the inner plasmasheet, the plasmasphere, the ring current and the radiation belt. The plasmasphere is defined as the dense cold-plasma population with in this region, while the radiation belt emphasizes the penetrating radiation, specifically particles that can penetrate deep into dense materials and thus cause radiation damage.

The ring current (e.g., [23]) mainly consists of H^+, He^+, and O^+ with energies of $10 - 200$ keV and electrons that drift azimuthally around the Earth at radial distances of about $2 - 7$ R_E (Earth radii) due to a combined curvature and gradient drift. The drift is eastward for electrons and westward for ions so the direction of the current is actually westward.

The cusp region is a funnel-shaped area between the dayside closed field lines and the nightside open field lines in the north and south polar regions, where the magnetic field magnitude is close to zero. Hence, it provides a direct entry for the solar wind particles. Solar wind particles may also flow along the open field lines in the tail and then enter the magnetosphere.

1.2 Geomagnetic Storms
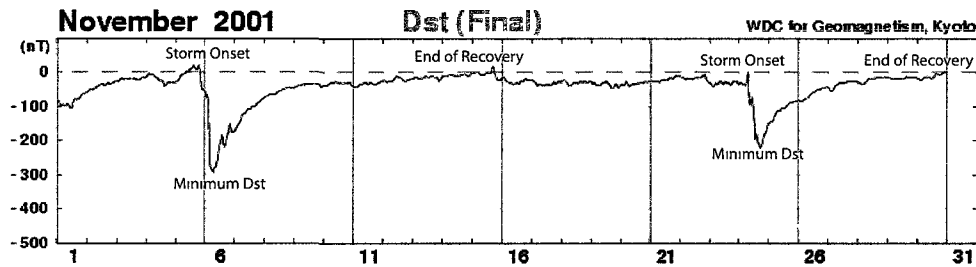
Figure 1-2: Dst index in November 2003. Plot is from World Data Center for Geomagnetism, Kyoto

A geomagnetic storm is a temporary disturbance of the magnetosphere driven by a disturbance in the solar wind and IMF. A standard model is that the extended southward IMF keeps on reconnecting with the Earth's magnetic field lines on the dayside, which increases the earthward convection of the plasma in the plasmasheet. The plasma then flows to the inner magnetosphere and is trapped in the Earth's magnetic field, enhancing the ring current with energetic particles. The enhanced ring current is able to interrupt Earth's magnetic field and increase its intensity. Over time, the ring current ion flux decreases due to

charge exchange and the storm ends. The Disturbance Storm Time (Dst) index is a common proxy for a storm. It measures the averaged horizontal component of the magnetic field observed by the ground-based magnetometers at equatorial latitudes. Figure 1-2 is a plot of hourly Dst values in November 2001 from the World Data Center for Geomagnetism, Kyoto. A typical large storm is observed around November 6th, and the minimum Dst occurs at 0600UT and is about 290 nT. The onset of the storm is defined as the initial jump observed before the decrease of the Dst index at 1900UT on November 5th, which is caused by the displacement of the magnetopause driven by the sudden solar wind pressure enhancement. The time period from the onset to the Dst minimum is defined as the storm main phase while the time period from the minimum Dst to the nonstorm time level Dst is usually called the recovery phase. A weaker storm is observed on November 24th, with minimum Dst at -196 nT.

For there to be a storm, a disturbance must be large enough to drive particles into the inner magnetosphere. There are many smaller disturbances that drive high latitude auroral activity, but not a full storm. The standard indices for measuring the general activity level of the Earth's magnetic field are the Kp and the AE indices. The K-index is derived from the maximum fluctuations of horizontal components observed on a magnetometer during a three-hour interval. The official planetary Kp index is derived by calculating a weighted average of K-indices from a network of geomagnetic observatories at mid-high latitude. The Auroral Electrojet (AE) index, a measure of the horizontal magnetic deflection at auroral latitudes, is supposed to reflect auroral geomagnetic activity, primarily associated with tail magnetic activity. However, the longitudinal coverage is limited, so localized substorm activity may sometimes escape detection.

1.3 Ionospheric Ions

The ionosphere is the upper part of the atmosphere of the Earth and the inner boundary of the magnetosphere. It contains plasma that has been ionized by the Sun's UV radiation, including H^+, He^+, O^+, O_2^+ and N^+. In addition to the solar wind particles, ionospheric ions

are the other source for the plasma inside the magnetosphere. Because O^+ is only from the ionosphere, it becomes the signature ion when we study the impact of ionospheric ions on the magnetosphere. Thus, it is the key element for understanding the ionosphere-magnetosphere coupling. As a matter of fact, O^+ has been found in the lobes, the plasmasheet and the ring current, and the fraction of O^+ in these regions increases during geomagnetic active time as will be discussed in the following sections.

Ionospheric ions are transported through several pathways. Ions flowing out from the cleft ion fountain [50] are heated and accelerated in the dayside cleft/cusp region (to be called cusp in the rest of the thesis), convect over the polar cap while moving along the open field lines to the tail lobe. A kinetic model of ion transport in the magnetosphere by Horwitz and Lockwood [35] shows that ions injected from the cusp disperse according to their velocity: ions with lower velocity will convect towards the central plasmasheet closer in, while faster ions will flow higher in the polar cap, taking a longer trajectory in the tail lobe and then enter the plasmasheet further down [34]. Figure 1-3 shows the O^+ transport path made by Horwitz [34] for (a) strong convection (100 mV/m) and (b) weak convection (20 mV/m). O^+ are clearly separated by the their velocity in both figures while stronger convection is able to bring more energetic ions to the near-Earth tail lobes.

As a result, when ions from the cusp are observed over the polar cap or in the lobes, they are tailward-streaming and mono-energetic, because only a particular energy ion reaches a particular tail lobe location. Observations have confirmed this, and beam-like O^+ distributions have been observed over the polar cap [20], in the lobe [59][46], and in the distant tail (up to 210 R_E) lobe/mantle region by Geotail [68]. Later, O^+ inside the lobe may either convect into the central plasmasheet through the PSBL and then convect inward to feed the ring current or be lost in the distant tail. In the nightside auroral region, ionospheric ions flowing along closed field lines may be directly injected into the near Earth plasmasheet without passing through the lobe region. Statistical studies have shown that there is significant O^+ outflow from both sources (e.g. review by [77]). Simulations of trajectories of the outflowing ions have shown that both sources may access the nightside plasmasheet so

7
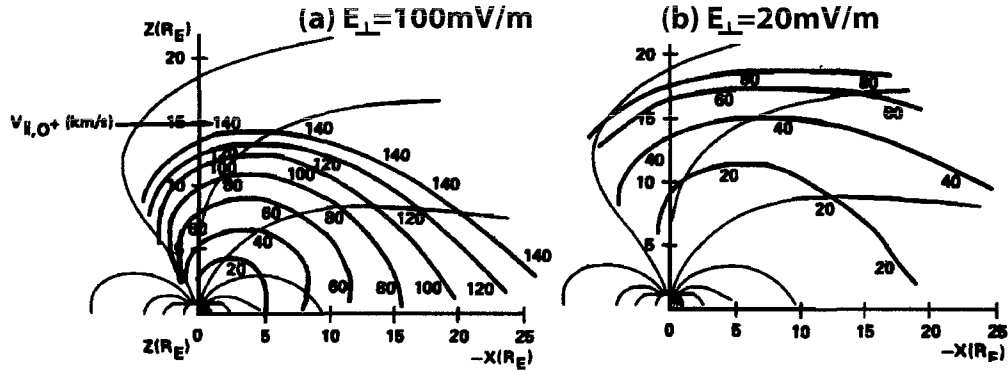
Figure 1-3: Transport path of O^+ under (a) strong convection (100 mV/m mapped to the ionosphere) and (b) weak convection (20 mV/m) from [34] figure 3. Copyright [1986] American Geophysical Union. Reproduced/modified by permission of American Geophysical Union.

both may contribute to the O^+ population in the plasmasheet [18][11][76]. Other sources or paths, such as energetic O^+ transport from the dayside plasmasheet to the polar cap and then into the tail lobes [67] or slow moving O^+ that enters the ring current directly [61], have been mentioned as well, but seem to be a minor contribution to the development of a geomagnetic storm.

Although southward IMF is considered to be the main driver for geomagnetic storms, the ionosphere has been suggested to be not only a source for the magnetospheric plasma but also an active element in the geomagnetic processes [17]. It is also evident that ionospheric origin O^+ plays an important role during the formation of geomagnetic storms [29]. [78] and [15] showed that the outflow rate of O^+ observed with Dynamics Explorer (DE) -1 satellite correlated well with general planetary activity level (Kp Index). Moreover, ionospheric outflow from the cusp is enhanced right after an interplanetary shock [53] [24]. The O^+ density and flux of the outflow are also correlated with solar wind dynamic pressure [20][15]. These results imply that an increase of ionospheric outflow is expected with geomagnetic storm activity. Kistler et al. [42] showed that the cusp outflow increases significantly during storm times, and directly feeds the plasmasheet during the main phase of storms. Thus this

outflow is the likely source for the O^+ in the storm-time ring current.

It has also been shown that it is predominantly during storm-times that O^+ is a major constituent of the plasmasheet [58][40][41]. During non-storm times, the O^+ density is typically 5 percent of the H^+ density, while during storm-times it is typically 25 percent, and there are times when it is the dominant species. The O^+ density is highest during the storm main phase, and is still enhanced during the storm recovery phase. This is consistent with observations in the inner magnetosphere during storms that show O^+ becoming a dominant species during large geomagnetic storms. For moderate storms, the O^+ is typically 20-30 % of the ring current, while for large storms (Dst < -250 nT) the O^+ energy density can exceed 50% of the total [38][16][44]. In addition, the typical fast initial Dst recovery in a storm is also due to the rapid loss of O^+ at 75-100 keV via charge exchange in the inner portion of the ring current [29]. Thus there is a good indication that the plasmasheet is the direct feeder for the storm-time ring current.

Cully et al. [15] showed that the solar Extreme ultraviolet (EUV) flux, measured using the proxy F10.7, has a strong positive correlation with ion outflow fluence, defined as the mean net outflow rate, and the correlation is stronger for O^+ than H^+. F10.7 index measures the radio flux at wavelength of 10.7 cm on the Earth and it has been commonly used as a proxy for EUV strength due to the strong correlation between them, although a recent study shows that the correlation has changed during the last long solar minimum [9]. Cully et al. [15] also showed that other solar wind and IMF parameters have also been found to have a positive correlation with ionosphere outflows: solar wind pressure, density, velocity, temperature, electric field, IMF field magnitude and its variability. The enhanced ionospheric outflows are almost certainly the source for the storm-time plasmasheet directly or by passing through the tail lobes. However, because the transport of O^+ from the ionosphere to the plasmasheet is activity-dependent and is strongly influenced by IMF and solar wind pressure, it is difficult to understand the feeding of the ionospheric outflows to the plasmasheet without understanding the transport path quantitatively: the spatial location, the influence of the velocity effect, and the effect of external drivers. Because the

pressure balance between the solar wind and the magnetosphere, the solar wind pressure controls the size of the magnetosphere, and solar wind velocity may influence the convection field. The IMF Bz component influences the convection field and the reconnection rate on the dayside. Seki et al. [68] found that the region where O^+ was observed in the distant tail was controlled by IMF By. Since the transport path may change dramatically during storm times and varies under different external conditions [34], it is important to draw a base line of the transport path during nonstorm times when the magnetosphere is relatively steady and the convection field does not change much.

Simulation and theoretical studies have discussed the influence of the O^+ on the reconnection mechanism and other magnetospheric dynamic processes. However, this will not be the focus of this thesis.

1.4 Transport and Acceleration of Cusp-Origin Ions

In this thesis, we will investigate the transport and acceleration of O^+ from the cusp to the tail lobes with case studies and a statistical study using the identified streaming O^+ data from Cluster/CODIF. As discussed above, Horwitz [34] clearly showed that due to the combination of the parallel motion and the $\mathbf{E} \times \mathbf{B}$ convection ions of the same species are separated by their parallel velocities when they are transported from the cusp outflow to the magnetotail. Due to this velocity filter effect, even without acceleration the O^+ should have a higher energy further down the tail because slower O^+ enters to the central plasmasheet before they reach the magnetotail. Zhang et al. [79] studied a case where a large change in the energy of O^+ was observed when there was a sharp increase in solar wind pressure, and showed that some energy increase in the lobe O^+ beam may be due to field line displacement and the velocity filter effect, not due to centrifugal acceleration. The method in the paper by Nilsson et al. [55] using parallel velocity at different geocentric distance to evaluate the velocity increase is also misleading because the difference in the velocities at different locations may be simply due to the velocity filter effect. Hence, when investigating the velocity changes using data from satellites, it is important to differentiate

the acceleration contribution from the velocity filter effect.

It has been found that ionospheric ions can be accelerated above the polar cap [51][56][24]. However, due to the fact that the lobe region has, on average, low plasma density and high magnetic field strength, one likely acceleration mechanism in the lobes is the centrifugal acceleration, which was first investigated by Cladis [10] and then calculated with Cluster EDI and EFW data by Nilsson et al. [55]. This mechanism is caused by the centrifugal force arising from the convection velocity V_{EXB} and supplies energy with the curvature drift of the ion along the convection field. It accelerates particles along the magnetic field lines and can be described as

$$\frac{dV_\parallel}{dt} = \mathbf{V_E} \cdot \frac{d\hat{\mathbf{b}}}{dt} = \mathbf{V_E} \cdot \left(\frac{\partial \hat{\mathbf{b}}}{\partial t} + V_\parallel \frac{\partial \hat{\mathbf{b}}}{\partial s} + (V_E \cdot \nabla)\hat{\mathbf{b}} \right) \tag{1.1}$$

Where $V_\parallel$ is the velocity component that is parallel to the magnetic field, V_E is the $E \times B$ drift, $\hat{b}$ is the unit vector of the magnetic field, s is the length along the magnetic field line. The second and third terms of the equation 1.1 give the largest contribution to the acceleration [10][55]. Nilsson et al. [55] also showed that the average value of the centrifugal acceleration is about 5 m/s^2. However, the method only included H$^+$ in the 0-60 eV range [21], so it is possible that they missed higher energy H$^+$ that was already hot and fast in the polar cap and was then further accelerated in the tail lobes.

We will present our study on the acceleration of O$^+$ along the transport path in lobes in chapter 5 with case studies and a statistical study. The dependence of the acceleration on geomagnetic active level will also be briefly discussed as well as the acceleration mechanism of O$^+$ as it enters the plasmasheet.

1.5   Solar Cycle

The strength of the Sun's activity has a roughly 11-year cycle, which is usually called the solar cycle. The real period actually ranges from 9 to 14 years. A whole solar cycle period starts at solar minimum, continues with a solar arising phase, reaches the solar maximum, goes down with the solar declining phase and finally ends at another solar minimum. The

last full solar cycle is solar cycle 23, which lasted from 1996.5 to 2008.12 and peaked in the later part of year 2000. The sunspot number is the standard proxy for measuring the solar activity.

There are predominantly two ways in which the changing solar cycle can affect geomagnetic activity. One is that large ejections from the sun called Coronal Mass Ejections, the number of which decreases significantly towards solar minimum. These ejections are associated with strong southward IMF Bz, as well as enhanced pressure, and so are the main drivers of large storms. The second is that the solar EUV flux, which heats the ionosphere, also increases and decreases with the solar cycle. EUV has been monitored since 1996 with the Solar Extreme Ultraviolet Monitor (SEM) of the Charge, Element, and Isotope Analysis System (CELIAS) onboard the Solar & Heliospheric Observatory (SOHO), followed by the Solar EUV Experiment (SEE) on the NASA Thermosphere Ionosphere Mesosphere Energetics and Dynamics (TIMED) mission, and now with the Solar Dynamics Observatory (SDO). Another way to monitor EUV on Earth is to use F10.7 index, which is the solar radio flux at a wavelength of 10.7 cm observed on the Earth. This parameter correlates strongly with solar EUV output at most of the time.

The dependence of the geomagnetic activity on the solar cycle is clear: the number of the storms has a clear difference between the solar maximum time and the solar minimum. It has also been found that the solar EUV flux has a strong impact on the ionospheric outflows [62]. The average solar wind parameters also have a dependence on the solar cycle but it is not as clear. Ruohoniemi [65] showed that the high-latitude convection pattern has almost no correlation with the solar cycle. In chapter 6, we will discuss the dependence of the O^+ transport path on the solar cycle with data from 2001 to 2009.

1.6 Summary

In this thesis, we will present results from a statistical analysis of the transport of O^+ from the dayside cusp to the plasmasheet, and its dependence on geomagnetic active level and external drivers, using data mainly from Cluster CIS/CODIF. We present the analysis

method and results of the statistical study in chapter 3 and then discuss the features and physics of the results in chapter 4 and 5. A detailed discussion of the solar cycle dependence of O^+ transport path will also be given in chapter 6.

Chapter 2

INSTRUMENTATION

In this chapter, we will briefly introduce the satellite and the instruments used in this study. We will address the transport of ionospheric ions to the magnetotail using data primarily from the time-of-flight ion COmposition DIstribution Function (CODIF) sensor of the Cluster Ion Spectrometry (CIS) instrument [63] on the Cluster satellites. We also used the Electric Field and Wave instrument (EFW) [26] and the FluxGate Magnetometer (FGM) [5]. Solar wind and IMF data are collected by the Advanced Composition Explorer (ACE) and all geomagnetic activity indices are obtained from OMNI data.

2.1 Cluster Mission

Cluster, launched in 2000, is a constellation mission of four spacecraft flying in a tetrahedral configuration as shown in figure 2-1, a drawing of Cluster from the European Space Agency (ESA) website. Cluster has a 4 R_E × 19 R_E polar orbit and it takes about 57 hours for the satellites to finish one orbit. The apogee of the spacecraft was initially in the equatorial plane but gradually moved southward in the later years. During the first four years of the mission, the equatorial plane encounters occur mainly at Cluster apogee of 19 R_E in the summer. In the Cluster extended mission, the spacecraft crossed the equatorial plane at closer and closer distances, so it could observe the near-Earth part of the plasmasheet and the lobes.

For this study we will concentrate on observations of O^+ in the magnetosphere moving from the cusp/cleft source region through the tail lobes and into the plasma sheet. The polar orbit of the CLUSTER satellites allows us to observe both the -19 R_E plasma sheet,
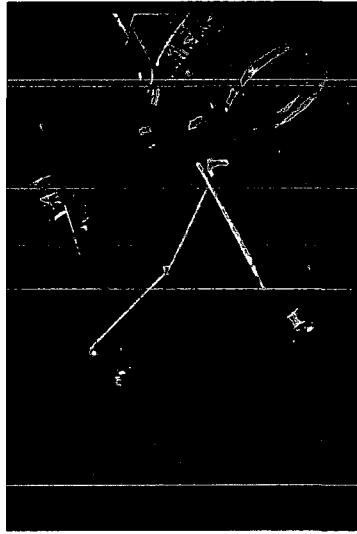
Figure 2-1: Artist's view of the Cluster spacecraft (ESA image).

the polar regions and lobes during tail season, from July to October, and near-Earth regions throughout the year, with local time coverage depending on the season. Figure 2-2 sketches the polar orbit of Cluster in the summer with a magnetotail plasmasheet crossing at -19 R_E. For most of the study, we will only use data during the solar maximum, from 2001-2002, in order to eliminate any solar cycle effect in those studies. However, part of our studies will specifically address how the O^+ transport path changes with the solar cycle so we will utilize data from 2001 to 2009.

There are eleven scientific instrument onboard Cluster and they are identical on all spacecraft. We only used the data from spacecraft 4 in this study rather than multiple spacecraft because we are studying large-scale features, and have averaged the data over 5 minutes for better statistics. With this resolution all spacecraft generally observed the same data.

2.1.1 CODIF

Cluster is the first satellite mission since ISEE to measure ion composition in the bulk-plasma energy range in the central tail. The ISEE ion composition data set has resulted
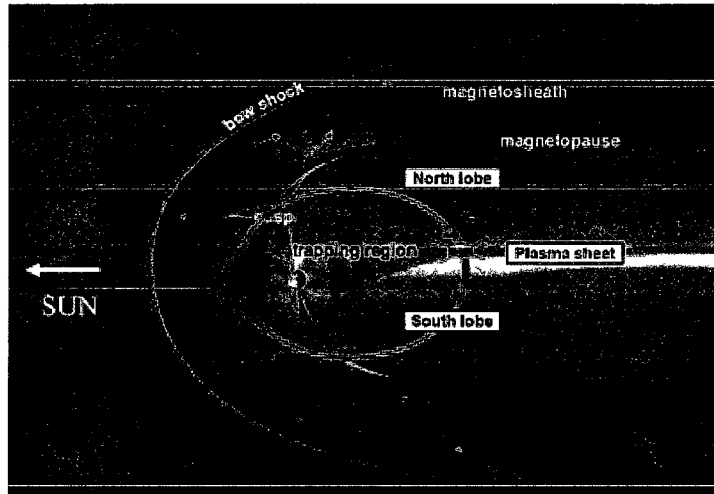
Figure 2-2: Diagram of Earth's magnetosphere with Cluster orbit during the tail season (ESA image)

in many important findings but was limited in both temporal resolution (10-15 minutes per cycle) and energy range (0.1-16 keV). The Cluster CIS/CODIF is a combination of a top-cap electrostatic analyzer followed by postacceleration of 15 kV and then a time-of-flight measurement. Figure 2-3 is a photo of CIS instrument. The instrument on the left is the CODIF and the one on the right is the HIA ion detector. Data from the HIA is not in use in this thesis. The data set from CIS/CODIF provides a substantial enhancement over the earlier data set. It can resolve the major species, H^+, He^{++}, He^+, and O^+ within energy range from 40 eV/e to 40 keV/e. The low energy threshold of 40 eV is significantly lower than the ISEE measurements, while the energy maximum of 40 keV is high enough to include the most significant contributions to the plasmasheet pressure [39]). The temporal resolution for a full 3D distribution function is 4 to 16 seconds (depending on mode) and the geometric factor of one (out of 8) positions in the CIS instrument is $2.2 \times 10^{-3} \text{cm}^2\text{sr}(\text{dE}/\text{E})$. Thus both the intrinsic time for a measurement and the counts needed to make a statistically valid measurement have been improved. However, there may be low energy ions, ranging from escape velocity ($\sim$10 eV) to 40 eV, inside the polar cap and tail lobes missed by this instrument [21].

16
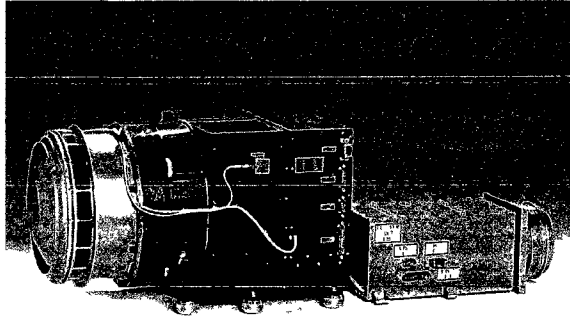
Figure 2-3: The CODIF (on the left) and the HIA(on the right) ion detectors of the CIS experiment. (CIS web sever image).

2.1.2 FGM

FGM onboard Cluster consists of two tri-axial fluxgate magnetometers mounted on one of the two 5 meters radial booms, as well as a data processing unit on the main equipment platform [5]. The instrument measures the magnitude and direction of the magnetic field.

2.1.3 EFW

Each Cluster spacecraft also has the EFW, an electric field and wave experiment based on the double probe technique [26]. On the tip of each radial wire boom, which spins with the spacecraft at a period of 4 s, are a spherical probe and a preamplifier. The two probe pairs are orthogonal to each other, which allows for the measurement of two electric field components that are perpendicular to each other in the spin plane. In order to reconstruct a 3D electric field from these two components, the assumption is made that there is no electric field parallel to the magnetic field.

2.2 Solar Wind and Auxiliary Data: ACE

In addition, measurements of the solar wind, IMF and solar irradiation as well as geomagnetic indices have been used to check correlations, and as inputs to the magnetic field model used for mapping. The transport of plasma in the magnetosphere is mainly controlled by

the solar wind, in particular the direction of the IMF. The IMF direction is often described in terms of clock angle, i.e., the angle between the Z_{GSM} axis and the projection of IMF into the YZ_{GSM} plane. A 0 clock angle indicates a purely northward IMF; 90 indicates an IMF pointing in the $+Y_{GSM}$ direction and so on. In this study, measurements of the IMF and solar wind plasma data are from Advanced Composition Explorer (ACE) data. ACE, launched in 1997, is an explorer mission orbiting the L1 libration point. From its location at L1, it has a prime view of the solar wind, interplanetary magnetic field and higher energy particles accelerated by the Sun, as well as particles accelerated in the heliosphere and the galactic regions beyond. The time shift of the solar wind measurements is done in this study to propagate the solar wind data to the bow shock at about 10 R_E.

2.3 Geomagnetic Disturbance Indices: OMNI

In order to correlate O^+ transport behavior with different geomagnetic activities in the magnetosphere, we used various geomagnetic indices including Dst index, Kp index and AE index, which were obtained from the GSFC/SPDF OMNIWeb interface at the address: http://omniweb.gsfc.nasa.gov [36].

Chapter 3

DATA ANALYSIS

In order to investigate the transport of O^+ from the dayside cusp to the plasma sheet, we have performed a statistical study of the location and properties of the narrow-energy-band field-aligned O^+ that has been observed in different regions inside the magnetosphere during geomagnetic storms and non-storm times [52][20][70][59][46][42]. In this chapter we will discuss the criteria used to identify the streaming O^+, the procedure for automatic identification for those O^+ beams, the calculation of the moments of streaming O^+, the external conditions used for sorting the data and some of the statistics of the resulting data set.

3.1   Criteria of Streaming O^+

Figure 3-1 shows one day of data starting from 1300UT on September 10 2001 from CODIF/CIS on CLUSTER S/C4. Figure 3-2 shows projections of the orbit of the satellite during this time in the XZ_{GSM} (figure 3-2a), XY_{GSM} (figure 3-2b) and YZ_{GSM} (figure 3-2c) planes. The satellite is close to the noon-midnight meridian in the XZ_{GSM} plane, moving over the polar cap, and into the lobe and plasma sheet, so it covers the different regions through which cusp origin O^+ may pass through. The color in figure 3-1 represents the differential flux $(cm^{-2}s^{-1}sr^{-1}(eV/e)^{-1})$ for all six panels. The top panel (Figure 3-1a) gives the plasma beta, defined as plasma pressure over magnetic pressure; figure 3-1b gives H^+ energy spectrum; figure 3-1c gives the energy spectrum of tailward moving O^+; figure 3-1d gives energy spectrum of earthward moving O^+; figure 3-1e gives O^+ pitch angle spectrum for the energy range from 40 eV to 40 keV and figure 3-1f gives the Dst Index. The pink
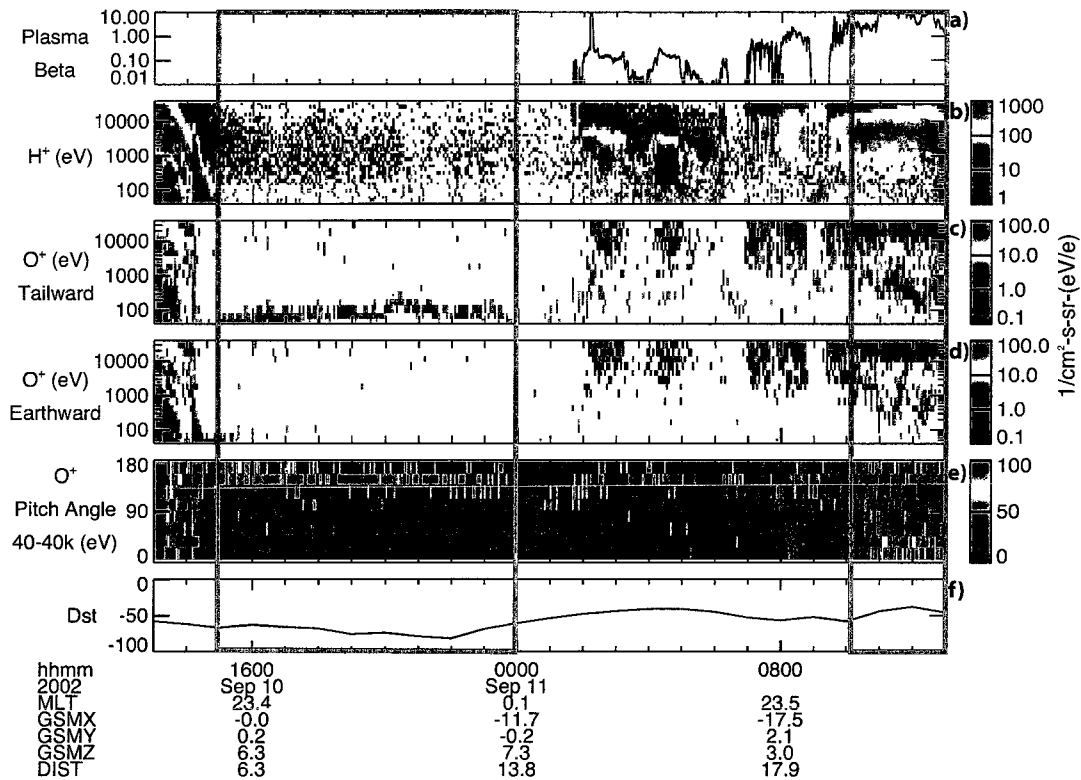
Figure 3-1: CIS/CODIF data for 24 hours, starting from 1300UT September 10 2002, with Cluster S/C 4 moving from the dayside cusp outflow region to the plasma sheet at -19 R_E . Panels from top to bottom are: a) Plasma beta, b) H^+ energy spectrum, c) Energy spectrum of tailward moving O^+, d) Energy spectrum of earthward moving O^+, e) O^+ pitch angle spectrum for energy from 40 eV to 40 keV, f) Dst Index.

box on the left shows the time period when streaming O^+ in the lobes were observed, from 1400UT to 2400UT on September 10 2001. The red stripe in the tailward moving O^+ energy spectrum, figure 3-1c, is a clear example of the O^+ in the CODIF data set. They always have a narrow energy range inside the lobes, most likely caused by the velocity filter effect as described in the introduction, a differential flux higher than local O^+, so that they can be easily identified by eye in the tail lobe, and a near-field-aligned tailward direction resulted from the combination of the field-aligned motion and the convection, as shown in the pitch angle spectrum of O^+ in figure 3-1e. Streaming O^+ like this can be observed for hours or even days.
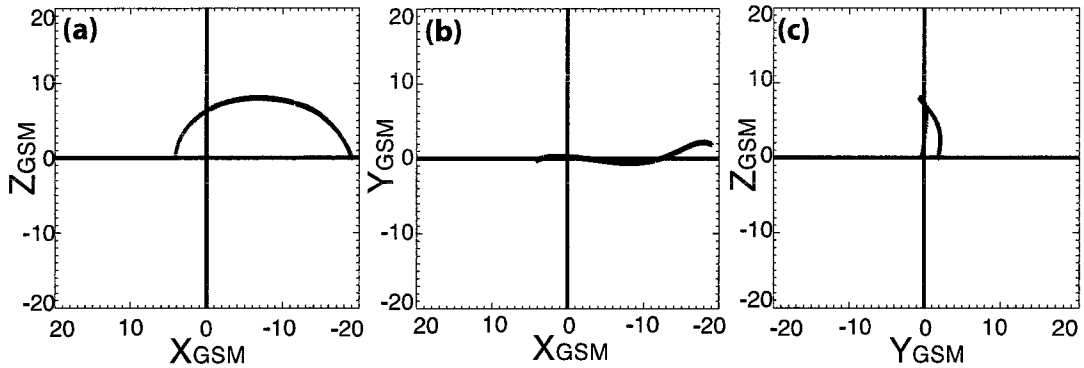
Figure 3-2: Orbit plots for figure 1. Plots from left to right are orbits shown in (a) XZ_{GSM} plane, (b) XY_{GSM} plane and (c) YZ_{GSM} plane. Most of the time, CLUSTER satellites are in the midnight-noon sector.

While this population is most easily identified in the lobe, a similar population can also be observed in the PSBL and the plasma sheet. Cluster passed the plasmasheet from 1100UT to 1300UT on September 11 2002, in the pink box on the right. Similarly, the red stripe on top of the yellow spectrum is the observed streaming O^+. The energy range of the streaming O^+ is broader (covers 3 energy bins for most of the time) than the lobe beams. This may be due to heating as the beam enters the PSBL or due to the fact that part of the streaming O^+ population scatters and isotropyrizes as it passes through the plasmasheet but a substantial fraction of the beam population are still moving along the field line. The appearance of O^+ beams in the plasma sheet and PSBL is also the evidence for cusp origin O^+ as a direct feeder for energetic O^+ inside plasma sheet. A more detailed discussion is described by Kistler et al. [42]. Note that there are also lobe beams observed from 0900UT to 0930UT. The energy of those beams is close to 1keV, which is comparable to those energetic beams observed in the plasmasheet. Although the pitch angle spectrum is not limited to the streaming O^+ population, the field-aligned distribution in both directions can still be seen. The fact that the pitch angle spectrum is not as sharp in the plasma sheet and PSBL as in lobes may be due to the combined effect of the existence of local plasma and/or the isotropization of the tailward streaming O^+.

Figure 3-1 shows mainly tailward-streaming O^+ distributions while also giving an example of earthward streaming O^+. When the O^+ from the lobes enters the plasmasheet as the field line reconnects in the tail, the behavior of the ions depend on the magnetic field curvature and the gyroradius of the particle [8]. If O^+ is on a field line that has a small curvature radius that is comparable to its gyroradius, as usually happens when the plasmasheet is thinning, the O^+ will be isotropized and heated as described before. However, if the curvature radius is much larger than the gyroradius of the O^+, it will stay on the field line, pass the neutral sheet and stream earthward. The bidirectional streaming O^+ are observed when the satellite detects both the tailward streaming population and the streaming O^+ that was just turning earthward.

To study the transport of the O^+ ions statistically, we have automated a procedure to identify the streaming O^+ in the lobes, plasma sheet and PSBL. Using this procedure, we have surveyed the CLUSTER/CODIF data set from 1 March 2001 to 31 December 2009 to identify the field-aligned O^+ beams, to determine the spatial regions where they are observed, and to show how their properties change with location and with geomagnetic activity.

3.2   Automatic Streaming O^+ Identification Procedure

Our automatic procedure searches for O^+ in both directions so that O^+ streaming both tailward and earthward can be identified. Figure 3-3 shows the general identification procedures for tailward (figure 3-3b-d) and earthward moving distributions (figure 3-3e-g) in different magnetosphere regions) for the same day of data as in figure 3-3. Plasma beta, plotted in figure 3-3a, is used to divide the magnetotail into: polar cap and tail lobes, where beta is less than 0.05; plasma sheet, where beta is greater than 1; and plasma sheet boundary layer, where beta is between 0.05 and 1. The value of plasma beta at 0.05 and 1 are shown as blue lines in figure 3-3a. Figure 3-3b is the energy spectrum of tailward moving O^+ averaged over 5 minutes. Energy bins with low counts are removed so that only statistically valid distributions are identified. The value of low counts threshold is at 9 count

per energy bin per time resolution, which was decided with experience. The data are used to identify the energy bin with the highest differential flux at each time. This identified energy is indicated with the black line. The pitch angle spectrum is then calculated for a narrow range around the peak energy (1 energy channel for 16 energy bin mode and 2 energy channels for 32 energy bin mode) and plotted in figure 3-3c. Note that the pitch angle plot includes all directions, not just the tailward direction. Local peaks are extracted from the pitch angle spectrum and again, bins with low counts are removed.

In order to ensure the beam peaks are well above the plasma background, a differential flux threshold is introduced with a relative value different for different magnetotail regions. The differential flux threshold is equal to the average differential flux at each time multiplied by a factor, 1.1 in the lobes, 1.3 in the plasma sheet boundary layer and 1.5 for the plasma sheet. This insures that the distribution is sufficiently peaked in pitch angle spectrum, so the plasma will have a clear streaming direction. The factor was determined by looking at the response of several streaming O^+ events in different regions during different geomagnetic active levels for different years, so that the identification program works well under all conditions. With this procedure we are confident that the distributions that are selected are the desired field-aligned distributions, as shown in 3-3d. We determine whether the field aligned flows are earthward or tailward using the CLUSTER magnetic field data and the location of the spacecraft (i.e., 0 degrees pitch angle means tailward in the south but earthward in the north). We only kept the identification results in the tailward direction in the procedure for tailward moving O^+ and there is also similar step for earthward results. Only consecutive 5-minute streaming O^+ events with streaming direction varying less than 1 angle bin (22.5 degrees) and the energy peak changing within 1 energy bin are considered to be one streaming distribution. Any consecutive streaming distributions with duration less than 15 minutes are removed.

23
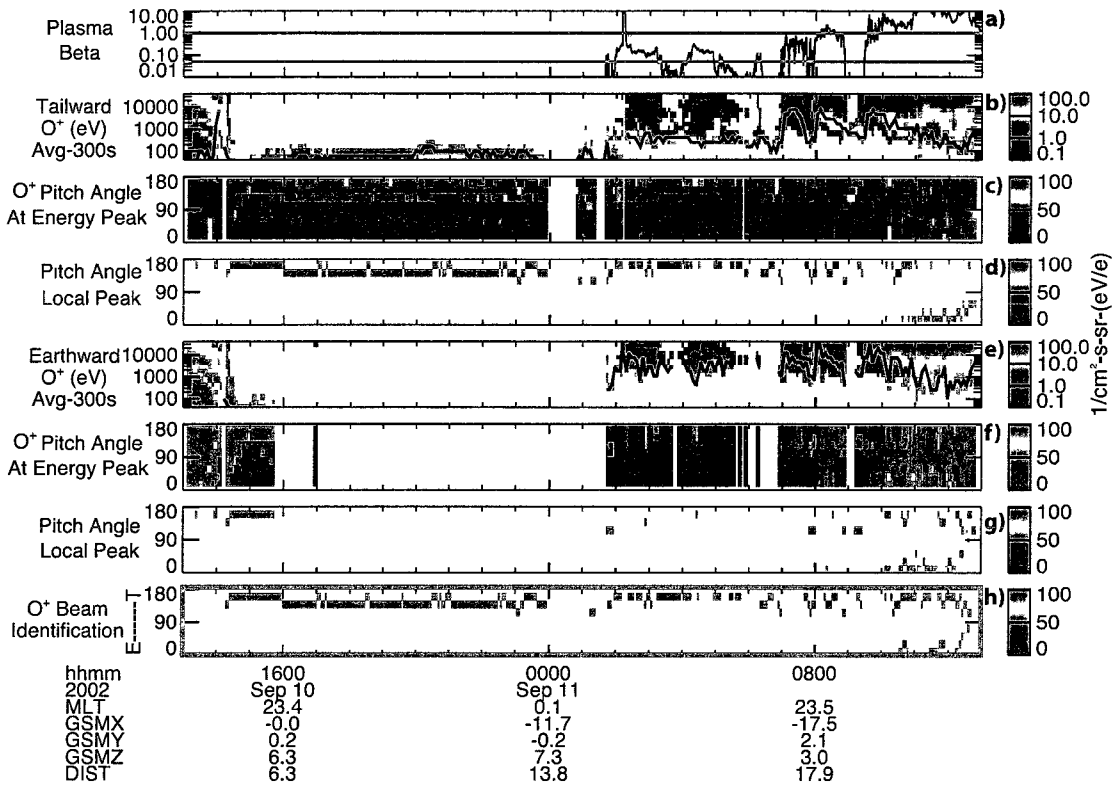
Figure 3-3: Streaming O^+ identification procedures. Same day of data as shown in figure 3-1. Panels from top to bottom are: a) Plasma beta, with pink lines showing the defined value for differentiating the lobes, PSBL and plasma sheet; b) Tailward O^+ energy spectrum averaged for 5 minutes, with black lines showing the energy channel with highest differential flux at each time; c) O^+ pitch angle spectrum plotted around the energy peak shown in panel (b); d) O^+ pitch angle local peak extracted from panel (c), refer to the text for detailed explanation; e) Earthward O^+ energy spectrum averaged for 5 minutes, with black lines showing the energy channel with highest differential flux at each time; f)O^+ pitch angle spectrum plotted around the energy peak shown in panel (e); g) O^+ pitch angle local peak extracted from panel (f); h) Combined identification results for streaming O^+ with y axis representing the O^+ streaming direction: Earthward (E) or Tailward (T).

24

Figure 3-3e-g have the same arrangement as figure 3-3b-d except they are showing the identification procedure for the earthward distributions. The final panel (figure 3-3h) is the combined identification results showing the differential flux and direction of the final identified streaming O^+ in the sense of tailward and earthward. After running the program over 9 years of Cluster data, for each identified 5-minute event, the time, location, differential flux and the pitch angle are recorded. The energy flux and phase space density are also included for further analysis.

3.3 Moments of Streaming O^+

We also calculated the characteristic properties of O^+ for further study. The errors in the moment calculation are also included for better understanding of the uncertainty in the calculated moments.

3.3.1 Moments Computation

Using the "ccat" program package written by C. Mouikis, for each identified 5-minute event, we calculated the characteristic properties of the streaming O^+, including density, velocity and temperature, as well as parallel and perpendicular velocity and temperature. Although streaming O^+ is mostly mono-energetic inside the lobe region, its energy range has becomes wider in the PSBL and plasmasheet as discussed before. Hence, we defined the energy range of the identified streaming O^+ as the last energy bin from the energy peak to have its differential flux above 10% of peak value. We then calculated moments around this energy range.

Figure 3-4 shows the calculated results for the same day of data as in figure 3-1 and figure 3-3. From top to bottom, panels are a) and b) tailward and earthward O^+ energy spectrum averaged for 5 minutes with black line showing the energy range of the identified O^+ beams; c-i) Calculated moments of identified O^+ beams: density, total Velocity, parallel velocity, perpendicular velocity, total temperature, parallel temperature and perpendicular temperature. Black points are the moments calculated from tailward distributions while
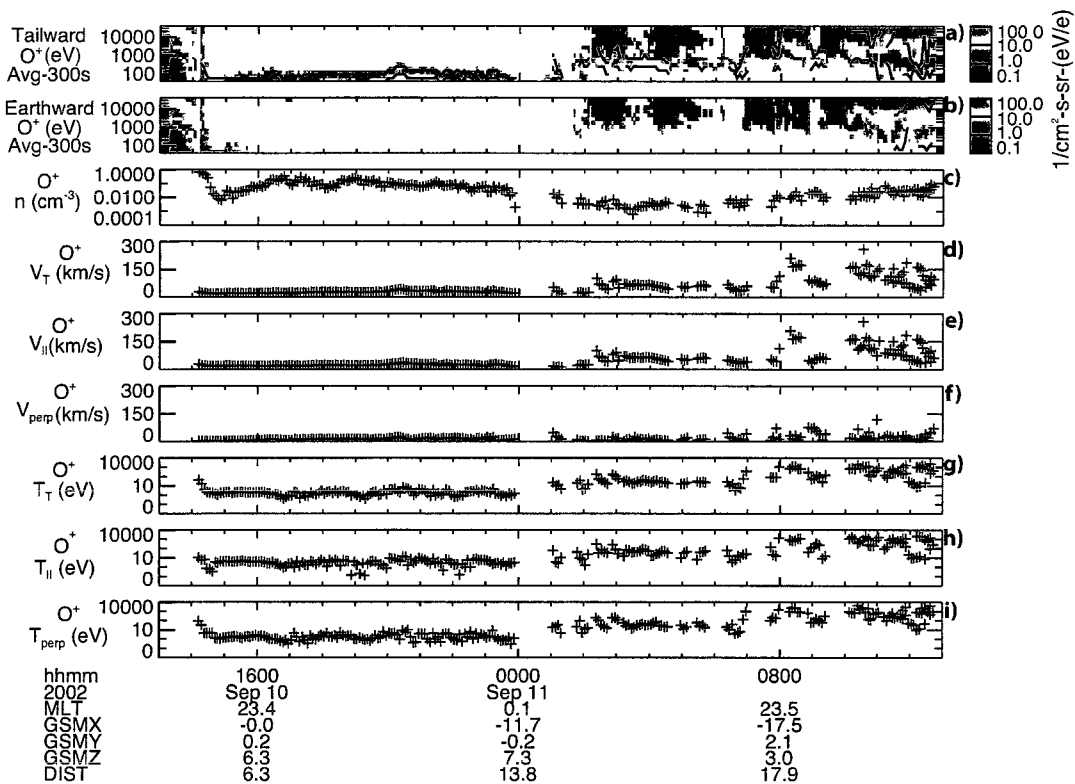
Figure 3-4: Calculated moments of identified streaming O$^+$. Same day of data as shown in figure 3-1. Panels from top to bottom are: a-b) Tailward and earthward O$^+$ energy spectrum averaged for 5 minutes with black line showing the energy range of the identified O$^+$ beams; c-i) Calculated moments of identified O$^+$ beams: density, total velocity, parallel velocity, perpendicular velocity, total temperature, parallel temperature and perpendicular temperature. Black points show the moments calculated from tailward distributions while blue points are from earthward distributions.

blue points are from earthward distributions. The density of the streaming O$^+$ is dependent on magnetic field magnitude at each location because the ion flux in each magnetic flux tube should be conserved. The density of earthward streaming beams inside the plasma sheet is consistent with the tailward streaming beams at the same location from 1000UT to 1200UT September 10 2002, which hints that they may be the same population with some of them having crossed the neutral sheet or mirrored back. In this case, parallel and perpendicular velocities seem to be within the same order in the lobe region while the parallel velocity is obviously higher in the plasma sheet. Parallel and perpendicular

temperatures are comparable with each other in both lobes and plasma sheet. An increase in the velocity and temperature with distance from the Earth in the lobes may indicate that acceleration is occurring in the lobes, or may be a result of the velocity filter effect. Typically, streaming O^+ is cold in the lobe but when it enters the plasmasheet it gets faster and hotter, which indicates that it may experience further acceleration when entering the plasmasheet. The temperature of the streaming O^+ inside the plasmasheet is often observed higher than the bulk kinetic energy inside the plasmasheet. Those beams are not typical streaming O^+ in the lobe as described in the earlier part of this chapter, but they are also included in this study because they are found to be the lobe streaming O^+ just entering the plasmasheet [42] and they still maintain their general moving direction. The moment calculation was carried out for all identified streaming O^+ from 2001 to 2009.
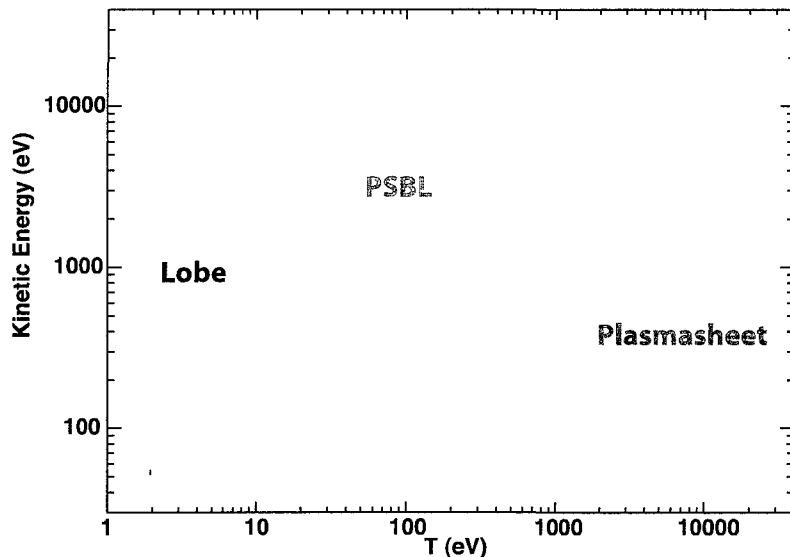
Figure 3-5: Scatter plot of all streaming O^+ data from 2001 to 2009 with x-axis and y-axis are total temperature and bulk kinetic energy, calculated with $mV_{bulk}^2/2$. Black, pink and red points represent the streaming O^+ events observed in the lobes, the PSBL and the plasmasheet respectively.

Figure 3-5 is the scatter plot of bulk kinetic energy, calculated with $mV_{bulk}^2/2$, versus total temperature for all streaming O^+ data from 2001 to 2009. The plot shows the streaming

O^+ is limited in certain range of bulk energy and total temperature for streaming in lobes, PSBL and plasmasheet. In the lobes, most of the O^+ beams are relatively slow and cold while in the PSBL they are hotter and faster. The ratio between the bulk kinetic energy and total temperature is around 10:1 for lobe beams while this ratio is reduced for beams in the PSBL, indicating that streaming O^+ is scattered when they entering the PSBL. O^+ beams in the plasma sheet have the highest bulk energy and temperature of all. The reason for the high energy is that the locations where the satellite passes the plasmasheet are usually far from the Earth so only the high energy beams can reach there. The ratio between the bulk kinetic energy and the temperature is even lower than those beams in the PSBL while some populations even seem to be separated from the main distribution and have a temperature that is higher than the bulk energy. As discussed, before those streaming O^+ with temperature higher than the bulk kinetic energy are no longer typical beams but still . maintain a general streaming direction.

3.3.2   Moments Accuracy

In addition to the statistical errors resulting from the underlying distribution functions, the moments suffer from limitations introduced by the implied integration procedures. The errors can be significant when the number of counts is low, and when the peak of the distribution is close to the energy limits of the instrument. Because streaming O^+ has a relatively low density ($\sim 10^{-3} cm^{-3}$), there are times when the temperature calculated for O^+ beams has a relatively large error. Therefore, it is important for us to know our limits in the calculated moments.

The core part of the temperature error calculation was written by C. Mouikis. The idea is to simulate the moment calculation by first finding the distribution function with particular moments input values (density, velocity and temperature), converting the distribution function into the counts data for each energy bin and angular bin with consideration of the instrument efficiency at each year and using the same format and instrument response as the real instrument, then deleting counts less than one and rounding the counts into
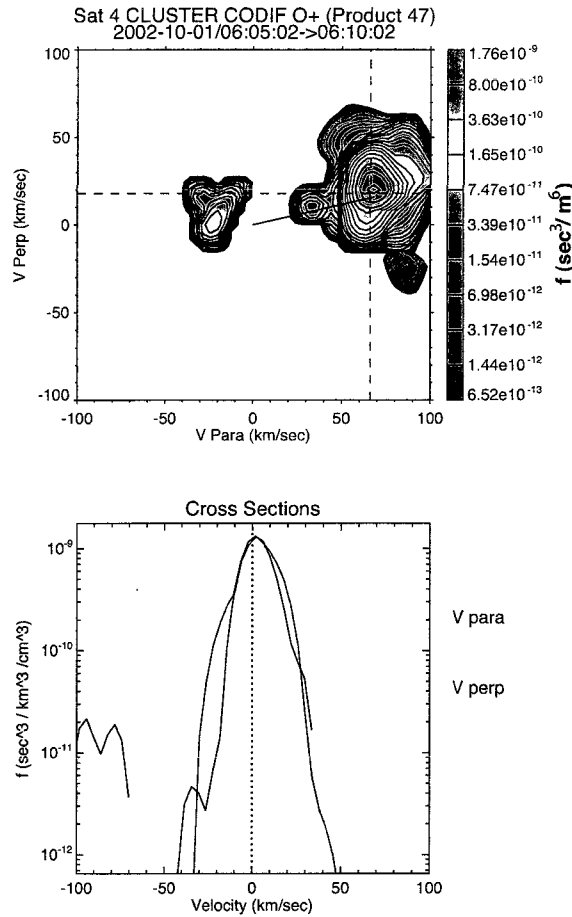
Figure 3-6: Phase space density of O^+ data averaged from Oct 0605UT 2001 to Oct 0610UT 2001. a) 2D phase space density; b) 1D velocity phase distribution for the stronger O^+ beam: black line is for parallel velocity and blue line is for perpendicular velocity. The cuts in panel (a) corresponds to panel(b)

integers, and in the end using this artificial data as an input to re-calculate the moments. Therefore, the original input moments are the true value and the difference between the calculated results and the true value gives the error of the moments.

Simulated Input Determination

Different density inputs are used to do the simulations. Here, we will only show two typical cases. The high density at 20 cm^{-3} shows the moment calculation uncertainty under ideal conditions while the low density at 0.002 cm^{-3} is used to give the confidence level for

calculated moment of the realistic streaming O^+.

Figure 3-6a is an example of phase space density ($s^3km^{-3}cm^{-3}$) of O^+ data averaged from Oct 0605UT 2001 to Oct 0610UT 2001. Figure 3-6a is the 2D phase space density with X-axis for parallel velocity and Y-axis for perpendicular velocity. The direction of the perpendicular velocity is chosen to maximize the magnitude of it. Two beams are observed at this time and they are in tailward ($V_\parallel \sim 70$ km/s and $V_\perp \sim 15$ km/s) and earthward($V_\parallel \sim$-20 km/s and $V_\perp \sim 0$ km/s) directions. Two different types of velocity distributions were tested in the simulation: the typical distribution for streaming O^+ (parallel and perpendicular velocities are 70%, 15% and 15% of the total velocity respectively as shown in figure 3-6a) and a velocity distribution with the same parallel and perpendicular components. It is found that it is the total velocity that affects the moment errors rather than the distribution of the velocity relative to the field direction. Hence, only the results from the typical velocity distribution input are shown.

The tailward O^+ beam is dominant so we concentrate on its analysis. We make a cut at the center of it and plotted the 1d phase space density in figure 3-6b. The black line shows the distribution of parallel velocity and blue line is for perpendicular velocity. The widths of the two distributions in 3-6b are comparable to each other, which means the observed O^+ beam has the same parallel and perpendicular temperature. A bigger survey (not shown here) of the phase space density of O^+ shows that the temperature distribution is isotropic most of the time. Comparison of the parallel and perpendicular distributions shows no obvious difference (may vary by a factor of 1/2 to 2), so in the following, we will only discuss the results with the typical temperature distribution for streaming O^+.

Time is also one of the inputs. The program reads the real magnetic field at the given time, but the value of magnetic field does not have any impact on the moment calculation results. The instrument coefficients are used when converting the distribution function back into the realistic counts units. As time goes by, the efficiency of the instrument is gradually decreasing. As a result, the minimum density that can be measured accurately in 2001 is less than in later years.

Simulation Methology

The simulation program first calculates the distribution function with the input density, velocity and temperature for each energy bin and energy bin:

$$f(energybin, angularbin) = \frac{n}{\sqrt{T_\parallel T_\perp^2}}(\frac{m}{2\pi})^2/3e^{\frac{-mV_\parallel^2}{2T_\parallel} - \frac{mV_\perp^2}{T_\perp}} \qquad (3.1)$$
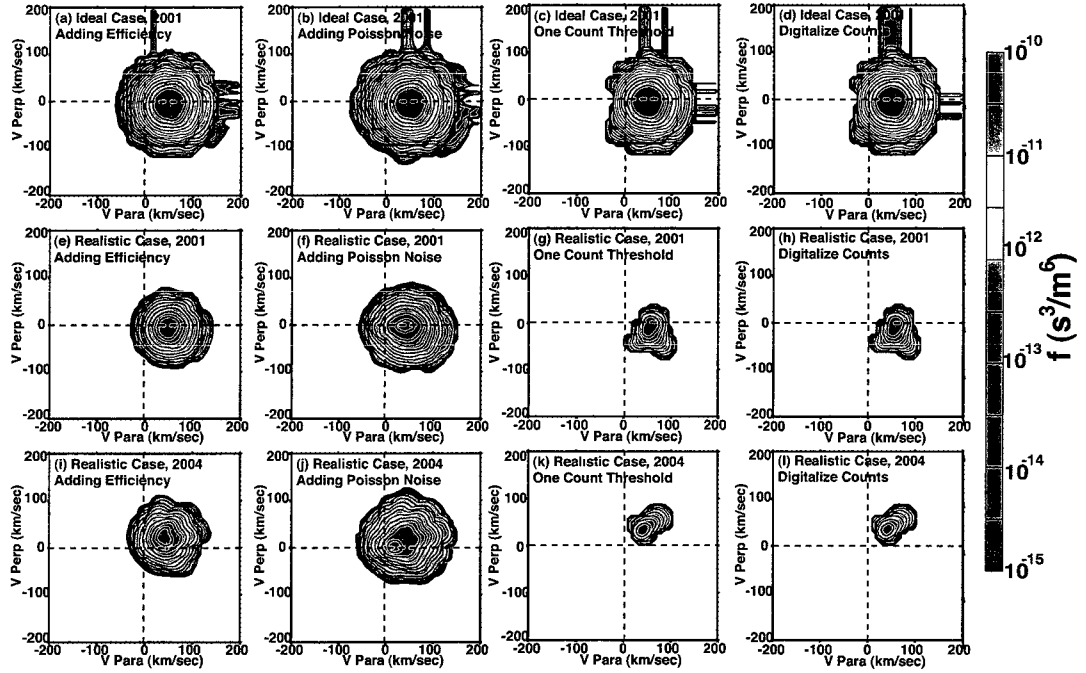
Figure 3-7: procedures in moment error simulation (a-d) with ideal density in 2001; (e-h) with realistic density in 2001; (i-l) with realistic density in 2004.

where, m is the mass of O^+, $T_\parallel$ and $T_\perp$ are the parallel and perpendicular temperature from the input, and $V_\parallel$ and $V_\perp$ are the parallel and perpendicular velocity in the instrument frame for a given energy bin and angular bin. It then calculates the energy flux based on the distribution function and the velocity that is calculated for each energy bin.

Figure 3-7 show the 2D distribution after each procedure in treating the data for ideal density (20 cm^{-3}) and realistic (0.002 cm^{-3}) density in 2001 and realistic (0.002 cm^{-3})

density in 2004. Velocity and temperature used in both cases are 69 km/s and 43 eV, which are the median value of all streaming O^+. Figure 3-7a, e and i show the distribution after converting energy flux into counts taking into account of the instrument efficiency. The distribution with lower density started with a less strong distribution as expected. Although the instrument efficiency decreased from 2001 to 2004, the distribution function of 2004 looks similar to the one in 2001 because of the calibration. Both the second and third case now have a clearly smaller density than the original one. In order to make the data more realistic, we added a Poisson noise, which is calculated by multiplying the square root of the count with a random generated noise. This noise is uniformly distributed random numbers between 0 and 1. Figure 3-7b, f and j show the distribution after adding the Poisson noise. Because data under one count cannot be detected, in order to make the counts more realistic, the program filtered everything lower than the one-count threshold and the results are shown in figure 3-7c, g and k. For the ideal case, as shown in figure 3-7a-d, during which the beam density is very high, these three procedures have little influence on the distribution, so as the velocity and the temperature. For the realistic case in 2001, as shown in figure 3-7e-h, after applying the one count threshold, only the center part of the distribution left. This change does not have a strong effect on the velocity but the temperature may be reduced. Although due to the calibration, the distribution function in 2004 is comparable to the one in 2001, the counts data are still small. Thus, after applying the one-count threshold, the distribution function for the realistic case in 2004 becomes even smaller than the one in 2001. Moreover, there is also a shift of the center of the distribution after adding the Poisson noise and applying the one count threshold, indicating that apart from a bigger error in the temperature there is now also an strong error in the bulk velocity measurement. Again, for both realistic cases, the total density has reduced again. Figure 3-7d, h and l show the distribution functions after the program digitalize the counts data. In all three cases, this procedure does not show strong impact on the distribution. Because of all the procedures above, the density now is well below the initial value. In order to regain back the input density, the program will start over again from calculating the distribution

function, but with a new input density that equals the old input density times a factor of 1.1. The loop will stop when the density is equal or bigger than the desired density. In the end of the day, we will have a realistic counts distribution with known moments.

The program then calculates the moments through the usual moment calculation routines with the artificial data and compares the results with the input moments. The error is defined as $(T_{true} - Tcalculated)/T_{true}$. Because the calculated temperature is usually lower than the true value as shown before, the error mostly ranges from 0 to 100%.

Moments Error Simulation Results

Figure 3-8, figure 3-9 show the result of the error calculation of velocity for ideal density (20 cm^{-3}) and realistic density (0.002 cm^{-3}) during different years while figures 3-10 and 3-11 show the error calculation of the temperature . The color represents the error so 0 means no error while 100% means error is same as the true value. The X-axis shows the thermal energy (temperature) while the Y-axis shows the bulk kinetic energy. The pink frames show typical the velocity and temperature range for the identified streaming O$^+$, which is obtain from figure 3-5.

For velocity, when density is very high, which represents the ideal condition, the error is near zero most of the time except when the velocity is very slow so the energy peak at the lowest energy bin and when the temperature is so high that it reaches the maximum energy. For realistic streaming O$^+$ density, because of the decreasing efficiency of the instrument, the error in the velocity becomes bigger and bigger over the years. Particularly, for very hot and slow O$^+$, the error can reach the 100%. Because the streaming O$^+$ has a beam-like distribution, most of the velocity error of the beam is around 30%. The error is especially low for streaming O$^+$ in the lobes, up to 20%. One exception is that when the energy of the beam peaks at the lowest energy bin of the instrument, because half of the distribution function is missing the error of the velocity reaches 100%. For very hot and relatively slow O$^+$ in the plasmasheet, the velocity error is also very large. Particularly in the later years, it can reach 100% as well. In 2009, however, the velocity error for those O$^+$ has reduced,

which is due to a increase of the efficiency. In July 2009, the CODIF microchannel plate high-voltage on spacecraft 4 was raised by ~80 V, which increased the particle detection efficiency by a factor of 2 and brought the efficiency back to the 2005 levels.

The temperature maps for ideal case are similar over the years: it is generally more accurate for hot O^+ than cold O^+. For realistic cases, the temperature error changes dramatically over the years. For the observed beams, the averaged temperature error increases from 30% to 70% from 2001 to 2009. Opposite to velocity error, temperature error is lower for O^+ in the plasma sheet than in the lobes. Similar as the velocity errors, the error of temperature in 2009 also reduced due to the efficiency increase. Here, we only showed cases with two different densities, but because the error of the moments strongly depends on the density, we have calculated the error distributions for different densities for future studies. The moment error calculation results are important and should be taken into account when doing a study with moments.
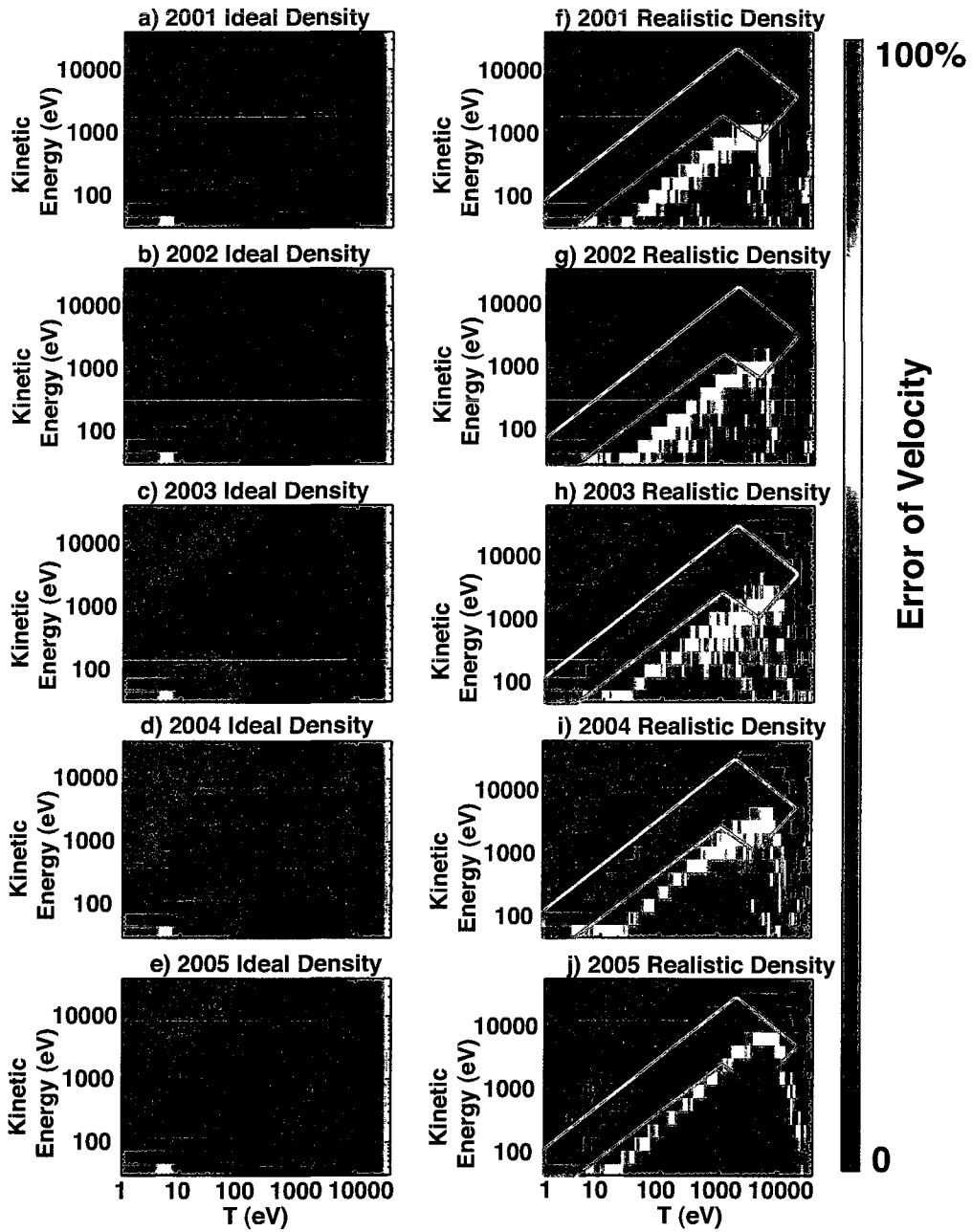
Figure 3-8: (a)-(e) and (f)-(j) show the O^+ velocity error simulation results from 2001 to 2005 for ideal density (20 cm^{-3}) and realistic streaming O^+ density (0.002 cm^{-3}) dependent on bulk kinetic energy and temperature. Pink frames show the typical values for observed streaming O^+.
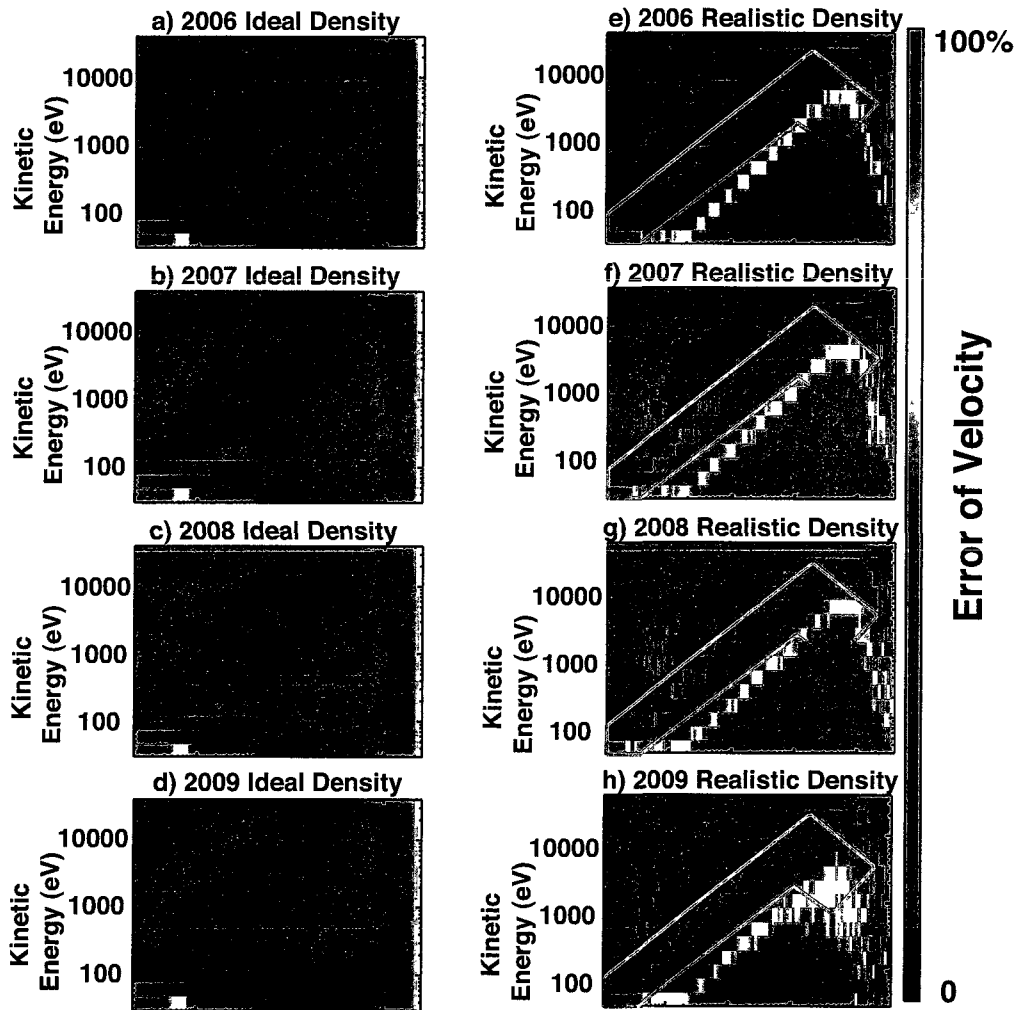
Figure 3-9: (a)-(d) and (e)-(h) show the O^+ velocity error simulation results from 2006 to 2009 for ideal density ($20\ \mathrm{cm}^{-3}$) and realistic streaming O^+ density ($0.002\ \mathrm{cm}^{-3}$) dependent on bulk kinetic energy and temperature. Pink frames show the typical values for observed streaming O^+.
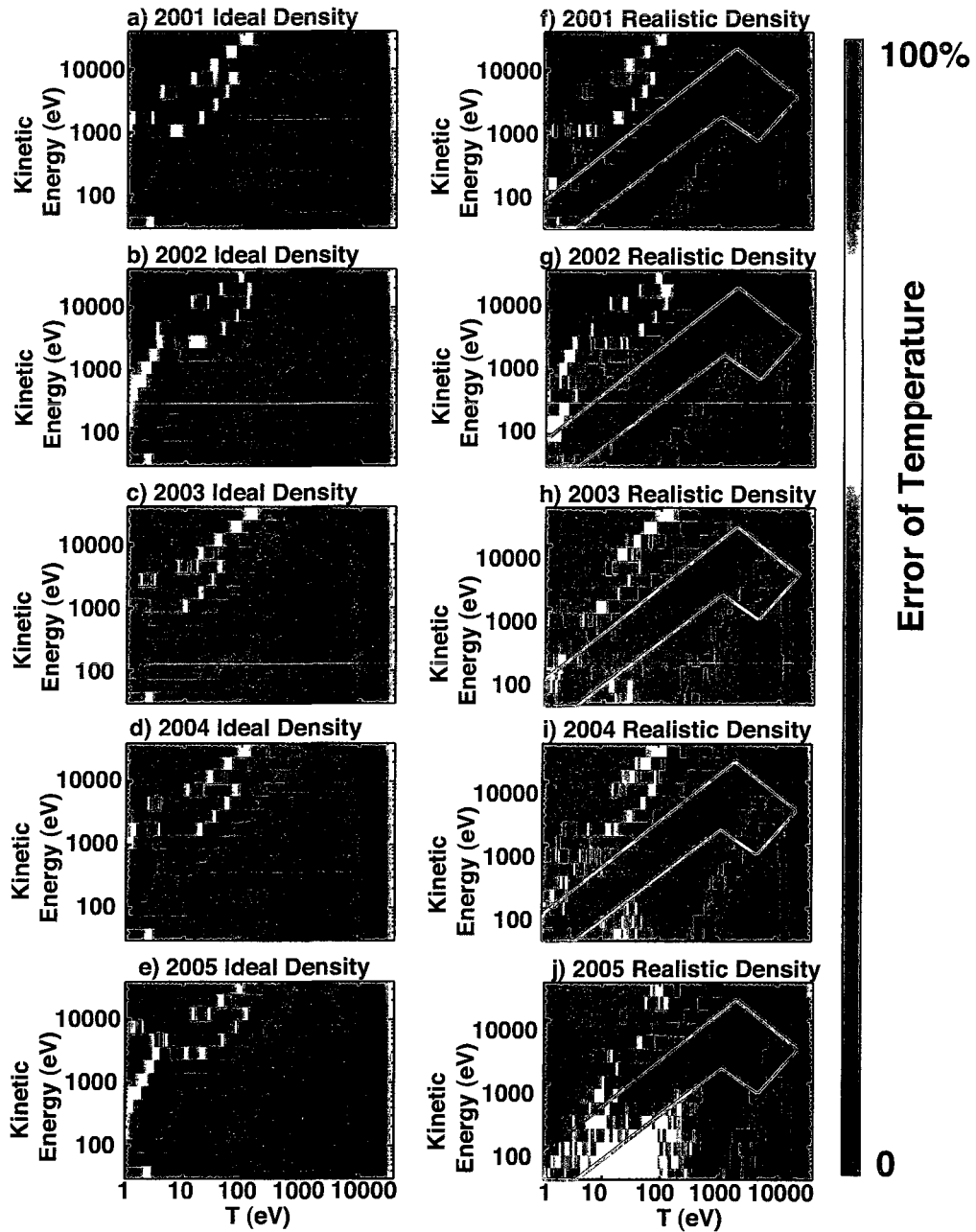
Figure 3-10: (a)-(e) and (f)-(j) show the O^+ temperature error simulation results from 2001 to 2005 for ideal density (20 cm^{-3}) and realistic streaming O^+ density (0.002 cm^{-3}) dependent on bulk kinetic energy and temperature. Pink frames show the typical values for observed streaming O^+.
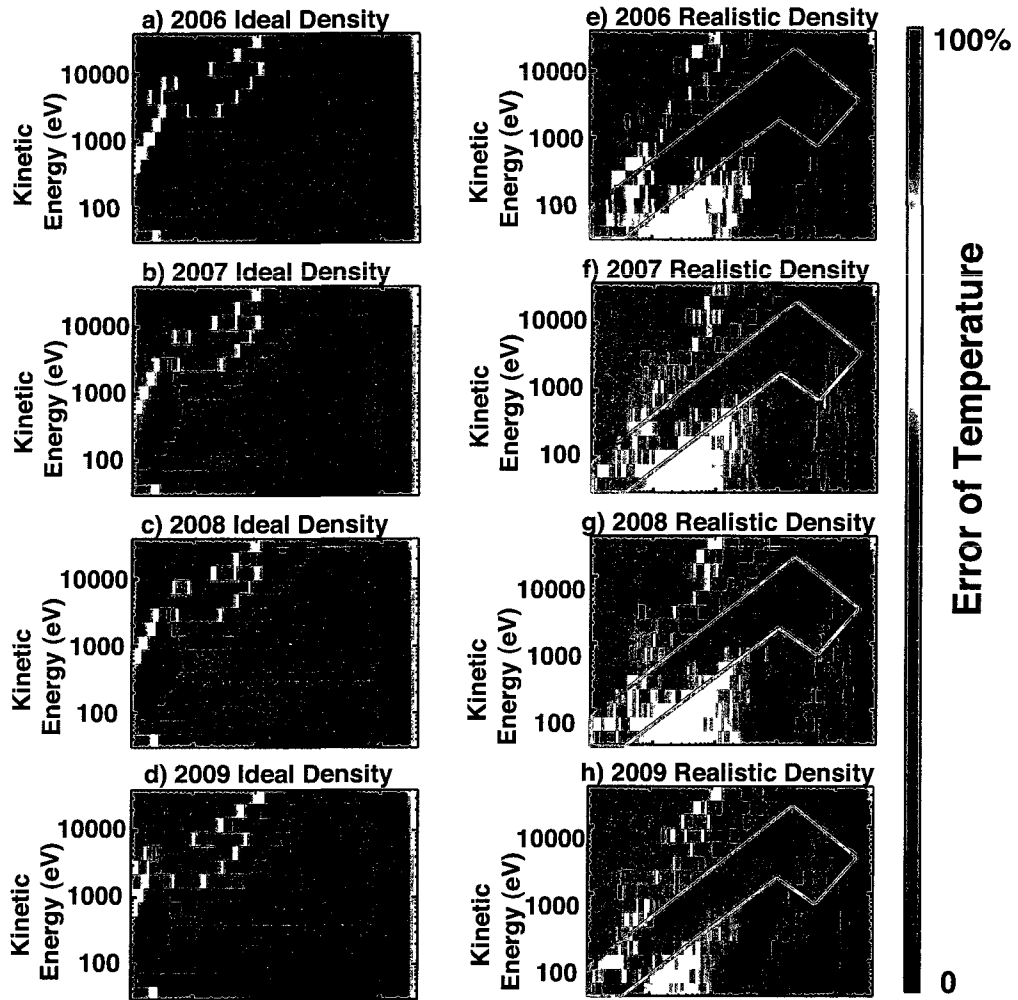
Figure 3-11: (a)-(d) and (e)-(h) show the O^+ temperature error simulation results from 2006 to 2009 for ideal density (20 cm^{-3}) and realistic streaming O^+ density (0.002 cm^{-3}) dependent on bulk kinetic energy and temperature. Pink frames show the typical values for observed streaming O^+.

3.4 Survey of Storm Phases and External Conditions

To determine how the O^+ outflow changes when a storm occurs, we first divided the data into storm and non-storm times, and then we divided the storm-time data by storm phase. In this study, we used the criteria that the minimum Dst must be less than -50 nT to be considered a geomagnetic storm. With those criteria, there were 71 storms during 2001-2002 and 191 storms for all 9 years. Storms with multiple dips in Dst are considered to be multiple storms with two main phases. From 2001 to 2002, 27 of the storms occurred during the tail season (middle July to end of October) of CLUSTER when the apogee of the satellites passed through the magnetotail. 70 storms occurred during the tail season for all 9 years. Using the ACE magnetic field data (Bz component) and the solar wind pressure and Dst index, we divided the storm period into three phases: initial phase, from the sudden increase in solar wind parameters (primarily pressure) to the storm onset (defined as the beginning of the drop in Dst); main phase, from the storm onset to the minimum Dst; and recovery phase, from the minimum Dst to the time when the Dst is back to a non-storm level. The initial phase will be omitted if there is no sudden increase in the solar wind parameters observed. The non-storm level of Dst is defined as either higher than 2/3 of the minimum Dst or -20 nT in Dst, whichever is satisfied first. These times were used to divide the data in the statistical analysis.

Proton density, velocity and temperature calculated with CODIF data are also included as external conditions. IMF and solar wind pressure and velocity data used in this analysis are the average values over the previous 1-hour time period, with ACE data that has been propagated to the subsolar point.

3.5 Database

By running our identification routine and moment calculation routine for the data from March 2001 to December 2009, we were able to build a time-based database with identification results, moments of the streaming O^+ and external conditions when observing the

streaming O^+.

To limit the data to regions inside the magnetopause, we exclude the magnetosheath using criteria that the proton density is greater than 3 cm^{-3} and the proton velocity is greater than 65 km/s, and we only kept the data inside the spatial region $(((X_{GSE} + 1)/8)^2 + ((Y_{GSE} - 1)/14)^2) < 1$ or $X_{GSE} < -1R_E$ to avoid the upstream region.

3.5.1 Statistics of the Identification Result

From 2001 to 2009 there are 381035 5-minute samples inside the magnetosphere during non-storm times, with 71428 of them containing signatures of streaming O^+. We call the 5-minute samples that contain streaming O^+ "O^+ event". For the storm times, there are 41642 5-minute samples with 18962 of them being streaming O^+ events. Figure 3-12 shows the histogram with the total number of samplings and number of the streaming O^+ events from 2001 to 2009 during nonstorm time and storm time. There are more events during nonstorm times, but the relative ratio of identified streaming O^+ over the total samples during storm time is higher than nonstorm time, indicating that the occurrence of streaming O^+ is correlated with geomagnetic activity level. There are more data collected during nonstorm times because the accumulated time during storm time periods is much shorter than the accumulated nonstorm times. There was not full-time data coverage during 2001 so there are fewer data obtained during 2001 for both active and nonactive times. There are fewer storm time samples during 2004 and 2009 because of the declining phase of solar cycle 23. Although there is more data collected in later years during nonstorm times, there are fewer O^+ beams identified because the Sun is less active. More discussions about the correlation of streaming O^+ events with magnetic storm and solar cycle are in chapter 4 and chapter 6.

3.5.2 Statistics of the Properties of O^+

Table 3.1 lists the median values of the moments of the identified streaming O^+ in different magnetosphere regions during different geomagnetic active levels as well as related
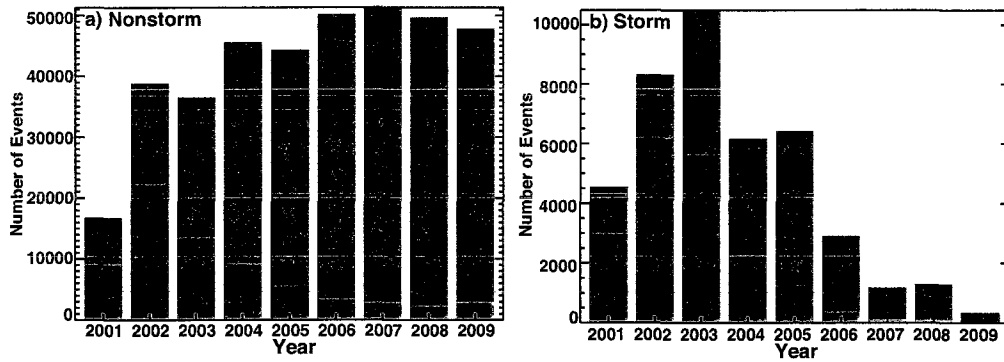
Figure 3-12: Histogram of events from 2001 to 2009 for (a) nonstorm times and (b) storm times. Dark blue plots show the number of all samples while light blue plots show the number of streaming O^+ events detected.

Geomagnetic Active Level	Regions	n (cm^{-3})	V (km/s)	T(eV)	Flux (10^4cm^{2}s^{-1})
	Lobe	0.009	40.5	9	3.79
Nonstorm Time	PSBL	0.002	131.0	379	2.56
	Plasmasheet	0.001	218.1	2409	2.41
	Lobe	0.014	45.4	9	5.87
Storm Main Phase	PSBL	0.005	133.7	384	5.96
	Plasmasheet	0.003	212.7	1649	6.34
Seki et al. [68]	$0 \sim 220R_E$	0.0036	107.93	24.4	/
Engwall et al. [21]	$0 \sim 20R_E$	0.18	32	/	39
Kistler et al. [37]	$200 \sim 300R_E$	0.00028	500	10^5	1.4

Table 3.1: Median values of the density, bulk velocity, temperature and flux of streaming O^+ observed in the lobes, the PSBL and the plasmasheet during nonstorm time and storms

observations from other papers. The cold O^+ beams studied by Seki et al. [68] are observations from Geotail, so the locations of the O^+ beams are up to -220R$_E$. The low energy population identified by Engwall et al. [21] with Cluster are mostly H$^+$ from 1∼60 eV. Kistler et al. [42] studied the O^+ in the distant plasmasheet with STEREO. In our study, the density is highest for O^+ beams in the lobe and lower in the PSBL and the plasmasheet, which may be due to the combination effect of the velocity filter effect and the acceleration and enhanced drift in the PSBL and the plasmasheet. The density is also higher during storm time than nonstorm times, consistent with the fact that ionospheric

outflows increase during active time. The value is comparable but slightly higher than the O^+ beams observed by Seki et al. [68] supporting that those two populations may from the same source region. The velocity is lowest in the lobes around 40.5~45.4 km/s. which is close to the velocity of the low energy population observed by Engwall et al.[21]. Due to the velocity filter effect and the regional differences, we do not expect any similarity between our velocity and the velocity of the population studied by Seki et al. [68] or Kistler et al. [42]. The temperature difference is very dramatic between the lobes, the PSBL and the plasmasheet, indicating that acceleration and heating may happen to O^+ beams inside the PSBL and the plasmasheet. It is interesting that the temperatures are similar for streaming O^+ observed during the nonstorm and storm times. The flux is calculated by multiplying density with velocity. The flux is similar during all times at different regions and the value is only about 2 times bigger than the flux calculated by Kistler et al. [42]. It implies that a large fraction of the the lobe streaming O^+ will be lost in the distant tail.
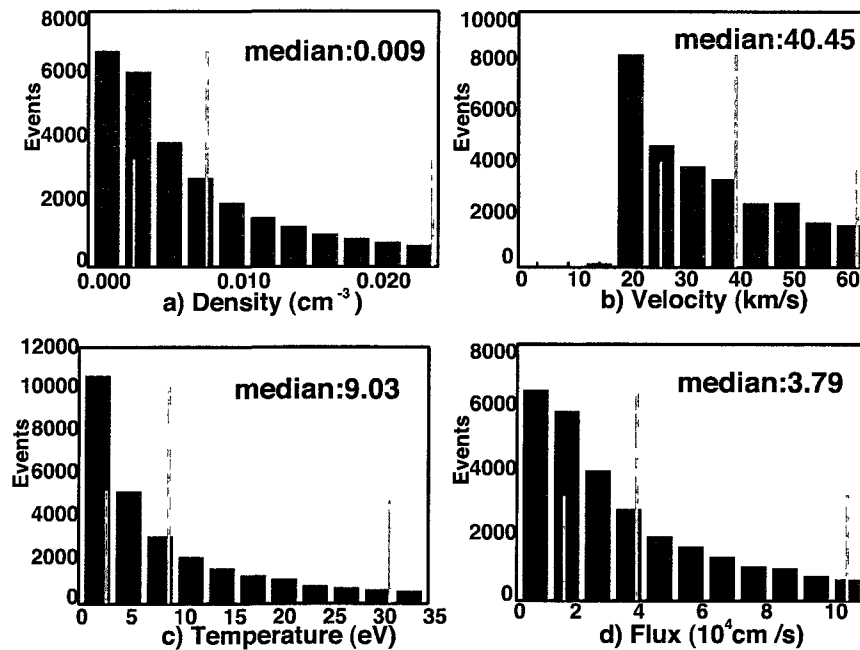
Figure 3-13: Histogram of density, velocity, temperature and flux during 2001-2009 for nonstorm times and storm times. Flux is calculated by multiplying density and velocity. Three pink lines in each plot shows the first, second and third quartile.

Figure 3-13 shows the statistical distributions of nonstorm time lobe region steaming O^+ moments· (a) the density, (b) velocity, (c) temperature and (d) flux, calculated by multiplying density and velocity. Three pink lines in each plot show the first, second and third quartiles. It is shown in the density histogram, figure 3-13, that most of the streaming O^+ have a very low density because 75% of them are below 0.015 cm^{-3}. The velocity distribution is cut around 15 km/s, which may be due to the low energy limit of the instrument. The O^+ outflows have an escape velocity at about 10km/s, so we do not suspect a large amount of O^+ is below our energy range. The error of the beam velocity will be low if the temperature is not too high according to figure 3-8 and figure 3-9 . Similarly, the temperature of the streaming O^+ are mostly in the very low range, where 70% of the uncertainty is expected. A more detailed discussion of the characteristic properties of the streaming O^+ is in chapter 4.

Chapter 4

SPATIAL DISTRIBUTIONS

In this chapter we discuss the spatial distribution of the transport path of O^+ outflow from the cusp using Cluster/CODIF data from 2001 to 2002. Data in this analysis is limited to the solar maximum time (March 2001 - Dec 2002) so solar cycle does not play a role in the result of this analysis. We show the dependence of the spatial distribution of the transport path of the O^+ on the geomagnetic active level, IMF and other drivers. Moreover, in order to focus here on the transporting, we also restrict the data to the lobes in most part of study. Streaming O^+ inside the plasmasheet and the PSBL will only be discussed in the previous section of the chapters.

4.1 Occurrence Frequency Map

During 2001-2002, we have identified 70 storm-time periods, 27 of which occurred when CLUSTER has extended coverage in the magnetotail with most of the plasmasheet crossings occurring close to -19 R_E. We obtained 156962 5-minute samples in the lobes during nonstorm times with 49000 of them classified as streaming O^+ events. During storm times, there were 23679 5-minute samples with 11199 of them classified as streaming O^+ events.

Figure 4-1 shows the distribution of 5-minute samples in the lobe and polar cap, summed into 1 R_E X 1 R_E bins in the XZ_{GSM} planes for different Y_{GSM} slices and different storm phases. Figure 4-1a to 4-1c show the number of samples for nonstorm times for three slices in Y_{GSM}: -12 to -4 R_E (the dawn side), -4 to 4 R_E (noon-midnight meridian) and 4 to 12 R_E (the dusk side). Figure 4-1d to 4-1f show the sample distributions for storm main phases, and Figures 4-1g to 4-1i show them for recovery phases, for the same slices in Y_{GSM}.
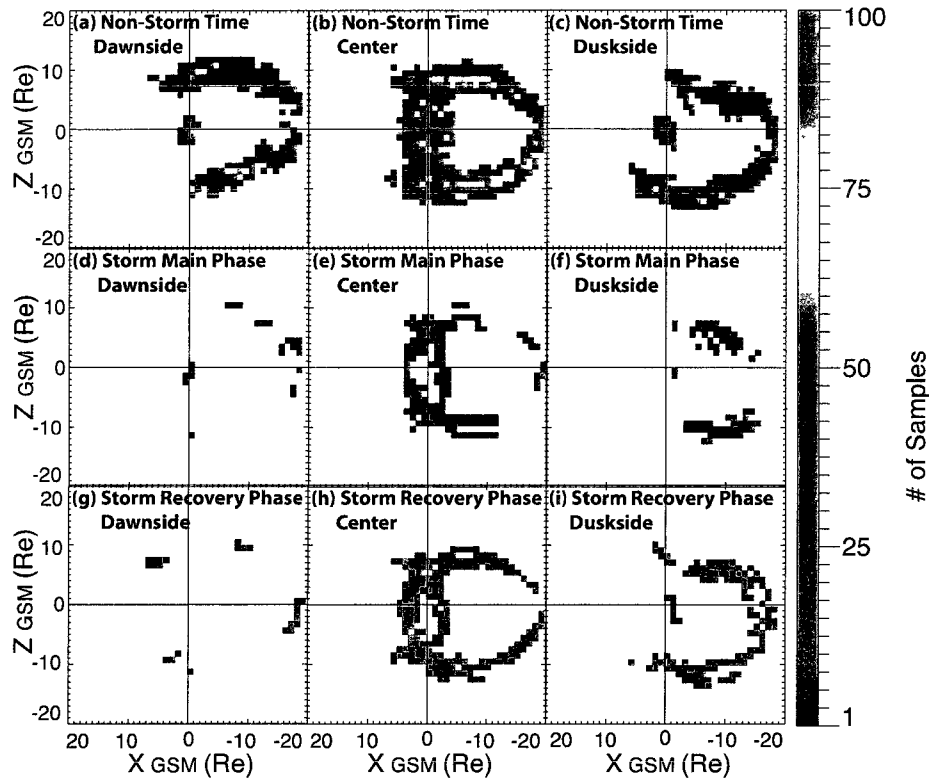
Figure 4-1: Maps show samples in the lobe and polar cap projected in the XZ_{GSM} plane and sliced in Y_{GSM} directions for three different geomagnetic storm active levels. Three rows from top to bottom are for: nonstorm times, storm main phase and storm recovery phase. Three columns are for threes slices in the Y_{GSM} direction. The columns from left to right show: the dawn side (-12 R_E < Y_{GSM} < -4 R_E), the center region (-4 R_E < Y_{GSM} < 4 R_E) and the dusk side (4 R_E < Y_{GSM} < 12 R_E). Data are from March 2001 to December 2002 in regions identified as the lobe and polar cap (plasma beta less than 0.05). The grid is 1 × 1 R_E.

Because there is significantly less accumulated time during storm main phases and recovery phases compared to nonstorm times, most of the samples occur during nonstorm times. The reason for the small number of events in the equatorial plane inside of 15 R_E is simply due to the polar CLUSTER orbit, which does not pass that region in 2001 and 2002. By comparing figure 4-1d with 4-1f, and figure 4-1g with 4-1i, we find that most of the storms occurred when the spacecraft was on the duskside. Thus we cannot compare dawnside and duskside distributions during storm times.

Figure 4-2 shows the distributions of identified 5-minute O^+ streaming events organized
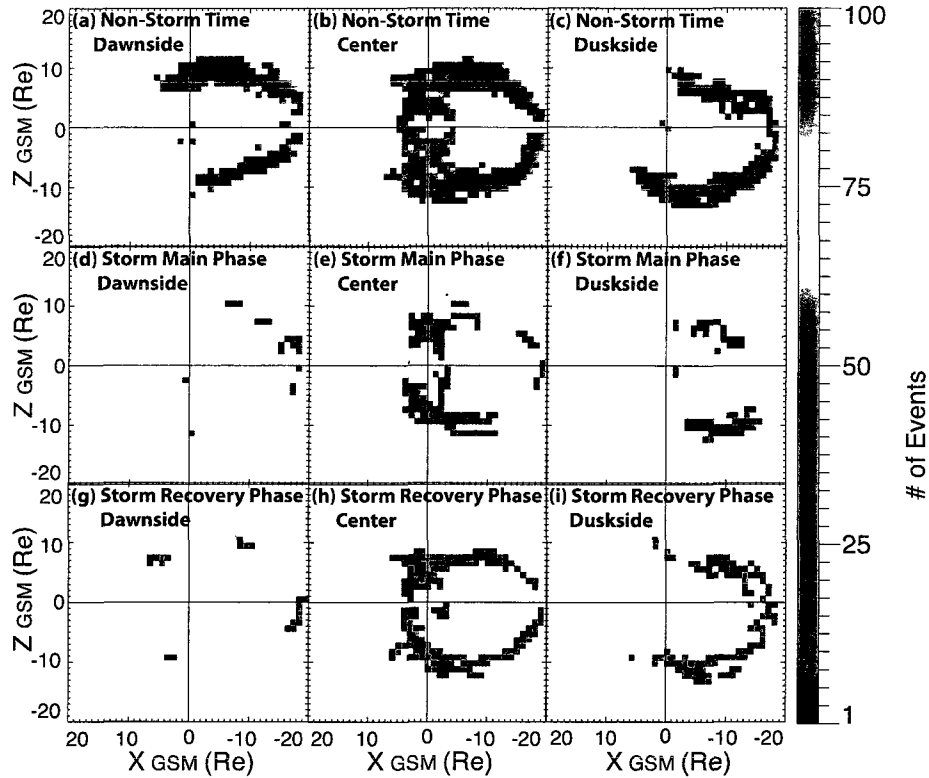
Figure 4-2: Maps show the number of 5-minute streaming O^+ events in the lobe and polar cap projected in the XZ_{GSM} plane and sliced in Y_{GSM} directions for nonstorm times, storm main phase and recovery phase. Map arrangement is the same as figure 4-1.

in the same way as in figure 4-1. The number of events during nonstorm is clearly reduced from those shown in Figure 4-1. The storm-time distributions look almost the same, indicating that almost all samples during storm times contained the mono-energetic streaming O^+. To determine this more quantitatively, figure 4-3 shows maps of the occurrence frequency of the streaming O^+ in the XZ_{GSM} plane. Occurrence frequency is defined as the number of 5-minute streaming O^+ events observed in a particular bin divided by the number of 5-minute samples that were made in that bin. It gives the fraction of the time we would expect to see streaming O^+ in that bin, or the probability that we would observe a streaming O^+ at a particular location. In the occurrence frequency maps, bins in white have no data coverage while dark blue means zero occurrence frequency. As in figures 4-1 and 4-2, only
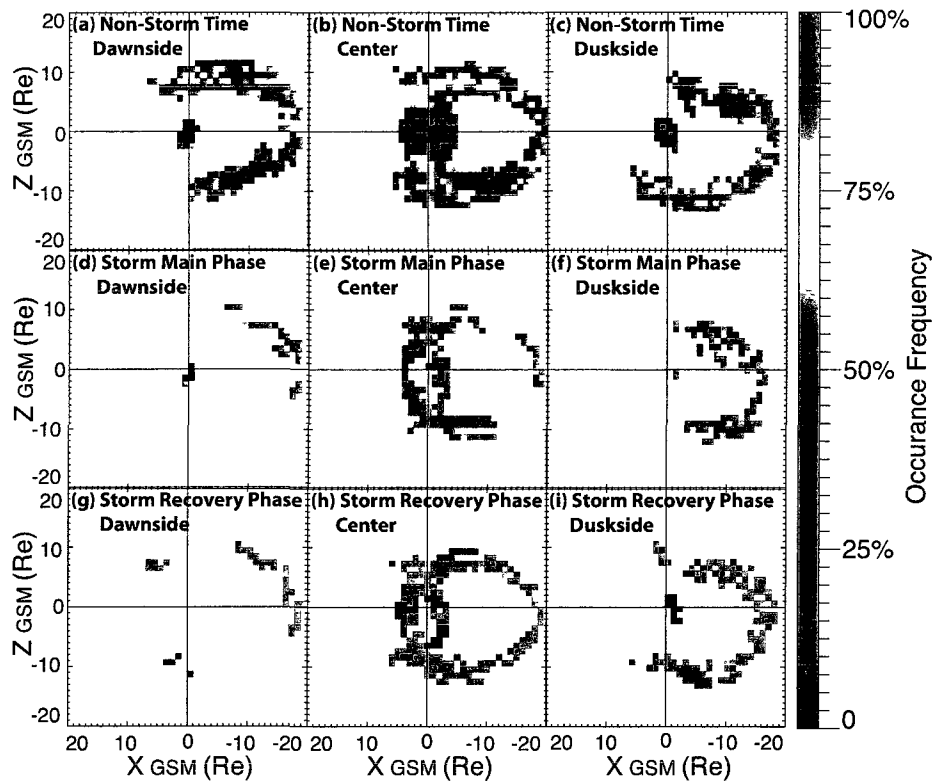
Figure 4-3: Occurrence frequency maps of streaming O^+ in the lobe and polar cap projected in the XZ_{GSM} plane and sliced in Y_{GSM} directions for three different geomagnetic storm active levels (nonstorm times, storm main phase and recovery phase). Map arrangement is the same as figure 4-1. Bins in white have no sample while dark blue means zero occurrence frequency.

data within the spatial region identified as tail lobes or polar cap (beta < 0.05) are used. The panels are organized in the same way as figure 4-1 and 4-2. The maps show the most probable locations where the streaming O^+ can be observed over the CLUSTER orbit. No bins are excluded for statistical reason. However, as can be seen in figure 4-1, there are bins, particularly close to the edges of the spatial distributions, where the number of samples is very low (some bins even have only one sample). Thus, the statistical errors for those bins are very high and the maps in figure 4-3 have to be interpreted taking into account the sample distributions in figure 4-1. Although the data coverage during the storm phases are not as good as during nonstorm times, at the locations with good coverage for all times,

the frequencies can still be compared. We find that a significant fraction of the samples containing O^+ events occur during nonstorm times (figures 4-3a to 4-3c). There are many regions with occurrence frequency higher than 70%, as shown in yellow and there are even places with nearly 100% of observing streaming O+ in the south region of the center. It indicates that streaming O+ is a very common feature even when there is no storm. This result is consistent with the result in Liemohn::2005 by Liemohn et al. showing that the observation of cold ion beams in the near-Earth magnetotail is very often. Moreover, the occurrence frequency increases greatly from nonstorm times to storm main phase (figure 4-3d to 4-3f) and recovery phase (figures 4-3g to 4-3i) times.
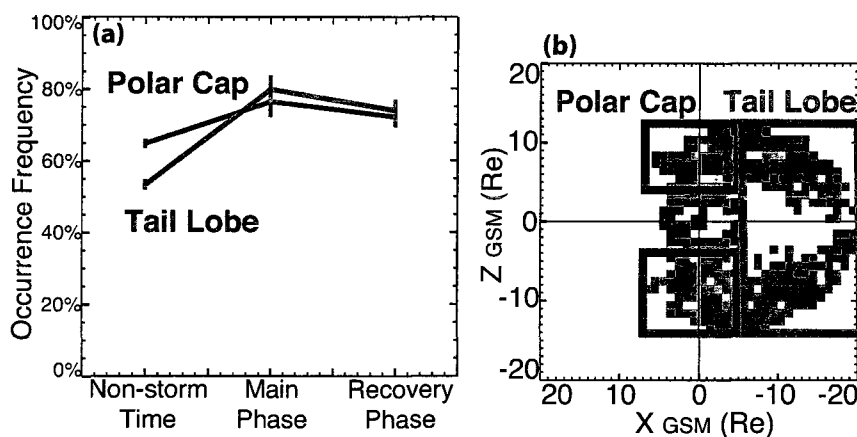
Figure 4-4: (a) Occurrence frequency VS geomagnetic storm active levels for polar cap region (blue) and tail lobe region (green). The error bars here are standard deviation. (b) One example map, with the definition of polar cap regions (blue) and tail lobe region (green) shown on the map. Bins in white have no sample while dark blue means zero occurrence frequency.

In order to study this dependence more quantitatively, figure 4-4 shows the overall occurrence frequency in two regions, the polar caps and tail lobes, during nonstorm times, storm main phase and storm recovery phase. Polar caps here are defined as X_{GSM} between 10 R_E and -5 R_E, $|Z_{GSM}|$ greater than 4 R_E and plasma beta less than 0.05, and tail lobe are defined as X_{GSM} between -5 R_E and -20 R_E and plasma beta less than 0.05. There

is no Y_{GSM} limit. Blue boxes in Figure 4-4b show the polar cap regions in the north and south, while the green box shows where the tail lobe region is defined. Figure 4-4a shows the occurrence frequency versus a pseudo-time scale of geomagnetic active level inside the polar caps (blue) and tail lobes (green), using data in the full region for the calculation. The error bars are one standard deviation. As previously discussed, the occurrence frequency shows strong dependence on geomagnetic storm activity. It is the lowest during nonstorm times, highest during storm main phase and reduced during recovery phase but still higher than nonstorm times. If we use occurrence frequency during nonstorm times as a base line, in the polar cap region, the probability to observe streaming O^+ goes up from 64.0% to 79.3% during main phase and back to 72.7% during recovery phase. The increase of occurrence frequency during storm times in the tail lobes is even higher than over the polar cap. It increases from 47.4% to 78.5% during main phase and back to 70.7% during recovery phase. The stronger geomagnetic storm activity dependence in the tail lobe region indicates that not only does the O^+ outflow increase during storm times but also the fraction of the O^+ transported to the near-Earth tail increases. Those O^+ is a direct source for the ionospheric ions in the plasmasheet during storm time, even before the increase of the ionospheric outflows access the plasmasheet.
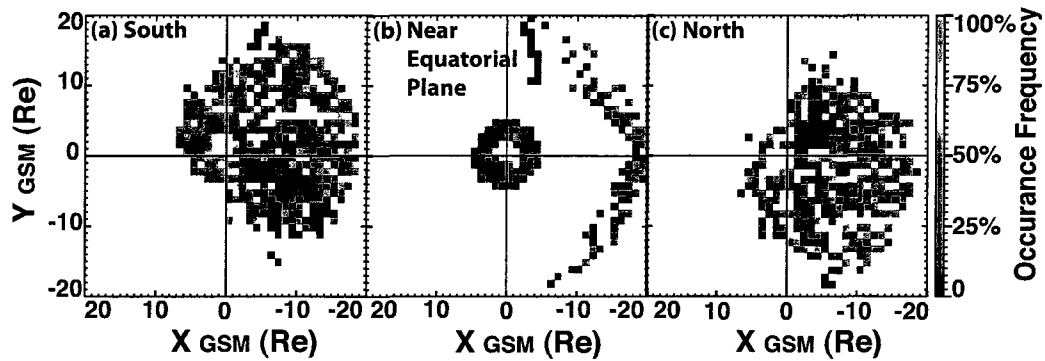
Figure 4-5: Nonstorm times occurrence frequency maps of streaming O^+ in the XY_{GSM} plane, sliced for different Z_{GSM}: South (-12 R_E < Z_{GSM} < -4 R_E), Near Equatorial Plane (-4 R_E < Z_{GSM} < 4 R_E) and North (4 R_E < Z_{GSM} < 12 R_E). Bins in white have no sample while dark blue means zero occurrence frequency.

Because the nonstorm times have the best statistics and the data coverage in storm main phases and recover phases is uneven in local time distribution, we have used the nonstorm times data set to study the transport path in detail. The spatial distributions during nonstorm times show that most of the dawnside ($Y_{GSM} <$ -4 R_E) O^+ is observed in the north of the magnetosphere as shown in Figure 4-3a while in Figure 4-3c most of the O^+ in the dusk ($Y_{GSM} >$ 4 R_E) is observed in the south; at the center ($-Y_{GSM}- <$ 4 R_E), as shown in Figure 4-3b, the occurrence frequency in the north is around 70% from the dayside cusp to the magnetotail while in the south the frequency in the polar region is obviously higher than in the tail. The duskside distributions during the storm main phases and recovery phases also show a greater occurrence in the south. However, there are not enough storms occurring when the spacecraft was on the dawnside to compare dawn and dusk. This asymmetric trend in the transport is also evident in Figure 4-5, which shows
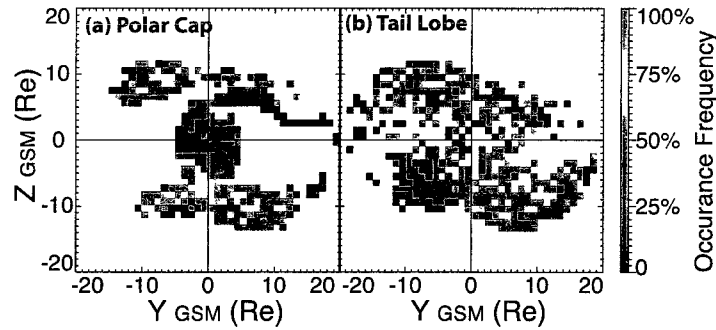
Figure 4-6: Nonstorm times occurrence frequency maps of streaming O^+ in the YZ_{GSM} plane, integrated over X_{GSM} from 10 R_E to -5 R_E for polar cap region as shown in (a) and from -5 R_E to -20 R_E for tail lobe region as shown in (b). Maps are viewed from the Sun to the Earth. Bins in white have no sample while dark blue means zero occurrence frequency.

the nonstorm times occurrence frequency maps in the XY_{GSM} plane, divided in slices in Z_{GSM}. Again, most of the O^+ in the southern magnetosphere is transported towards the duskside. In the north, the distribution is spread more uniformly in Y_{GSM}. Figure 4-6 shows the occurrence frequency in the YZ_{GSM} plane, integrated over X for the polar cap region (10 to -5 R_E), in figure 4-6a, and the tail lobe region (-5 to -20 R_E), in figure 4-6b.

All maps in the YZ_{GSM} plane in this paper are viewed from the Sun to the Earth. The occurrence frequency of streaming O^+ is again observed to be higher in south-dusk and north-dawn for both polar cap and tail lobe maps. Hence the latter maps in the YZ_{GSM} plane are integrated over all X.

4.2 Transport Path Dependence on Geomagnetic Active Level

This paper for the first time gives a clear picture of the transport of O^+ over the polar cap and into the tail lobes to the near-Earth ($\sim$-19 R_E) plasmasheet. As shown in figure 4-3 and discussed in the previous section, the streaming O^+ from the dayside cusp can almost always be observed over the polar caps and in the lobes inside -20 R_E during storm main phase and recovery phase. The ions are also observed during nonstorm times, with a lower occurrence frequency. The increase in occurrence frequency, especially in the lobes, with storm main phase, as shown in Figure 4-4a, supports that O^+ from the cusp plays an important role in the storm formation, as discussed by Kistler et al. [42]. The occurrence frequency of O^+ in the lobe increased more from nonstorm times to the storm main phase than the O^+ in the polar cap, which may indicate that the transport path itself is changing to bring O^+ into near-Earth lobe during geomagnetic active time. The higher convection inside the magnetosphere during storm main phase would be expected to bring more of the O^+ to the near-Earth plasmasheet, as shown by [34].

To study the dependence of the O^+ transport on geomagnetic active level further, we calculated the integrated occurrence frequency for storm and nonstorm times in the polar cap and tail lobe regions as a function of geomagnetic indices. Polar cap and tail regions are defined the same as in figure 4-4, for nonstorm times and storm times. Figure 4-7 shows the plots of occurrence frequency as function of Kp index, figure 4-7a-b, and AE index, figure 4-7c-d. The error bar is, as in figure 4-4, one standard deviation. We did not plot the correlation for F10.7 and Dst Index here because we already limited the solar cycle to the solar maximum time and limited the storm conditions by manually sorting the storm phases. As expected, occurrence frequencies in both polar cap and tail lobe regions have

51
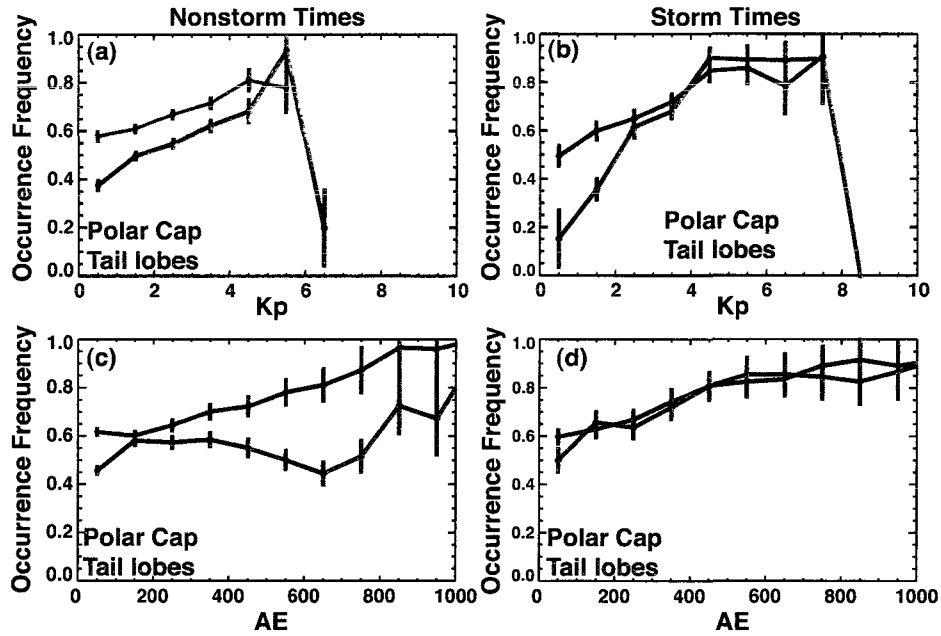
Figure 4-7: Occurrence frequency VS Kp index and AE index during nonstorm and storm times.

positive correlations with Kp index during both nonstorm times and storm times. The result is consistent with the findings by Yau et al. [78] of the correlation between outflow rate and Kp index for solar maximum period. Abe et al.[1] found that the O^+ ion integrated flux, in s^{-1}, below 75° invariant latitude correlates positively with Kp while the rate above 75° invariant has weak or no dependence on Kp index. Similar results were obtained by Cully et al. [15] where he showed that the mean net outflow rate, known as fluence, of both net or upward O^+ ion flows, positively correlate with Kp index after the F10.7 effect was removed. Occurrence frequency, different from outflow rate, merely represent how often O^+ can be seen at certain region without taking the intensity of flux into account. Hence, the positive correlation between occurrence frequency and Kp shows that a stronger magnetic active environment will cause O^+ outflow to last for a longer time. The occurrence frequency in the tail lobes is typically lower than over the polar cap during nonstorm times while the slope is similar, which means during nonstorm times the fraction of the O^+ from the cusp to the tail lobes does not change much even when the magnetosphere is more active. Figure

52
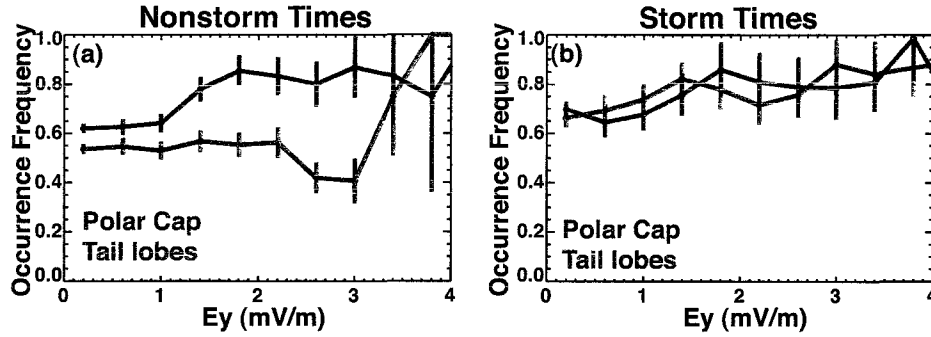
Figure 4-8: Occurrence frequency VS solar wind electric field Ey component during non-storm and storm times. Ey is the product of southward IMF B_z and solar wind speed.

4-8 shows the similar occurrence frequency correlation plots as a function of Dawn-Dusk Ey. Ey here is calculated by multiplying southward IMF B_z and solar wind speed. All IMF and solar wind data used in this paper are the averaged values over the previous 1-hour time period, using ACE data that has been propagated to the subsolar point. As shown with the green line in figure 4-8a, for nonstorm times, the occurrence frequency of O^+ in the tail lobes has no dependence on Ey when Ey is less than 2 mV/m, negative correlation with Ey when Ey is between 2 to 3 mV/m and a positive correlation again when Ey is bigger than 3 mV/m. Moreover, during nonstorm times, the occurrence frequency of tail lobe O^+ is also independent of AE when AE is smaller than 300, has a negative correlation with AE if AE is between 300 and 650 and a positive correlation when AE is greater than 650, as shown with the green line in figure 4-7c. The two line plots are similar. The results indicate that substorm activities may affect the O^+ transport but the correlation is non-monotonic. At very quiet times, there is no dependence between the convection field and the fraction of the O^+ that gets into the tail lobes because the change of the transport path is small. Substorms are associated with both increased convection field and AE. One possible explanation is that the combination of the increased cusp outflow and the stronger convection cannot replenish the amount of lobe O^+ that is convected into the plasmasheet due to the reconnection in the tail, leading to the reduction in lobe O^+. Another possibility is that while the outflow increases slightly, the stronger convection field drags the O^+ in the

lobes further inward, which leads Cluster to observe more energetic O^+ ions with weaker flux. Those low flux O^+ may thus be missed by CODIF. When the convection becomes even stronger, larger than 3 mV/m. stronger substorms occur and AE goes up to 650. The occurrence of O^+ ions in the near-Earth lobes will increases again because now the increases in the supply of O^+ outweighs the loss.

During storm times, the occurrence frequency correlates well with the Kp index, as shown in figure 4-7b, both in polar cap and tail lobes, with a steeper slope for the tail lobe O^+. When Kp is very low, even during storm phases, a large fraction of the O^+ does not arrive in the near-Earth lobes. When Kp is larger than 2, which is more normal during storm times, the occurrence frequencies of polar cap and tail lobes are almost the same and both increase as the Kp increases. It indicates that there is nearly no loss of O^+ from polar cap to tail lobes. Similarly, the occurrence frequency correlates with AE index positively for both polar cap region, and tail lobes region and the two correlations are almost identical. Within the range of the error bar, during storm time, the correlations between occurrence frequency and Ey for two regions are similar as well: both increase slightly as convection field Ey becomes stronger. Thus, during storm times, most of the O^+ observed in the polar cap also enters the near-Earth tail lobe region. The loss of O^+ is very small. Compared with nonstorm times, the transport of O^+ is more effective in moving O^+ from the cusp to the near-Earth tail, and the O+ may then be trapped into plasmasheet, and become the source of storm times ring current.

4.3 Drivers for a More Effective Transport Path

The effect of IMF B_z as a major driver for the geomagnetic storm is well known, as discussed in the introduction. In order to study the influence of the IMF direction on the transport path of O^+ from the cusp to the plasmasheet, we have plotted the occurrence frequency as a function of IMF B_z, IMF B_y, IMF B magnitude, IMF clock angle, solar wind pressure and solar velocity in figure 4-9, figure 4-10 and figure 4-11.

Figure 4-9 shows how the occurrence frequency changes with IMF B_z and IMF B_y
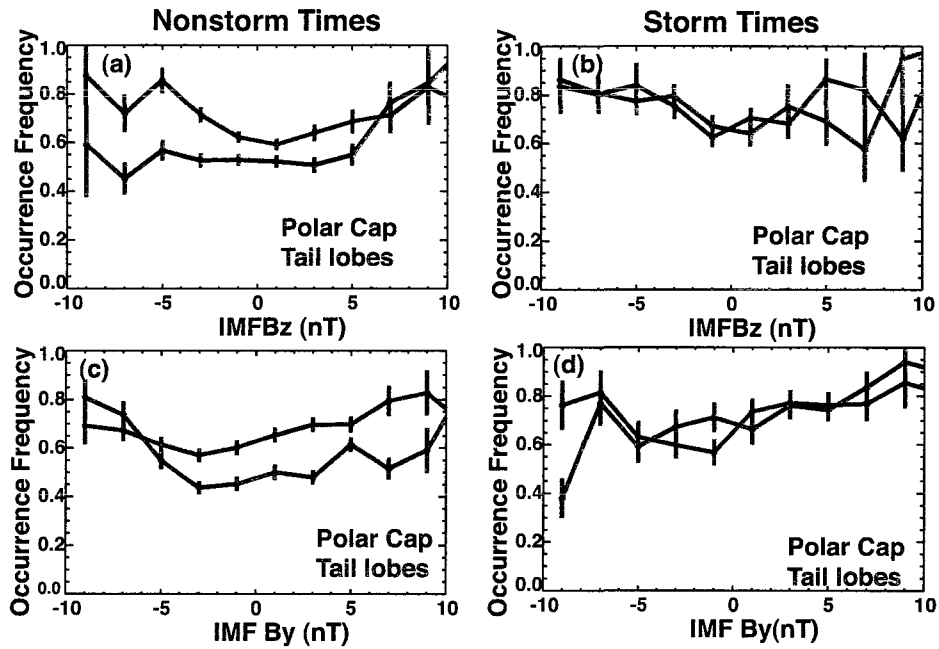
Figure 4-9: Correlations between occurrence frequency and IMF B_y and IMF B_z during nonstorm and storm times.

during storm times and nonstorm times for streaming O^+ in the polar cap and the tail lobes. During nonstorm times, cusp origin O^+ inside the polar cap, shown with the blue line, increases both for stronger negative and positive IMF B_z. The negative IMF B_z effect does not seem very strong for bringing O^+ into the polar caps and even weaker in the tail lobes. Figure 4-9c shows that during nonstorm times, the occurrence frequency also increases with IMF B_y magnitude, with positive IMF B_y being slightly more effective in the polar cap. As with the other nonstorm times correlations, the occurrence frequency in the tail lobes is generally lower than in the polar cap during nonstorm times.

During storm times, stronger IMF B_z leads to higher occurrence frequencies, with almost identical occurrence in the lobes and the polar cap, as shown in figure 4-9b. It seems that even during storm times it is the magnitude rather than the direction of IMF B_z that brings cusp origin O^+ into the near-Earth tail lobe region more effectively. Again, negative IMF B_z does have a better correlation with the occurrence frequency than positive IMF

B_z. For IMF B_y, as shown in figure 4-9d, the trend of the correlation is similar to that during nonstorm times except, as with other trends, the correlation relation for streaming O^+ inside polar cap, the blue line, and tail lobe, the green line, are almost identical, which indicate a more effective transport of O^+ from polar cap into near-Earth tail lobes.
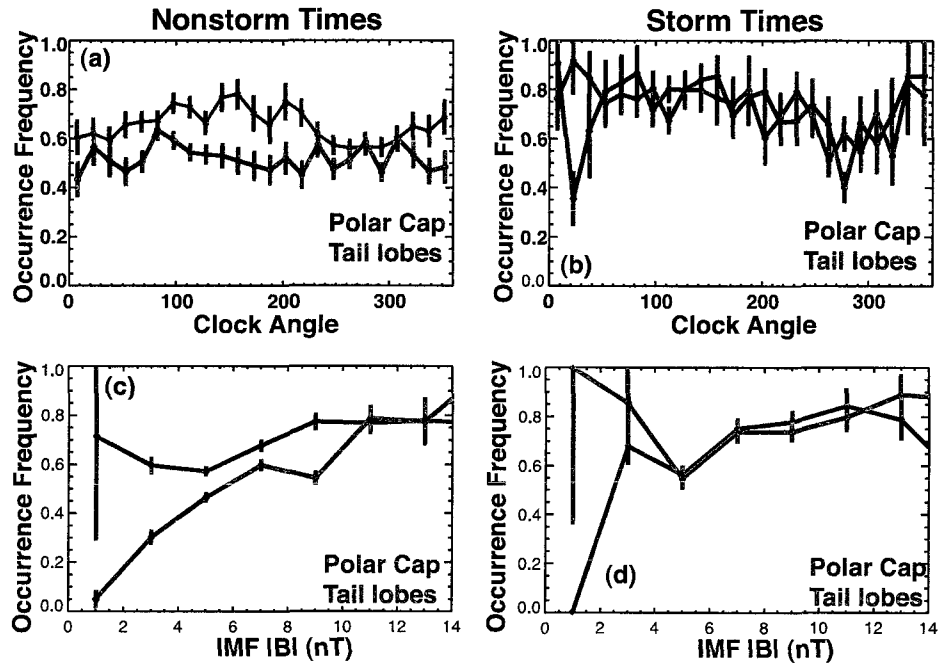
Figure 4-10: Correlations between occurrence frequency and IMF magnitude and IMF clock angle during nonstorm and storm times. Clock angle is defined as $arctan(B_y/B_z)$.

Figure 4-10 shows the correlation between occurrence frequency and IMF clock angle, 4-10a-b, and IMF B magnitude, 4-10c-d. Clock angle is calculated as $arctan(B_y/B_z)$. In this set of plots, it is clear that the direction of IMF is not a strong driver of streaming O^+ in both regions during all times. The only clear trend is a minimum in the occurrence frequency for angles from $\sim$270-340 degree, when IMF B_y is negative and B_z is positive. The IMF B magnitude, in the other hand, seems to be the real driver. During all times in all regions, the occurrence frequency shows a very clear correlation with B magnitude. The trend is especially strong for the occurrence frequency inside the tail lobes during nonstorm

times. The correlation is stronger for tail lobes than for the polar cap.

As stated before, during storms the occurrence frequency dependence for the tail lobes is essentially identical to the one for the polar cap. It seems that all O^+ observed over the polar cap enters the near-Earth tail lobes so that the O^+ occurrence frequency depends on the outflow condition. During nonstorm times, the occurrence frequency for streaming O^+ in the tail lobes is mostly lower than in polar cap especially when IMF B magnitude is low, which indicates that not all the streaming O^+ observed over the polar cap is transported into the near-Earth lobes. They likely move further tailward, and may be lost in the distant tail. The green line in figure 4-10c-d illustrates that the IMF B magnitude is the main driver for the transport path of cusp origin O^+.
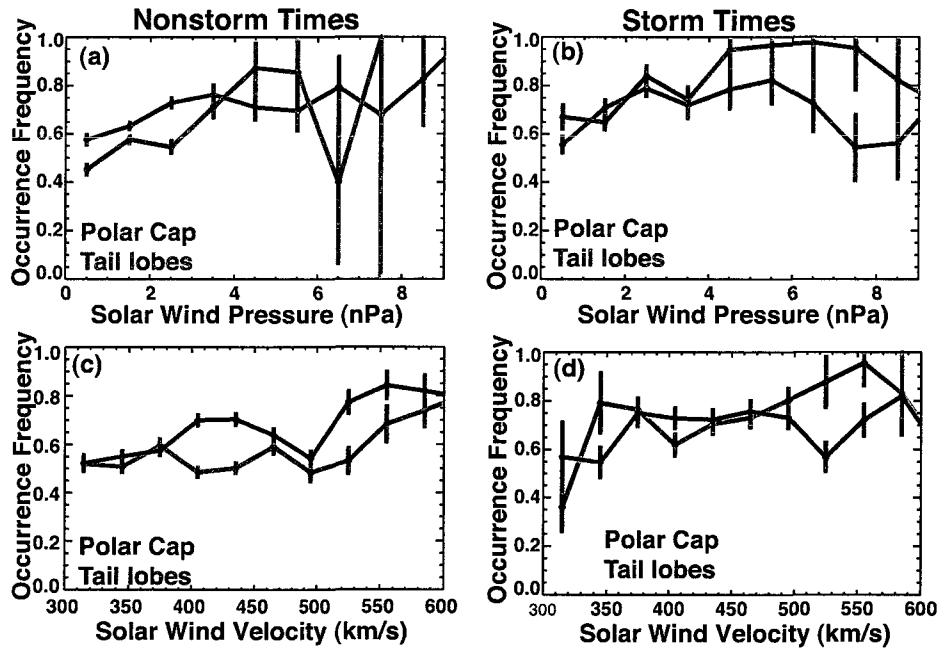
Figure 4-11: Correlations between occurrence frequency and solar wind speed and solar wind pressure during nonstorm and storm times.

Figure 4-11 shows plots of the occurrence frequency versus solar wind pressure and velocity. Solar wind pressure has been found to be a driver for ionospheric outflows [15][53],

so it is not surprising to see that the occurrence frequency of streaming O^+ inside the polar cap increases with higher solar wind pressure in almost all cases. There is a negative correlation with pressure for P > 5 nPa during storm times in the polar cap. This may be because the transport path has been shifted so severely that it moved away from Cluster observation locations. The occurrence frequency of streaming O^+ inside the tail lobes also has a positive correlation with solar wind pressure when it is less than 5 nPa, which may be due to the combination of the increase of the outflows and the compression on the transport path for O^+ at different energies. This may also explain why when it becomes more than 5 nPa, the occurrence frequency during storm times is almost all at 100% in the tail lobes, which is even higher than in the polar cap. There is no noticeable correlation between occurrence frequency and solar wind speed except a positive correlation that can be observed in the polar cap during nonstorm times when velocity is lower than 450 km/s.

4.4 IMF Clock-angle Driving Effect on Asymmetry Transport

In the previous sections, we showed that O^+ from the dayside cusp is not transported symmetrically into the lobe. One possible cause for the asymmetry is the IMF direction because it controls the direction of the newly reconnected geomagnetic field lines on the dayside. In order to determine the external driver for the asymmetry of the O^+ transport path, we calculated the average value of the IMF over the previous 1-hour time period using ACE data that has been propagated to the subsolar point. We then subdivide our data by IMF orientation and magnitude. Figure 4-12 shows the YZ_{GSM} occurrence frequency maps for nonstorm times under different IMF clock-angle ranges. The top two panels show the distributions for positive B_z with negative and positive B_y, and the bottom two panels show the distributions for negative B_z with negative and positive B_y. Maps for positive IMF B_y (Figure 4-12b and 4-12d) are very similar and both of them have a strong south/dusk – north/dawn asymmetry. Maps for negative IMF B_y (Figure 4-12a and 4-12c) show no
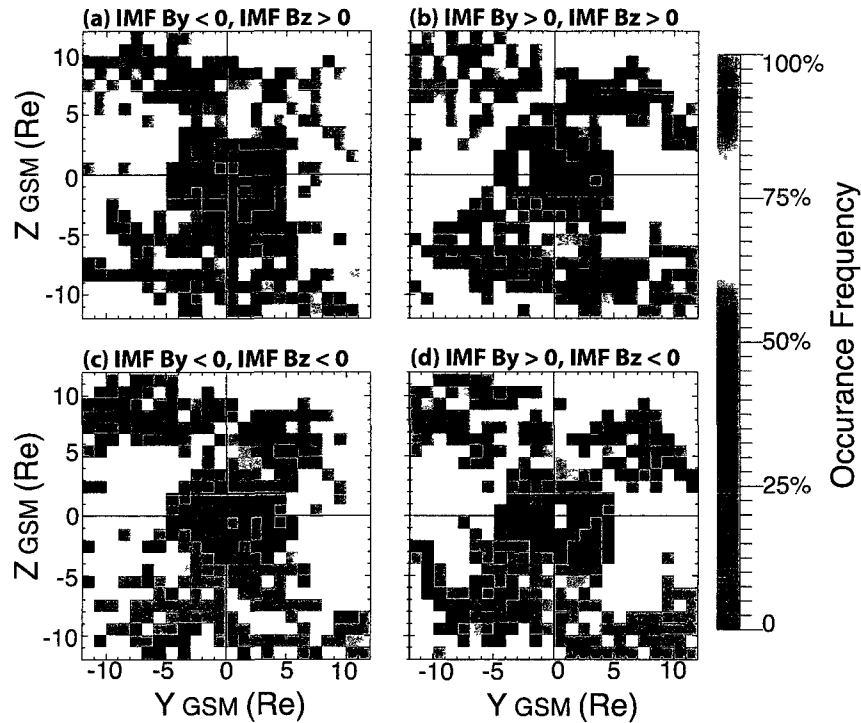
Figure 4-12: Nonstorm times occurrence frequency maps of streaming O^+ sorted by the direction of IMF B_y and IMF B_z. Maps are in the YZ_{GSM} plane and integrated over all X_{GSM}. Bins in white have no sample while dark blue means zero occurrence frequency.

strong asymmetry, although the map for negative IMF B_z (Figure 4-12c) has an overall higher occurrence frequency than the map for positive IMF B_z (Figure 4-12a). In summary, positive IMF B_y causes O^+ to move towards the south/dusk – north/dawn quadrants, while the O^+ transport is more symmetric under negative IMF B_y. IMF B_z does not have an effect on the asymmetry of the O^+ transport.

To investigate further, we examined the influence of the magnitude of IMF B_y on the asymmetry. Figure 4-13 compares the distributions for positive and negative B_y with the distributions when the IMF B_y is less than -3 nT and greater than 3 nT. The map for IMF B_y greater than 3 (Figure 4-13d) has a clear asymmetry, similar to the map for positive IMF B_y (Figure 4-13b). For the case when IMF B_y is more negative than -3 (Figure 4-13c), a reversed asymmetry from Figure 4-13d, is now observed in the northern hemisphere,
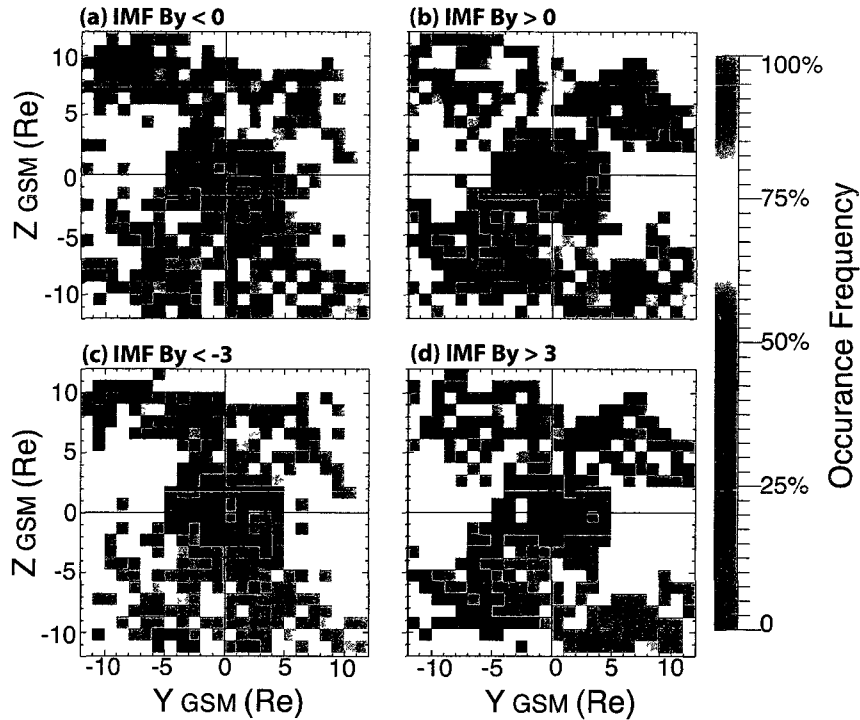
Figure 4-13: Nonstorm times occurrence frequency maps of steaming O^+ sorted by IMF B_y direction and magnitude. Maps are in the YZ_{GSM} plane and integrated over all X_{GSM}. Bins in white have no sample while dark blue means zero occurrence frequency.

that is not observed in Figure 4-13a, the map for IMF B_y less than 0. The north/dusk asymmetry in the occurrence map for IMF B_y less than -3 confirms that the IMF B_y direction does control the O^+ transport from the dayside cusp, but there seems to be an overall south/dusk – north/dawn asymmetry independent of B_y and then the B_y effect acts on top of this, enhancing it for positive B_y and reducing it for negative B_y.

4.4.1 Effect of IMF B_y on Transport

The transport path of the cusp O^+ outflow has a spatial asymmetry that is associated with the IMF B_y component. When IMF B_y is positive, the outflow from the northern hemisphere tends to move towards the dawnside, while outflow from the south travels towards the duskside of the magnetosphere. The sense of this asymmetry becomes stronger when the magnitude of IMF B_y increases. The asymmetry disappears under weak negative

IMF B_y, and reverses, at least in the north, under strong negative IMF B_y, although overall, positive IMF B_y still leads to a much stronger asymmetry than negative B_y. Similar IMF B_y-related asymmetries have been observed for different species and in different magnetosphere regions. Hardy et al. [30] found a similar IMF B_y related asymmetry for the occurrence probability of lobe ions at 10 to 3500 eV/q, instead of streaming O^+, using the Total Ion Detector (TID) of the Suprathermal Ion Detector Experiments (SIDE) stationed on the lunar surface. He speculated that the asymmetry was due to a high cross-tail electric field in those sections of the tail, enabling the lobe plasma to drift a greater distance into the tail thus increasing the time during which it is seen. Gosling et al. [25] reported an asymmetry controlled by IMF B_y component in the same sense for lobe plasma densities near the distant current sheet over the radial range -118 R_E to -220 R_E. Since electron density was measured here rather than occurrence probability, the IMF B_y related asymmetry in the plasma density cannot be explained by the longer drift paths in the preferential quadrants. Gosling interpreted the phenomenon to be solar wind particles entering preferentially on the more locally "open" sides of the geomagnetic tail. Seki et al. [68] reported that O^+ observed at high energy ($\sim$3.4 keV on average), in the distant tail (geocentric distance from 8 to 210 R_E) with Geotail has an IMF B_y related asymmetry in occurrence frequency. This result and our observations are consistent in the sense of asymmetry and they are consistent with the expected outcome of the velocity filter effect, in that the more energetic O^+ would go further down the tail. The asymmetry of the solar wind plasma distribution inside the magnetosphere at both near Earth regions and distant tail indicates that there is an IMF B_y controlled asymmetry in the same sense as the distribution of the open field lines. Cowley [13] discussed this effect more quantitatively and showed how the plasma entry is connected with the field normal to the tail magnetopause.

One cause of the asymmetric plasma transport is the connection with the IMF, through reconnection that happens at the dayside. Newly reconnected open field lines are dragged tailward by the IMF, and the B_y component of the IMF drags the tail field either duskward or dawnward. Figure 4-14 shows the Tsyganenko T04s [72] model results of the magnetic

field configurations under different IMF clock-angles but the same strength (10 nT). Plots are shown in 3-D, but in the view of looking from the Sun to the Earth, the same direction as all occurrence frequency maps in the YZ_{GSM} plane. The vector lines are the open field lines with foot points on the Earth and the other ends extending outward and tailward. When IMF B_y is positive, as in figure 4-14b and figure 4-14d, all open field lines in the north magnetosphere turn towards the dawnside as they extend to the tail lobe region as if they are dragged by the end that is connected to the IMF while the open field lines in the south are dragged in the opposite direction. When B_y is negative, the force associated with the field line tension changes to the opposite direction in both hemispheres so, as shown in figure 4-14a and figure 4-14c, the field lines tend to move to the sides opposite to the one for positive IMF B_y. The color in the plots represent the strength and direction of the Y component of the magnetic field inside the magnetosphere at the cross section of X_{GSM} = -15 R_E. The red/yellow region means the field is duskward, blue means dawnward and green represents a very small B_y component. For positive IMF B_y, shown in both Figure 4-14b and Figure 4-14d, the magnetic field lines in the tail lobe show strong asymmetry in the strength of the magnetic field B_y, implying that there are more open field lines in the quadrants of north-dawn and south-dusk due to the drag from the IMF. This effect leads to the magnetic field strength asymmetry in the normal direction along the boundaries of the magnetotail and produces the asymmetry of the plasma entry found by Gosling et al. [25]. It is also consistent with the observation that the Y component of the internal magnetic field inside the magnetosphere tends to have the same sign as IMF B_y [22]. The low-altitude signature of the shift of geomagnetic field lines is the azimuthal flow of the newly opened field lines in the dayside cusp region, which moves predominantly westward for IMF B_y positive and eastward for IMF B_y negative in the northern hemisphere, leading to the Svalgaard-Mansurov effect [13].

Because of the drag of the IMF on the magnetic field, there are two additional effects that influence the plasma transport as well. One effect is that the boundary between open and closed field lines displaces depending on IMF B_y and is different in the north and south

hemisphere [33][14], in the same sense of asymmetry as we observed for streaming O^+ in the lobe. This effect will cause the source of the ionospheric ions on the open field lines to have an asymmetry from the start and will influence the transport pattern of O^+ when they have not traveled too far down the tail. The other effect is that due to the pull of the IMF on the open field lines and the torque they exert on the close field lines, the magnetospheric field lines are twisted in the tail and the current sheet is tilted, with the direction of the tilt depending on IMF B_y. As a result, all the plasma flowing along the field lines will tilt as well, causing an asymmetry in the plasma flow and density. Villante [73] found that at -1000 R_E (Pioneer 7), the tilt of the very distant current sheet is less than 20 degrees most of the time. Within the region of the CLUSTER orbit, less than 20 R_E in the tail, the tilt of the current sheet should be very small and not a major contribution to the asymmetry we observed in the O^+ transport path. On the other hand, the effect will have a stronger influence on the observation far away from the Earth such as the Geotail observation from Seki et al. [68] and ISEE result from Gosling et al. [25].

Statistical studies with CLUSTER EDI data show that the sign of the convection velocity Y component is the same as IMF B_y in the north lobe and opposite in the south [27][57]. The result can be explained as $\mathbf{V_y} = \mathbf{E_z} \times \mathbf{B_x} = (\mathbf{V_x} \times \mathbf{B_y}) \times \mathbf{B_x} = \mathbf{B_y}(B_x V_x)$. This convection velocity brings the plasma from the outer open field further toward the center of the plasmasheet. This convection velocity in the lobe was also shown by Cowley [13] to result from the IMF B_y effect. A similar asymmetry in the electric field strength was also mentioned by Cowley [13] and explained with $\mathbf{E} = \mathbf{V_x} \times \mathbf{B_n}$, but a study by Noda et al.[57] does not seem to support this idea. More investigation is still needed to make clear whether there is an asymmetry in the strength of the convection field. It will also help determine whether there will be an asymmetry in the velocity filter effect that affects O^+ transport in different quadrants under different IMF B_y conditions.

4.4.2 Influence of IMF B_z on the asymmetry

Our data show that the asymmetry is not dependent on the sign of IMF B_z. For both positive and negative IMF B_y, there is no obvious difference between positive and negative IMF B_z in the spatial distribution of the occurrence frequency, although there is some effect on the overall magnitude of the occurrence frequency. This result is consistent with the model magnetic field results shown in figure 4-14. Although IMF B_z does change the field line configuration to some extent, it does not have a strong influence on the dawn/dusk shift of the magnetic field. The shift direction of the field lines in figure 4-14a for positive IMF B_z and negative IMF B_y is the same as in figure 4-14c when IMF B_z is negative and IMF B_y still points at dawnward. The situation is the same for positive IMF B_y and IMF B_z changing from northward to southward. As is well known, the location of reconnection on the front side changes depending on IMF B_z [45]. However, independent of where the reconnection occurred, if the IMF is southward, the newly reconnected field lines will be dragged by the solar wind and convect towards the nightside. The situation for northward IMF is more complicated, but MHD simulations have shown that for northward IMF reconnection, after connection, the field lines still end up as nightside and tailward open field lines in the lobe [47]. In addition, when the polar cap convection patterns are sorted by IMF clock angle into 45-degree sectors, as done by Haaland et al. [28], the convection patterns for sectors with positive B_y or negative B_y are almost independent of B_z. Only the 45-degree sector centered on north shows a dramatically different pattern. In summary, we can state that the direction of the IMF B_z component does not change the asymmetry patterns, and this is consistent with empirical models of the magnetic field, and with the polar cap convection patterns. Note here that we are talking about the influence of IMF B_z on the spatial distribution of the O^+, not the flux. IMF B_z may well have a significant impact on the flux of O^+, in the polar cap and tail.
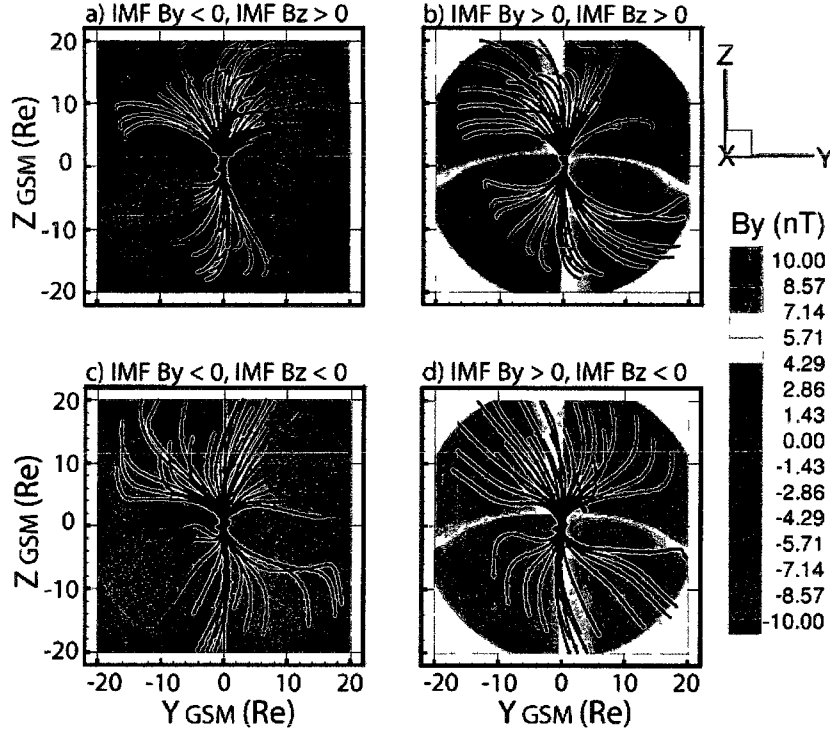
Figure 4-14: Tsyganenko T04s modeling of open magnetic field lines sorted by IMF B_y and IMF B_z directions. Plots are in the YZ_{GSM} plane and are viewed from the Sun to the Earth. Color shows the magnitude of the B_y component of the magnetospheric field lines at $X = -15$ R_E.

4.4.3 Lack of mirror symmetry when B_y is reversed

Although the asymmetric transport path of streaming O^+ is controlled by IMF B_y, it is also clear that the path does not mirror for positive and negative IMF B_y, so there is some other effect besides the effect of the IMF driver. Polar cap convection patterns also show a lack of mirror symmetry when IMF B_y reverses [31][74] [64], [28]. In particular, in the northern hemisphere, for positive IMF B_y, the pattern is very asymmetric, with a westward azimuthal flow over the polar cap, while for negative IMF B_y the pattern is relatively symmetric. This is believed to be due to the day-night conductivity gradient in the polar cap, which has the effect of squeezing the ionospheric flows to the dawnside

in the northern hemisphere, similar to the effect of positive IMF B_y. Hence, for positive IMF B_y, the effect is enhanced, while for negative IMF B_y it is reduced, breaking the mirror symmetry of the IMF Y component effect on the flow transport [2]. Simulations have shown how the day-night conductivity gradient breaks the symmetry for the positive and negative B_y convection patterns [54][71]. This is very similar to what we observe, with a strong asymmetry for positive B_y and only a small asymmetry for negative B_y. However, for the polar cap convection, the pattern is reversed in the southern hemisphere, with a strong asymmetric pattern for negative B_y, and a symmetric pattern for positive B_y. For the O^+ distributions, we observe the strong anisotropy in both the north and the south for positive B_y, and the more symmetric transport for negative B_y. Why this is not consistent with the polar cap results is not clear.

One possibility is that the difference is due to a seasonal effect. From 2001 to 2002, the satellite passes the cusp and polar cap region during all seasons while the apogee only passes the deep tail from July to October. During the tail season, the northern hemisphere is in the summer and fall while the southern hemisphere is in the winter and spring. As a result, our observations in the north tail lobes are streaming O^+ from the summer/fall hemisphere while in the southern lobe we observe O^+ from ionosphere that is in the winter/spring season. Ruohoniemi and Greenwald [64], performed a study how the IMF B_y influence on the convection pattern is affected by the seasons. They found that the seasonal effect tends to reinforce the IMF B_y effect, so that the positive IMF B_y summer (corresponding to our northern observations) and the negative B_y winter (corresponding to our southern observations) have the most asymmetric convection patterns. Thus, the fact that we observe very little asymmetry for negative B_y in the south cannot be explained as a seasonal effect.

Weimer [75] has mentioned a similar break of IMF B_y influence on his map for field line current and he suggested IMF B_x as the cause. Further study is needed to clarify if there is an IMF B_x effect.

4.4.4 Effects of sampling biases

Some bias may be introduced because O^+ from 10 eV to 40 eV that may exist in the polar cap and lobe region are missed in this data analysis. Based on the velocity filter effect from Horwitz [34], the lack of low energy O^+ may cause an underestimation in occurrence frequency during low-convection times. In our data set, the O^+ observed in the polar cap tends to peak at the lowest energy channel (40 eV) while O^+ in the tail lobe peaks at the 154 eV channel. Thus, there is relatively more low energy O^+ missed in the polar cap than in the tail lobes. We already observe the largest occurrence frequency of streaming O^+ over the polar cap, 64% even during quiet times, so we do not think that missing the lower energies has a large at the effect occurrence frequency result.

4.4.5 Effect of the asymmetric transport on the plasmasheet and flank
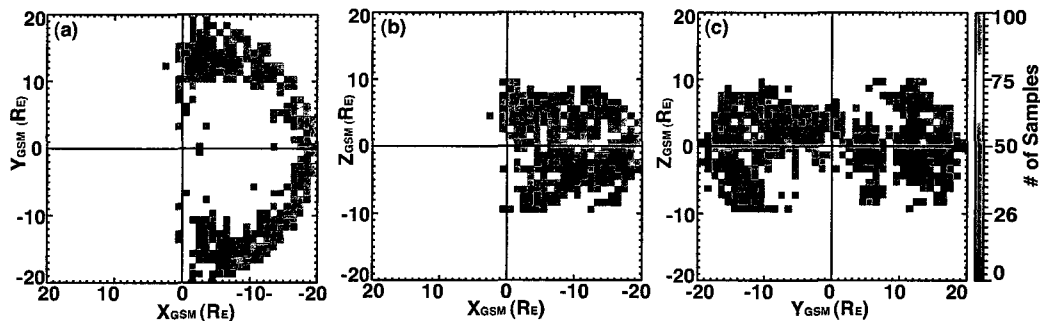
Figure 4-15: Sample maps for all data collected in the plasmasheet during nonstorm times from 2001 to 2002. From (a) to (b), maps are in projection plane XY_{GSM}, XZ_{GSM} and YZ_{GSM}

A long-standing question has been whether O^+ in the plasmasheet affects the dynamics of the plasmasheet by affecting the onset of reconnection, the onset of current disruption, or the reconnection rate. Baker et al. [4] and Baker et al. [3] suggested that a localized region of oxygen-dominated plasma could make the plasma more unstable to the ion tearing mode, and enhance the probability for substorm onset in that region. If the O^+ entered
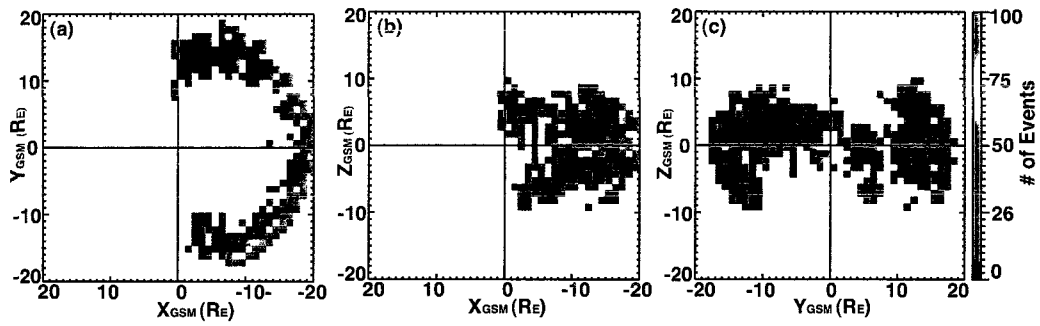
Figure 4-16: Streaming O^+ events maps for all data collected in the plasmasheet during nonstorm times from 2001 to 2002. From (a) to (c), maps are in projection plane XY_{GSM}, XZ_{GSM} and YZ_{GSM}
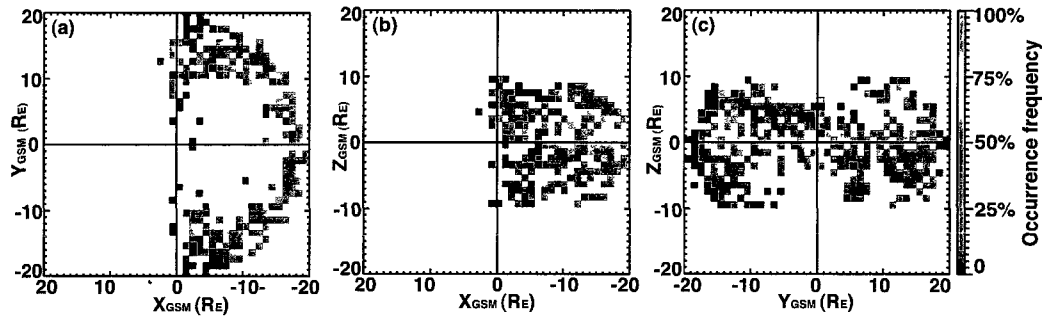
Figure 4-17: Occurrence frequency maps for all data collected in the plasmasheet during nonstorm times from 2001 to 2002. From (a) to (c), maps are in projection plane XY_{GSM}, XZ_{GSM} and YZ_{GSM}

the plasmasheet preferentially on one side or the other, it could effect the likely locations of reconnection onset and the subsequent dynamics.

Figure 4-15 are the maps of total data samples collected inside the plasmasheet during nonstorm times in XY_{GSM}, XZ_{GSM} and YZ_{GSM} projection planes. Those maps show the Cluster coverage of the plasmasheet during nonstorm times from 2001 to 2002. As shown in figure 4-15a, because of the nature of the orbits from 2001 to 2002, the coverage is a shell. It only contains the outer part of the plasmasheet.

Thus, in figure 4-15b, the region inside of $X_{GSM} = 10$ R_E and outside of $Y_{GSM} = 10$ R_E, is close to the magnetopause, known as the flanks. Figure 4-16 and figure 4-17
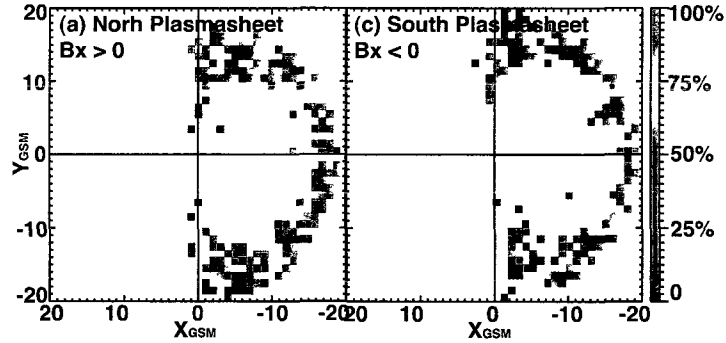
Figure 4-18: Occurrence frequency map of O^+ beams in XY_{GSM} plane during nonstorm times in the north plasmasheet ($B_x > 0$) and south ($B_x < 0$) plasmasheet.

are maps of streaming O^+ events and occurrence frequency of O^+ inside the plasmasheet during nonstorm times in all three projection planes. The events maps look very similar to sample maps, which hints that streaming O^+ is very common. This can be seen directly from the occurrence frequency maps: streaming O^+ was detected over 70% of the time at most locations in the plasmasheet. There is an asymmetry observed for the occurrence frequency of the O^+ beams in the flanks, shown in figure 4-17c. The trend is similar as observed for the O^+ beams inside the tail lobes. The location of the plasmasheet inside the flanks is tilted in this coordinate system, but there is no obvious asymmetry in the beam locations.

Because of the movement of the magnetotail, it may not be accurate to use Z_{GSM} to divide the north and south plasmasheet. Figure 4-18 shows the occurrence frequency maps in XY_{GSM} plane in the north and south plasmasheet. B_x is used here to divide the plasmasheet. It is clear that there is no asymmetry for the streaming O^+ in the plasmasheet at -19 R_E. Some asymmetry can be seen here in the flanks. One possible explanation for the absence of the asymmetry in the plasmasheet is that although we found asymmetry for the transport path of the O^+ from the cusp, the O^+ does reach both sides of the plasmasheet. It just preferentially reaches the dawn from the north and the dusk from the south. Once the O^+ enters the plasma sheet and crosses the neutral sheet, it becomes isotropized [59][42] so that the north/south asymmetric entry may be no longer be apparent in the near-Earth

part of the plasmasheet, but a dawn or dusk preference would remain if there is any. Thus for individual cases, a difference in the amount of O^+ outflow from the north and the south could lead to a dawn-dusk asymmetry in the O^+ in the plasmasheet, which would have the associated consequences. However, if the outflow from the two hemisphere is not equal, this may still result in an O^+ concentration in certain regions. Flux and density need to be taken into account when considering the instability since occurrence frequency itself can only represent how often O^+ beams appear, not how many O^+ ions arrive.

Chapter 5

ACCELERATION

The moments of the streaming O^+ and their distribution functions offer a lot of information about the transport mechanism of ionospheric ions from the cusp, i.e. how those ions are transported across the polar cap, into the lobes, though the PSBL and then convected into the plasma sheet. In this chapter, we will show the maps of the median moments and the changes to the distribution function of the streaming O^+ and discuss the impact of the velocity filter effect in observing and analyzing the acceleration mechanism. As in the last chapter, only data from 2001 to 2002 are used to limit the solar cycle impact. Most of the data used in this chapter is from nonstorm times because the transport and acceleration mechanisms during storms can be quite different from nonstorm times and we do not have the statistical database to perform the same analysis. We will only do some comparison of the nonstorm times data with storm times data in the discussion section.

5.1 Velocity Filter Effect Impact

The cusp outflow is dispersed according to its velocity as it is transported to the tail, due to the velocity filter effect as discussed in introduction. Thus changes in the moment maps may result simply from Cluster orbits flying through regions where O^+ with different velocities passes by, and do not necessarily indicate an acceleration.

To show what we expect from the velocity filter effect, we assume the distribution function in the cusp outflows is an ideal Maxwell-Boltzman 2D distribution as shown in figure 5-1a. Although the real outflow distributions vary for different latitudes and contains mostly upward population, using Maxwell-Boltzman 2D distribution in this case is good
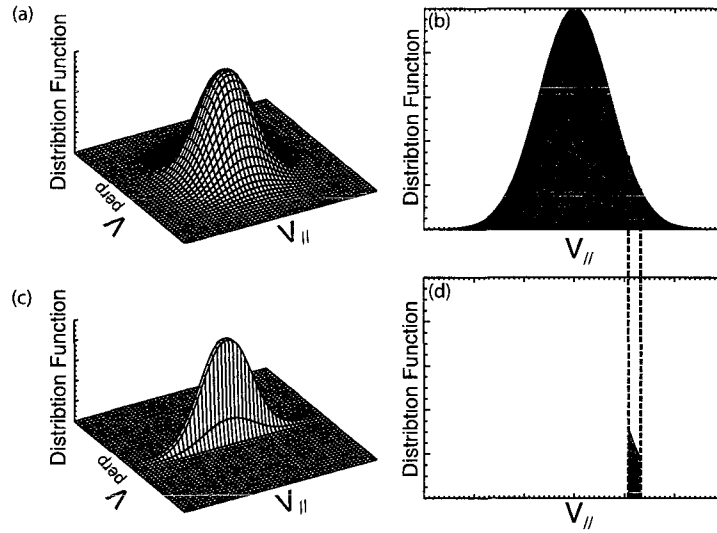
Figure 5-1: Sketches showing the relationship between the initial outflow distribution function and the outflow distribution function in the tail lobes after the velocity filter effect (after [69]). (a) Maxwell-Boltzman 2D distribution; (b) The cut of the initial distribution function in parallel velocity direction; (c) Maxwell-Boltzman 2D distribution in the region where the magnetic field is lower and the plasma has cooled down because of the mirror force; (d) Distribution of streaming O^+ which is part of the full distribution due to the velocity filter effect.

enough for showing our concept of velocity filter effect. The distribution will fold up due to the mirror force as the ions move towards the tail so the distribution function will become like figure 5-1c. Figure 5-1b shows the cut of the initial distribution function in parallel velocity direction and figure 5-1d shows how a particular beam distribution function would look when the velocity filter effect has separated the distribution by the parallel velocity. When the satellite passes through the transport path of O^+ streaming at different velocity, the observations will strongly depend on the orbit. Because the initial distribution is a maxwell-boltzman-like distribution centered at a low energy as will be shown in the later part of the chapter, the density of the streaming O^+ in a higher energy range will be naturally lower compared with slower streaming O^+. Moreover, if the tail lobe ion beam distribution is part of the initial distribution, it means that we are observing just a velocity filter effect. However, if the observed beams exceed the initial distribution, most likely

the O^+ has been accelerated from the lower energy population, whose phase space density is higher. Hence, it will be an indication of the existence of an increased velocity due to additional acceleration or stronger drifts.

5.2 Moment Maps

As described in chapter 3, we calculated the moments of the streaming O^+, and in this section we will present the maps of the median value of moments. We used median value instead of average value here so as to reduce the impact of the long tail to the distribution since the spread of the O^+ beams moments is wide, but most of them have relatively small values as shown in figure 3-13.

Figure 5-2, figure 5-3 and figure 5-4 give the maps of the median density, median bulk kinetic energy, and median temperature during nonstorm times in the XZ_{GSM} plane. Three different rows are for different magnetosphere regions. The panels from top to bottom show for streaming O^+ in the lobes, PSBL and plasma sheet. The three columns are for threes slices in the Y_{GSM} direction and from left to right are at the dawn side, defined as -12 R_E < Y_{GSM} < -4 R_E, the center, defined as -4 R_E < Y_{GSM} < 4 R_E) and the dusk side (4 R_E < Y_{GSM} < 12 R_E). The color shows the median value of the moments of all the streaming O^+ observed at each 1 × 1 R_E grid.

As shown in figure 5-2, the median density of the O^+ beams in the near-Earth magnetosphere varies inside the magnetosphere. The density of O^+ beams in the lobes is generally higher than in the PSBL and in the plasma sheet. It is not surprising since the density here is only the density of the beams rather than the whole plasma population and the low magnetic field inside the latter two regions leads to a larger magnetic flux tube, which will lower the density of the O^+ beams in the end. Another strong feature is the gradual decrease of lobe O^+ density from near the cusp source region, up to 0.1 cm^{-3}, to the tail lobes around 0.005 cm^{-3}, as shown in figure 5-2b. As stated before, this density decrease in the tail can be explained with the velocity filter effect which cause the satellite detect slower and denser O^+ close to the Earth and faster and less dense O^+ in the tail. Another
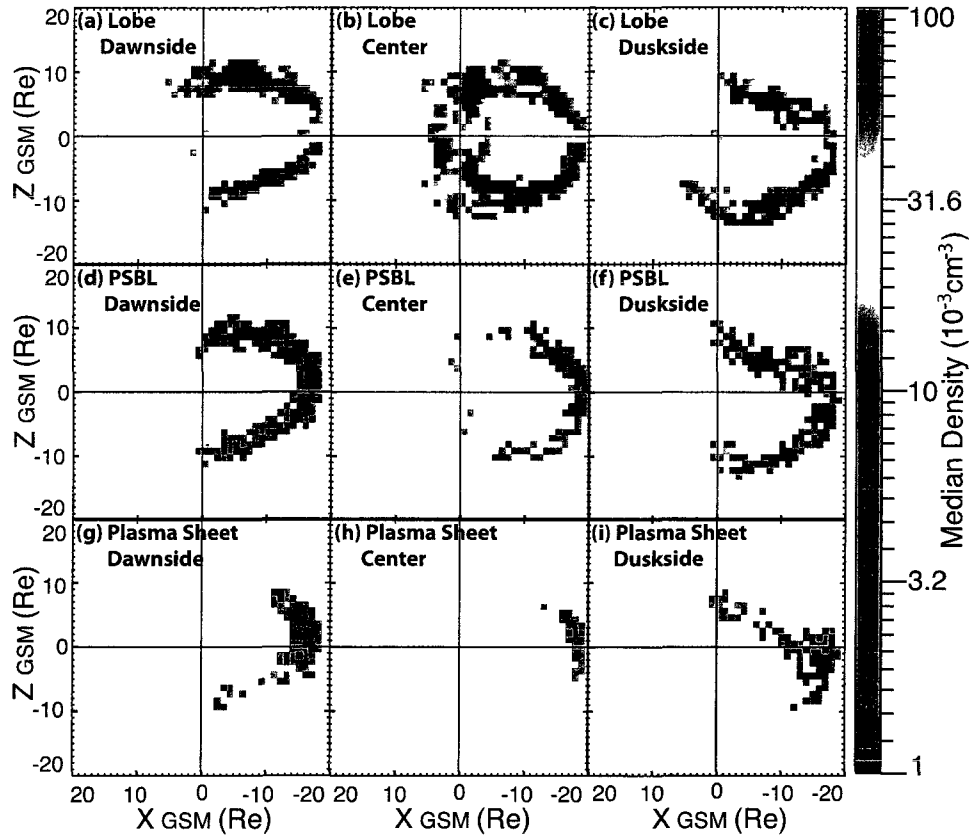
Figure 5-2: Maps of the median density of streaming O^+ during nonstorm times in XZ_{GSM} plane. Three rows are for different magnetosphere regions (top to bottom): lobes, PSBL and plasma sheet. Three columns are for three slices in the Y_{GSM} direction (left to right): the dawn side (-12 R_E < Y_{GSM} < -4 R_E), the center (-4 R_E < Y_{GSM} < 4 R_E) and the dusk side (4 R_E < Y_{GSM} < 12 R_E).

contribution, similar to the reason for the low density O^+ beams observed in the PSBL and the plasmasheet, is the increased flux tube volume in the tail due to the low magnetic field strength compared with polar cap region, which then further dilutes the O^+ beams in the tail. The density does not seem to have any dependence on Y_{GSM}.

Bulk kinetic energy mapped here is the median value of the kinetic energies of all the streaming O^+. However, in the lobes because most O^+ beams observed are cold and mostly parallel to the magnetic field, the bulk kinetic energy mapped here are mainly from the parallel velocity and is the major contribution of the total energy of the streaming O^+.
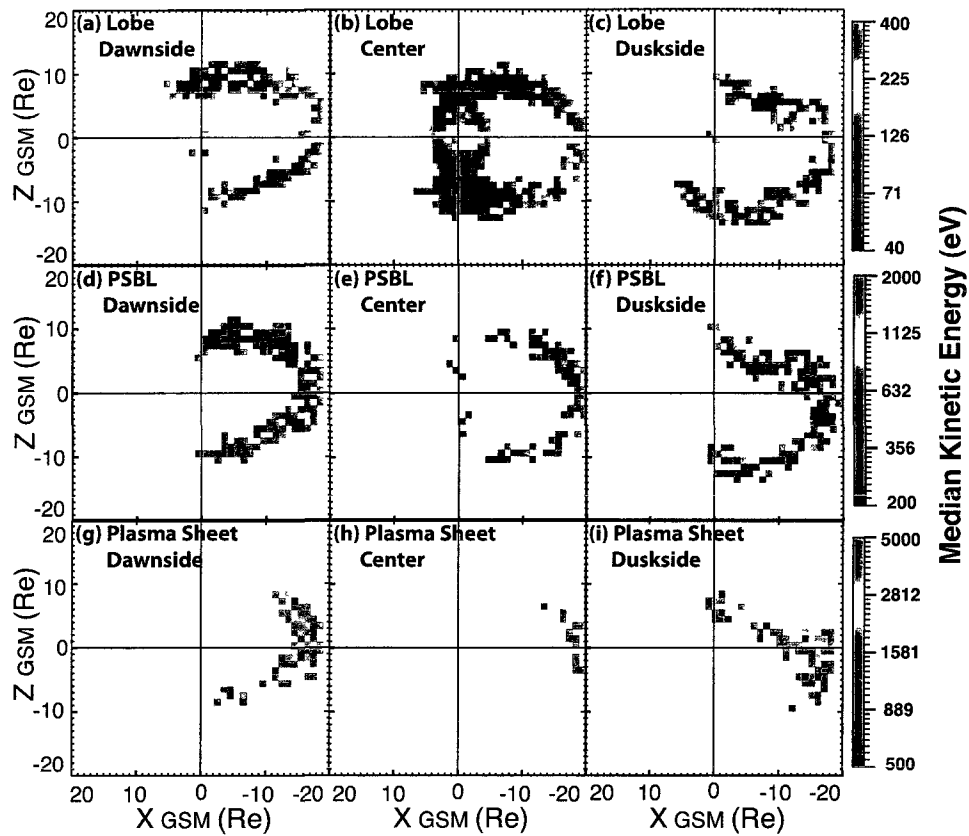
Figure 5-3: Maps of the median velocity of streaming O^+ during nonstorm times in XZ_{GSM} plane. Plot arrangement is the same as figure 5-1.

The contribution of the perpendicular velocity becomes stronger in the PSBL and the plasmasheet. As expected, O^+ streaming velocities are slowest inside the lobes, get faster in the PSBL and are fastest inside the plasma sheet. Multiple accelerating mechanisms have been proposed and studied for O^+ entering the plasma sheet through the PSBL as mentioned in the introduction chapter.

The bulk kinetic energy map for streaming O^+ inside the lobes at the center of Y_{GSM}, figure 5-3b, shows that there is a clear gradual increase from the cusp/cleft regions to the tail, from 40 eV to about 400 eV. Both the velocity filter effect and acceleration may lead to this result and they may actually both have an effect. A particle tracing simulation may be done to find out which one is the dominant effect. Streaming O^+ transported to larger
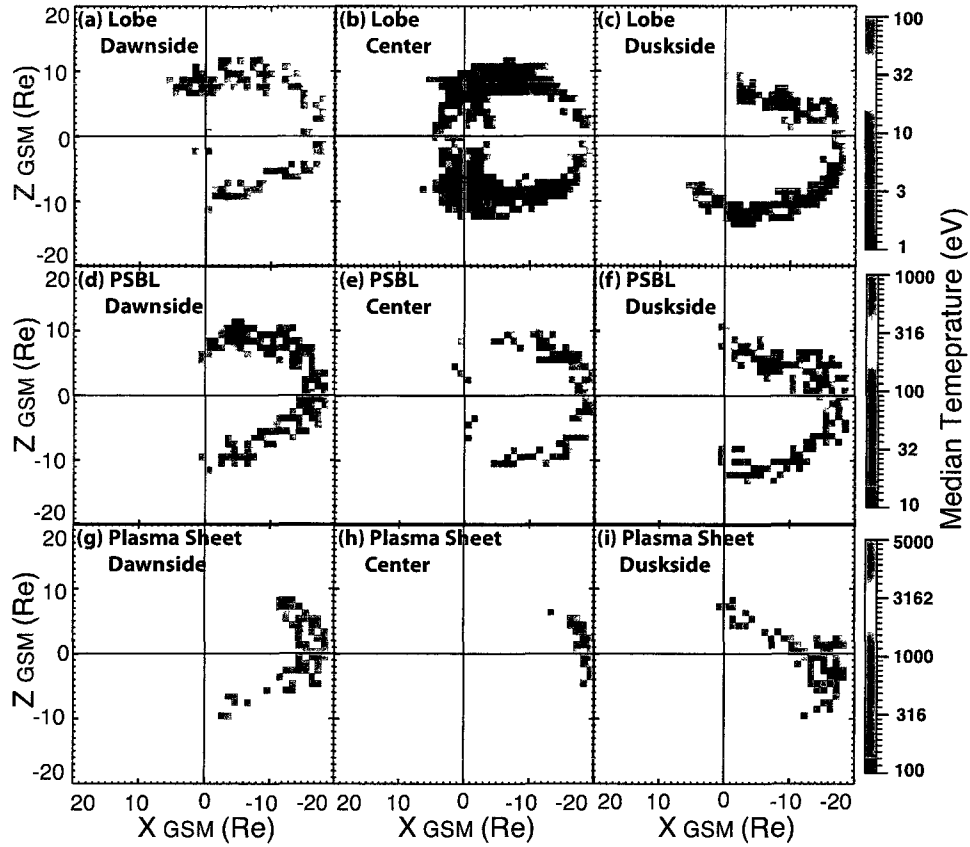
Figure 5-4: Maps of the median temperature of streaming O^+ during nonstorm times in XZ_{GSM} plane. Plot arrangement is the same as figure 5-1.

Y_{GSM}, as shown in dawn side and dusk side maps, are faster than those at small Y_{GSM}, shown in the center maps.

The median temperature maps in figure 5-4, have very similar features as bulk kinetic energy maps in figure 5-3, which is consistent with the fact that observed streaming O^+ inside the magnetosphere have a similar distribution. Streaming O^+ are the hottest in the plasma sheet, less hot in the PSBL and cold in the lobes, which may due to the combination of the additional acceleration on the O^+ entering in the PSBL and the plasmasheet and the velocity filter effect. As in the bulk kinetic energy maps, the temperature gets hotter and hotter from the cusp region to the tail lobes. Streaming O^+ at the dawnside and duskside are hotter than those travels in the center Y_{GSM}.

5.3 Case Study and Method

In order to differentiate between the velocity filter effect and acceleration, in this chapter, we will hypothesize that only the velocity filter effect but no acceleration exists and compare the ideal situation with the observational result to determine whether acceleration is required to explain the observed O^+ with high energy in the tail lobes at $\sim$ -20 R_E.
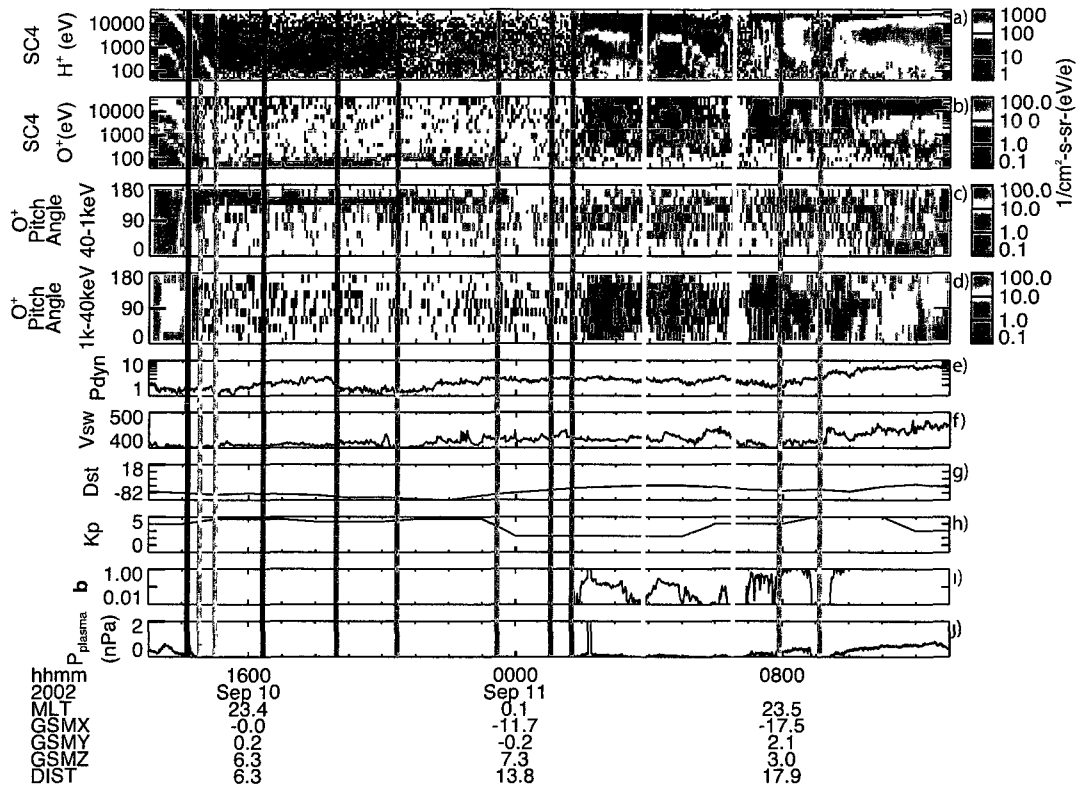
Figure 5-5: One day plot of CIS/CODIF Cluster data and external conditions. Vertical lines show the time of the cusp pass (in black) and times for typical O^+ beams observed in polar cap and tail lobes (in colors). Panels from top to bottom: H+ and O^+ energy spectra, O^+ pitch angle spectra within energy range between 40 eV – 1 keV and 1 keV – 40 keV, solar wind pressure and velocity, Dst and Kp indexes, plasma beta and plasma pressure.

Figure 5-5 and figure 5-6 show an example of a case study in which we test for acceleration. We took one day when the Cluster orbit passed through the cusp and then observed O^+ beams at different locations in the lobe before it arrived in the plasma sheet and com-
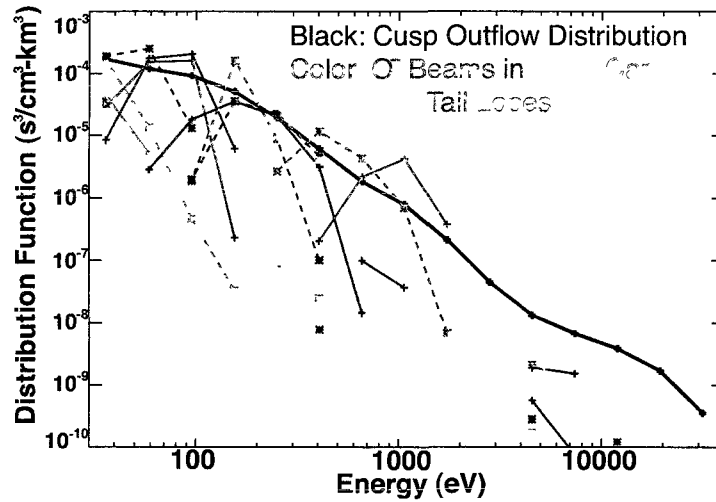
Figure 5-6: Distribution function VS energy plot for O^+ outflow at cusp and O^+ beams in polar cap and tail lobes, normalized to 1000 km. Colors correspond to the lines in figure 5-5

pared the initial cusp distribution with the distributions of typical O^+ beams observed along the orbit. Figure 5-5 shows the spectra and external conditions from 1300UT September 10 2002 to 1300UT September 11 2002. From top to bottom, the panels show the H^+ and O^+ energy spectra, O^+ pitch angle distribution at low (40 eV – 1 keV) and high (1 keV – 40 keV) energies, solar wind pressure, solar wind velocity, Dst index, Kp index, plasma beta and total plasma pressure. The black vertical line in figure 5-5 shows the identified cusp outflows. To identify the cusp, we observed the O^+ energy spectrum near the cusp region, after it comes out from the radiation belt, and chose the time when the distribution of O^+ is the highest at all energy ranges. The colorful lines in figure 5-5 show the times when typical O^+ beams were observed in the polar cap and tail lobes. As mentioned before and can be seen in figure 5-5a and figure 5-5c, the streaming O^+ has a very narrow energy range and are transported mostly along the magnetic field line, i.e. pitch angle is close to 0 or 180 degree. Figure 5-6 compares the normalized distribution function of cusp outflows, in black, with the normalized distribution functions of the lobe O^+ beams, whose colors corresponds to the vertical lines in figure 5-5. In order to compare distribution functions

at different locations in the magnetosphere where the distribution function correlates with the local volume of the magnetic flux tube, we normalized the distribution function with

$$f_{normalized} = f_{observed} \frac{B_{1000km}}{B_{observed}} \tag{5.1}$$

where $f_{normalized}$ is the normalized distribution function, $f_{observed}$ is the observed distribution function, B_{1000km} is the magnetic field at latitude of 1000 km calculated with the dipole field, $B_{observed}$ is the observed magnetic field. As shown in figure 5-6, all of the normalized distribution functions of the O^+ beams have a typical beam like distribution with peaks at different energies. They generally follow the initial distribution function from the cusp outflow, with a slightly higher flux at some energy ranges. The peak energy of the O^+ beams increases from polar cap to lobes while the distribution function decreases, which is the same trend as the cusp outflow distribution, i.e. the distribution function is lower for higher energies. In general, the peak beam distribution function follows the outline from the cusp distribution. Because this example is during storm time, with changing drivers for the outflow and changing convection field, it is not surprising that there is not exact agreement between the outflow and the beams. While it is hard to find a case that has streaming O^+ observed all the way from the cusp to the -19 R_E tail lobe during quiet times, the storm times case usually has dramatically changing conditions, so it is impossible to give a solid statement with only case studies. Without simultaneous outflow and beam observations, a statistical study is required to test whether the beams show clear evidence of acceleration or not.

5.4 Statistical Study

In this section, we will statistically compare the initial distribution from the cusp outflows with the distribution function of the streaming O^+. All distribution functions used were normalized with the method described in the last section. We will use the list of Cluster cusp passes from [6] for our initial cusp distribution, and all streaming O^+ identified automatically with Cluster/CODIF data from Mar 2001 to Dec 2002 (solar maximum) for the

beam distributions. The details of the cusp definition can be seen in [6], where he used the sudden increase of the O^+ mean energy and temperature as the equatorward boundary of the cusp and the time when all the first and secondary moments start to drop precipitously as the poleward boundary. The definition describes the property of cusp as a intense heating region for O^+ with narrow range in latitude and the fact that O^+ cools down as it leaves the heating region. Data are categorized into storm and nonstorm times using the Dst Index, and into different regions, polar cap, tail lobes, PSBL and plasma sheet. Table 5.1 shows the number of cusp passes and number of streaming O^+ events observed in the different regions. There are significantly more streaming O^+ events during nonstorm periods than storm time. The polar cap and tail lobes are both limited to where beta is less than 0.02 rather than 0.05 in this part of the study so they will represent the feature of the lobe more clearly. Similarly, the definition of PSBL is restricted to $0.05 < \beta < 0.5$ in order to avoid the region close the hot plasma in the plasmasheet. Data within region where the condition is not typical were not used in the part of study.

	Cusp	Polar Cap	Tail Lobes	PSBL
Nonstorm	139	11672	4960	2306
Storm	40	2626	2533	1517

Table 5.1: Number of cusp passes and number of streaming O^+ events at different regions during nonstorm and storm time. Polar cap is defined as $\beta < 0.02$ and $X_{GSM} > $ -5 R_E, tail lobes are defined as $\beta < 0.02$ and $X_{GSM} < $ -5 R_E and PSBL is defied as $0.05 < \beta < 0.5$.

One caveat that must be taken into account is that weakly heated O^+ ions exit the heating region at a lower altitude than where Cluster passes the cusp. Figure 5-7a is a sketch showing how Cluster passes the cusp heating region without observing the low energy ions that have been convected away from the cusp at lower latitudes (cite from figure 1 in [7]). Cluster spacecraft are shown as the black lines and point. Red arrows from left to right show the routes of the O^+ with velocity from fast to slow. The red arrow on the very right represents the route of the velocity that is so low that the O^+ moves out from the

heating region before it reaches the latitude of Cluster's orbit. As a result, Cluster misses a major component of the cusp outflow populations at low energy range when it is over the cusp but it may still encounter these lower energy ions over the polar cap or further down the tail.
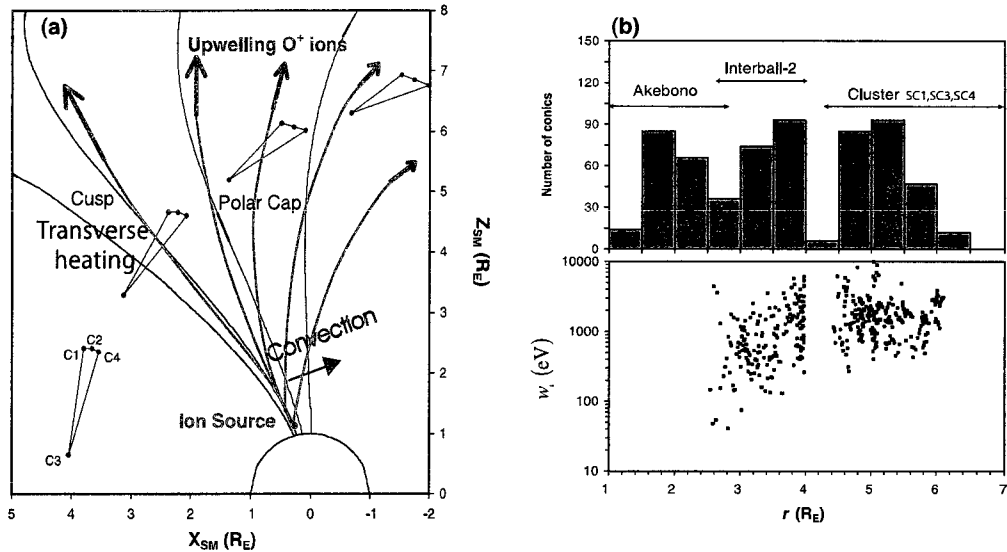
Figure 5-7: (a) Drawing of the Cluster orbit conguration in the dayside auroral and polar regions between July and November 2001 [6]. (b) Top panel is number of ion conical distributions per altitude range and the bottom panel is the mean energy in eV [7]. Copyright [2004] belongs to the European Geosciences Union. Figures are reproduced/modified by permission of the European Geosciences Union.

Figure 5-7b shows the mean energy of O^+ observed by different satellites (cite from figure 4 in [6]). As shown, the mean energy of O^+ observed by Cluster in the cusp is mainly above 500eV. Ions with lower energy are convected out of the cusp below the Cluster orbit. Therefore, the comparison of Cluster cusp outflow observations with the O^+ beams can only be done above 500eV. As in the previous chapters, we divide the whole lobe region into polar cap, X_{GSM} greater than -5 R_E, and tail lobes, X_{GSM} less than -5 R_E. In this way, we can compare the distributions of O^+ beams from the cusp, into the polar cap and into the tail lobes to study the acceleration from cusp to polar cap to the tail lobes.

81

Figure 5-8 shows a comparison of the normalized distribution function of cusp outflows for all passes, in orange, with the normalized distribution function at the peak energy of each O^+ beam. The median of the cusp outflow is shown in red. Nonstorm times are shown on the left, and storm times are on the right. The polar cap distributions are in figure 5-8a-b, the tail lobes, figure 5-8c-d, and the PSBL, figure 5-8e-f. As stated before, the cusp outflow distribution at low energies does not represent the full cusp outflow, so the comparison between the distribution function of the cusp outflow and the O^+ beams is only valid for O^+ with energies higher than 500 eV. For streaming O^+ in the polar cap, figure 5-8a-b, when the energy is higher than 500eV, the features during nonstorm and storm times are similar: the distribution function of the beams in the polar cap cover about the same range as the cusp outflow, and the median values are very close Hence, there is little or no acceleration from the cusp to the polar cap. This may be because of the short distance from the cusp region to the polar cap or it may be there may be that no acceleration exists. This result is consistent with the statement that the centrifugal acceleration impact is very small for ions near the Earth since the accelerating time is too short and the acceleration is a relatively small number [55].

Similarly, during nonstorm times, streaming O^+ with energies higher than 500eV in the tail lobes, as shown in figure 5-8c, cover the same range as the cusp values, while the median values are also very close. This implies that even when O^+ has traveled from the cusp all the way to $19R_E$ down the tail, there is still little or no acceleration.

The story changes during storm times, as shown in figure 5-8d. More than half of the O^+ beams above 500eV exceed the distribution envelope of cusp outflows, which indicates a clear acceleration. However, there were no O^+ beams with energies higher than 3keV observed during storm times. This may be due to the poorer statistics for the storm-time data set. It also supports the statement by Nilsson et al. [55] saying that centrifugal acceleration is weaker for higher energy O^+ because they have a shorter time of flight. Another possibility is that because the typical beta in lobes becomes greater than the $\beta < 0.02$ cutoff during storm time, more energetic streaming O+ may be left out, which may

manually introduce this observed energy cutoff.
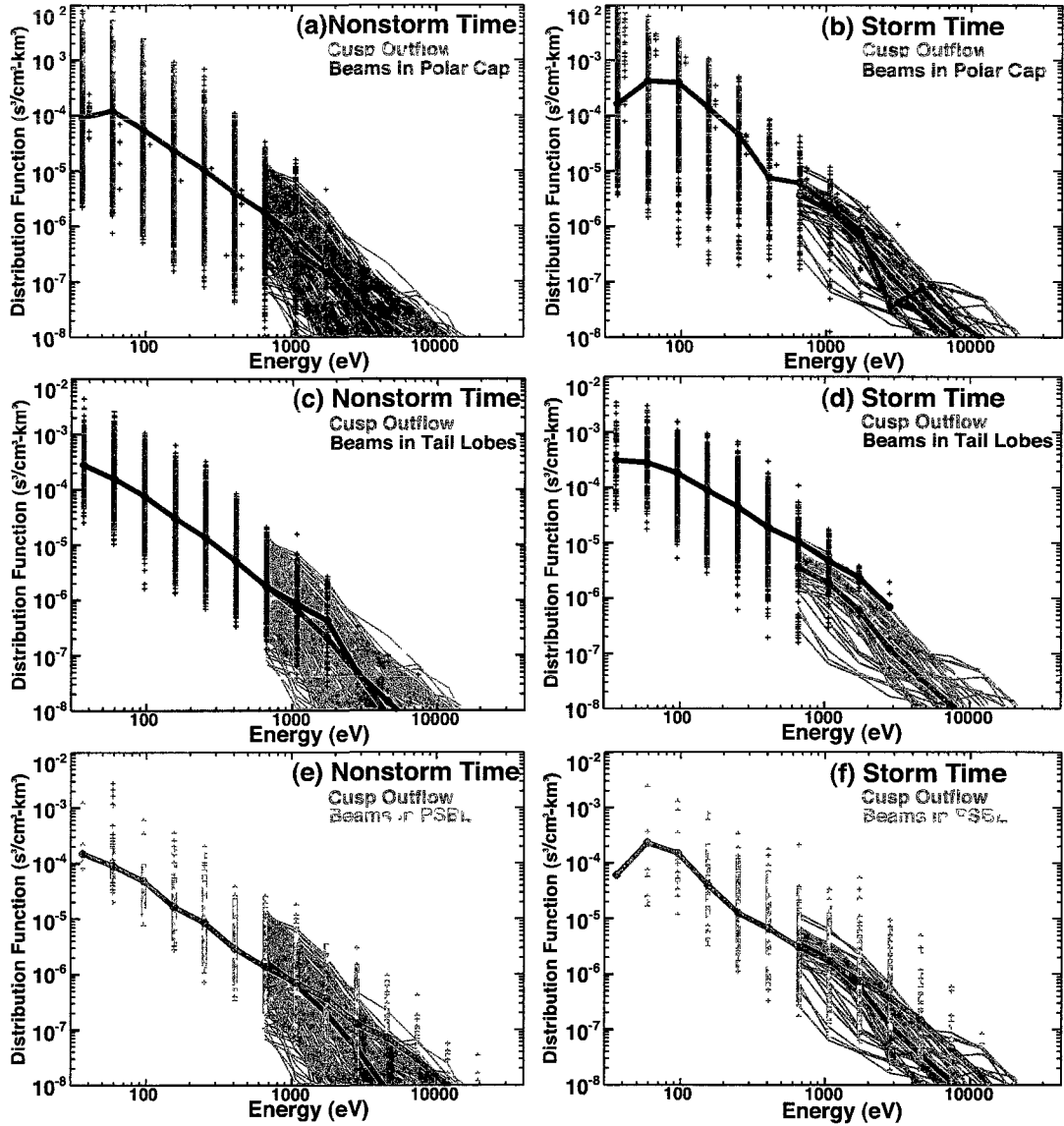
Figure 5-8: Normalized distribution function comparison plots for cusp outflows, orange lines, and steaming O^+ beams observed during nonstorm times (a, c, e) and storm times (b, d, f) within the polar cap (cyan data points in panel a and b), the tail lobe (blue data points in panel c and d), and the PSBL (pink data points in panel e and f). Two thick lines in each plot show the median values for the scatter plots of the cusp outflows (dark red) and O^+ beams. The measurement of the cusp outflows is valid above 500 eV, so lower energy part of the cusp distribution was not plotted. Note that by definition, plasma beta is less than 0.02 in the polar cap and the tail lobes, and larger than 0.05 in the PSBL.

Figure 5-8e-f shows the comparison between the initial distribution and the O$^+$ beam distributions in the PSBL. A clear difference from the tail lobes beam distributions is that there are many more O$^+$ beams above 500eV exceeding the cusp distribution function envelope in the PSBL even during nonstorm times. It indicates that acceleration is occurring when the lobe O$^+$ beams enter the PSBL region even when the magnetosphere is quiet. O$^+$ beams with energies higher than 3keV occurred in the PSBL as well, and almost all of them have a higher distribution function than the cusp outflows. Those ions clearly have a much higher velocity. During storm time, the spread of data points for O$^+$ beams in PSBL is larger compared with nonstorm times. This result implies a much more complicated situation but it is clear that acceleration is definitely occurring during storms for O$^+$ beams entering PSBL from the tail lobes and it can be very strong.
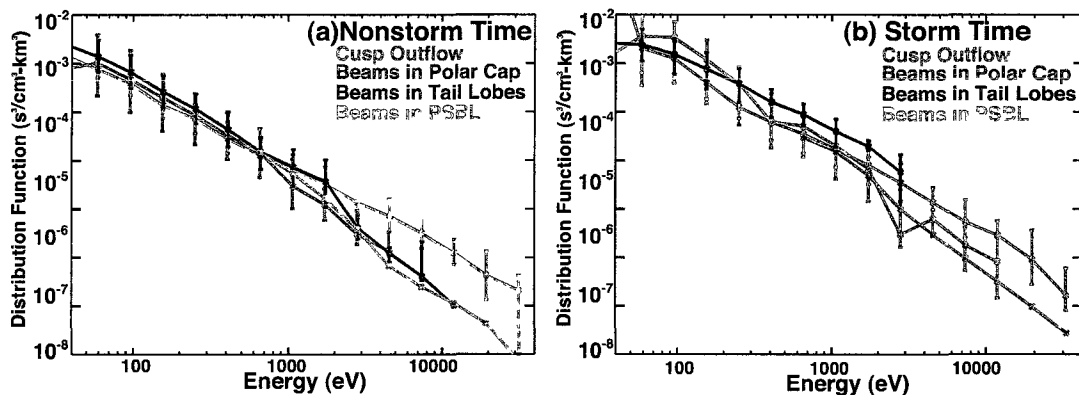
Figure 5-9: The median values of the normalized distributions of cusp outflows (orange), streaming O$^+$ in polar cap (cyan), in tail lobes (blue) and PSBL (pink) for nonstorm and storm times. Error bars represent the 1st and 3rd quartiles.

As for the streaming O$^+$ within the energy range 40eV to 500 eV, one can compare the tail distributions with the polar cap distributions to understand the acceleration from the polar cap to tail lobes and PSBL. Figure 5-9 are plots for median values of the normalized distributions shown in figure 5-8 for nonstorm and storm times. Colors have the same meaning as in figure 5-8. The error bars represent the 1st and 3rd quartiles. The wide

spread of the distribution for most of the energy ranges in the polar cap leads to the large error bars for the polar cap distribution. During both nonstorm and storm time, all median values of distributions overlap each other when the energy is lower than 500eV within the statistical errors. It implies that further acceleration is not necessary from the polar cap to tail lobes, and even into the PSBL, for the O^+ beams at 40 – 500 eV to be observed in the tail lobes, and PSBL, during all times.

5.5   Estimation of the Acceleration

As discussed before and shown in figure 5-9, acceleration seems necessary only for observing high energy streaming O^+ in the PSBL during nonstorm times, and in the tail lobes and PSBL during storm times. In this section, we will estimate how much acceleration is required for the energetic streaming O^+ observed in the tail lobes and PSBL.
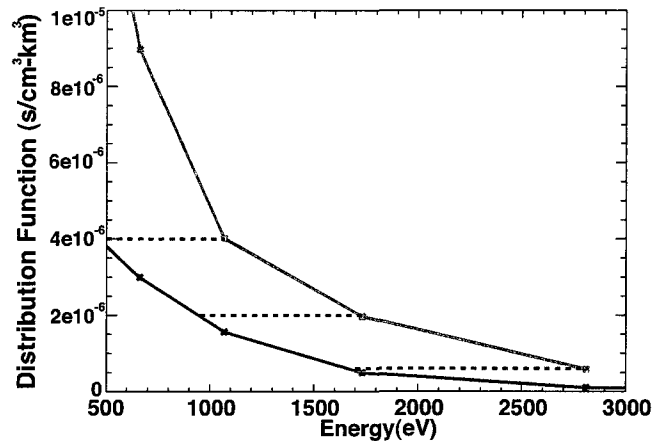
Figure 5-10: Estimation of the acceleration by measuring the difference between the beam distributions, in red, and the initial distribution, in blue. Black dashed lines show the energy increase for the streaming O^+ at certain energy transporting from the cusp to the tail lobes.

Figure 5-10 shows how we makes the estimation for O^+ beams observed in tail lobes during storm times as an example. The plot shows only within the range from 500 eV to

3000 eV, where acceleration is observed. The red line is the median value of the distribution functions observed in the tail lobes and the blue line is the cusp outflow median distribution. The horizontal difference is the shift required to accelerate from the initial distribution to the final distribution. In this way, one can calculate that during storm time, streaming O^+ beams observed in tail lobes at 1000eV have been accelerated by 880 eV, 1700 eV O^+ beams have been accelerated for 780 eV, and 2800 eV O^+ beams have been accelerated by 1100 eV O^+ from the outflow distribution.
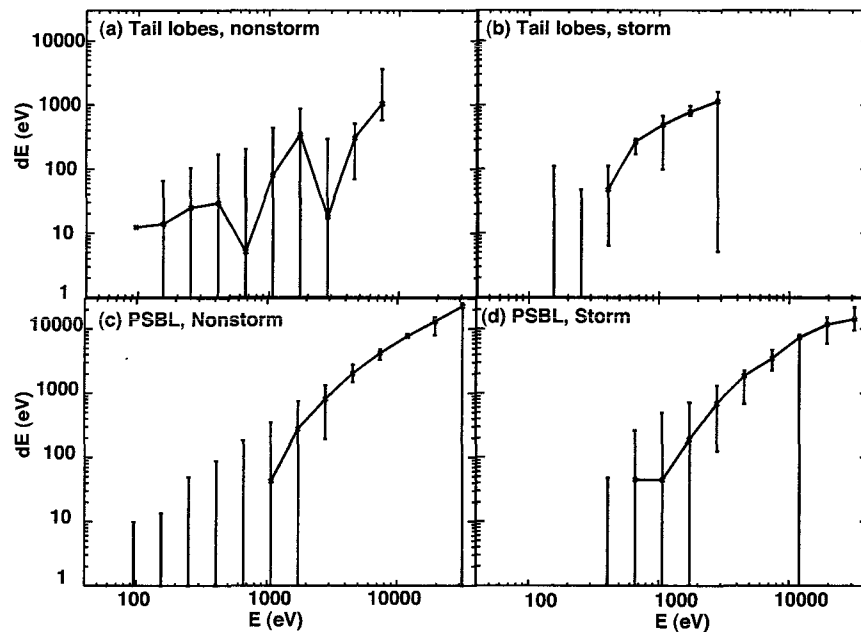
Figure 5-11: Estimated acceleration in eV VS the bulk kinetic energy of the streaming O^+ in the tail lobes and PSBL and during nonstorm and storm times. Error bar are calculated by shifting the 1st and 3rd quartile of beam distribution to the median value of cusp outflows.

The estimation results are shown in figure 5-11. The x-axis shows the energy of the streaming O^+ when it has been accelerated and observed in the tail lobes while the Y-axis shows how much it has been accelerated from the cusp distribution. The error bars are calculated by shifting the 1st and 3rd quartile of the beam distribution to the median value of the cusp outflows. Some points have error bars extending to 0 (no acceleration). Figure

5-11a is for O^+ beams in tail lobes during nonstorm time. Although the line plots have positive values for many energy ranges, the fact that the lower error bars go to 0 means that there is no acceleration needed, as discussed in the last section. There are some indications that energetic beams between 5 keV to 10 keV may need acceleration here but this result is not be convincing, considering the small amount of data collected under this condition, shown in figure 5-8a. During storm times, as shown in figure 5-8b, however, it is evident that streaming O^+ from 400 eV to 2 keV observed in tail lobes have gained 50 eV to 1 keV since they came out from the cusp. On average, they increased about 2/3 of their initial energies from cusp to the tail lobes ($-5R_E$ to $-19R_E$). These numbers are larger than the upper limit of centrifugal acceleration, 20 km/s (32 eV), in the magnetotail lobes given by [55] and much larger than the observational constraints, 5 km/s (2 eV), Nilsson et al. [55] gave on any other acceleration mechanism. Since Nilsson did not categorize his data into different storm phases and most of his data are during nonstorm times, we do not know how much stronger the acceleration would be during storm times. However, the different distribution function and acceleration estimation for O^+ beams in the tail lobes during nonstorm and storm times may indicate different energization mechanisms for quiet times and active times and/or that parameters such as the convection field change significantly when the storm starts.

Figure 5-8c shows, during nonstorm time, that a strong acceleration, i.e. above 800 eV, has to occur from the tail lobes to the PSBL for us to observe energetic streaming O^+ inside PSBL at energies above 3 keV. The acceleration increases for higher energy O^+ beams. The O^+ is accelerated from tail lobes by about 50% to 2 times of their initial energy. During storm times, the acceleration curve is very similar to the nonstorm curve, with larger error bars showing a wider spread of the normalized distribution function of the identified streaming O^+.

5.6 Discussion of the Acceleration Mechanism in PSBL

The PSBL has been found to be a site of intense mass, energy, and momentum transfer [19] and various energization mechanisms have been proposed to explain the evolution and acceleration of the ion beams. However, it was also found that the electric field inside the PSBL often has a high magnitude and high fluctuation [60]. As a result, a sudden increase in $\mathbf{E} \times \mathbf{B}$ drift is expected as O^+ beams enter the PSBL from the tail lobes, as discussed by Hirahara et al. [32]. In order to study the $\mathbf{E} \times \mathbf{B}$ drift effect on O^+ and investigate the real acceleration, we performed a case study of a fast (92 second) PSBL crossing in the north magnetosphere during quiet time.

The left panels of the figure 5-12 provide the basic information for this event. As shown in figure 5-12a-b, Kp is about 2 and AE is lower than 300, indicating a quiet time period with neither storm nor substorm. Figure 5-12c shows the plasma beta, which is used to identify different magnetosphere regions as mentioned earlier in the thesis. The PSBL is defined as plasma beta between 0.05 and 0.5. The two values are marked with the two pink lines. According to this definition, the satellite was in the lobe at the start of the plot, entered the PSBL at 11:37:56, and then entered the plasmasheet at 11:38:45. Two black vertical lines marked the two entry times. Figure 5-12d-e are the energy spectra for O^+ and H^+. The mono-energetic streaming O^+ can be clearly spotted in the lobe, persisted after the satellite entered the PSBL region and disappeared at about 11:38:20. The energy of the O^+ beams increased from 1keV, between 11:36 to 11:37, to 4 keV − 7 keV at 11:38 when the satellite entered the PSBL. A similar beam can also be seen in H^+, but it is not very clear because of the stronger background plasma. A population of energetic H^+ are observed in the later part of the PSBL passing and extended to the plasmasheet region. Similar O^+ at the same energy range but with much smaller flux can also be seen.
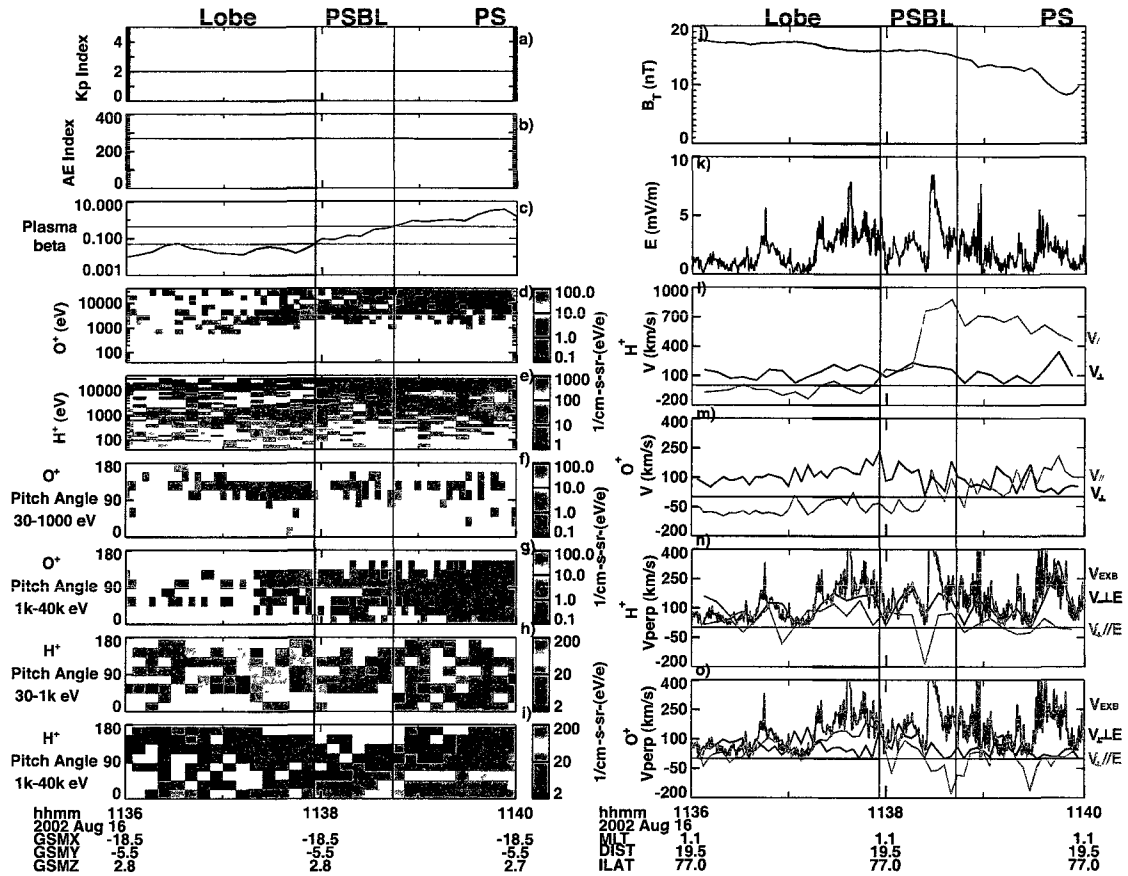
Figure 5-12: Case study of PSBL. Left panels: (a)Kp index; (b) AE index; (c) Plasma beta (pink lines shows the values divide the regions into lobe, PSBL and PS); (d) O^+ energy spectrum; (e) H^+ energy spectrum; (f)-(g) O^+ pitch angle spectra for 30 eV – 3 keV and 3 keV – 40 keV; (h)-(i) H^+ pitch angle spectra for 30 eV – 3 keV and 3 keV – 40 keV. Right panel: (i) Magnetic field; (k) Electric field after filtered with a lowpass filter at 0.1Hz; (l)-(m) Parallel (red) and perpendicular (blue) velocity for H^+ and O^+; (n)-(o)Perpendicular velocity component that is parallel (red) and perpendicular (blue) to electric field for H^+ and O^+. Green lines are $\mathbf{E} \times \mathbf{B}$ drift velocity. Black vertical lines show the entry and exit of the PSBL. Blue shadow marks the period with a clear acceleration.

Figure 5-12f-i are pitch angle spectra for low energy (30 eV – 1 keV) and high energy (1 keV – 40 keV) O^+ and H^+. Streaming O^+ can also be easily spotted in the pitch angle spectra. At the start, they are more anti-parallel to the magnetic field (tailward): the pitch angle is around 150 degree. As the spacecraft approaches the PSBL, at about 11:37:00, the pitch angle became closer to 90 degree, which may be due to acceleration or increased convection drift. Starting at about 11:37:50, the energy of the beam went above 3 keV but the pitch angle remained the same. The pitch angle spectra for H^+ does not have a clear pattern for the lobe beams because of the background. However, the high energy H^+ observed in the energy spectrum is shown here mostly field-aligned (earthward), with a large pitch angle spread. A similar field-aligned energetic O^+ population is only noticeable inside the plasmasheet. Considering the location is around -18R_E, the earthward injection of H^+ and O^+ are possibly part of the population that is ejected earthward due to the reconnection in the more distant tail.

The right panels of figure 5-12 show the field conditions and the calculated moments of H^+ and O^+. The total magnetic field, as shown in figure 5-12j, decreased slowly from the lobe to the PSBL and lowest in the PS. The electric field, shown in figure 5-12k, is from Cluster/EFW and has been filtered with a lowpass filter at 0.1. It still has large fluctuations and the envelope increased when the satellite moved close to the PSBL. figure 5-12l-m show the parallel velocity $V_\parallel$, in red, and perpendicular velocity $V_\perp$, in blue, of H^+ and O^+. For H^+, the earthward injection in the PSBL/PS is more clear: $V_\parallel$ was in tailward direction but changed to earthward when the satellite enters the PSBL and the earthward flow became significantly faster at about 11:38:20. $V_\perp$, on the other hand, did not change much during the entire period. Similarly, $V_\parallel$ of O^+ was tailward at the start but turning earthward at about 11:38:20 with a much lower speed than H^+. $V_\perp$ of O^+ did not change much as well.

Figure 5-12n-o shows the component of the perpendicular velocity that is parallel to the electric field $V_{\perp,\parallel E}$, in red, and perpendicular to the electric field $V_{\perp,\perp E}$, in blue. The green lines plotted in both panels are the same, the $\mathbf{E} \times \mathbf{B}$ convection velocity $V_{E \times B}$. If there is no other acceleration or drift, H^+ and O^+ will have the same perpendicular velocity, which

is the $V_{E\times B}$ convection velocity, and it should be perpendicular to the electric field. In figure 5-12n, the blue line generally overlaps the green line, which means that $V_{\perp,\perp E}$ of H^+ is mostly from the $V_{E\times B}$ drift. However, the perpendicular velocity component is not small either, indicating that there is another drift or acceleration mechanism for H^+. For O^+, $V_{\perp,\perp E}$ does not follow the $V_{E\times B}$ drift line that well. They were close at the start when the electric field is still small but separate whenever $V_{E\times B}$ went above 200km/s (3.2 keV). A reasonable guess for this issue is that when electric field goes up, the velocity of O^+ increases so much that it went above the CODIF energy range. However, 3.2 keV is not big enough to move the major part of O^+ above the instrument energy range and there is not clear sign in the energy spectrum showing that a large part of O^+ disappeared when the electric field became larger. A mass dependent acceleration or drift moved O^+ in the opposite direction of the $V_{E\times B}$ when the electric field is large. The $V_{\perp,\|E}$ of O^+ is comparable to the one of H^+ but it is more clear that this component is small in the lobe region, increase near the PSBL and largest inside the PSBL. Although fluctuates a lot, this component can reach 200km/s (3keV) from time to time, which indicates that some acceleration or drift parallel to E acted on the O^+ ions.

During the period from 11:37:10 to 11:38:00, as marked by the blue shadow: the energy of streaming O^+ beam increases from 1.5 keV to 4~7 keV there is a sudden increase in the electric field, $V_\|$ is very small for both H^+ and O^+, $V_{\perp,\perp E}$ of H^+ follows $V_{E\times B}$ (around 200km/s) and $V_{\perp,\perp E}$ of O^+ decreases to about 50km/s, $V_{\perp,\|E}$ of H^+ and O^+ are similar, around 150 km/s (1.8 keV) and in the same direction as the electric field. Thus, O^+ during this period has been accelerated and/or has a large drift velocity except $V_{E\times B}$ when they approach the PSBL and the acceleration amount is at least 1.8 keV.

The acceleration pattern is more clear if we look at the O^+ 2D phase space density (PSD) plots at start and end of this period, as shown in figure 5-13. X-axis and Y-axis are $V_\|$ and $V_\perp$. The $V_\perp$ is taken at the direction when the magnitude of $V_\perp$ is the largest. Panel a shows a clear lobe beam distribution with both $V_\|$ and $V_\perp$ at 100km/s. The PSD in panel b has two populations. The left one has a similar $V_\|$ as the PSD in panel and a larger
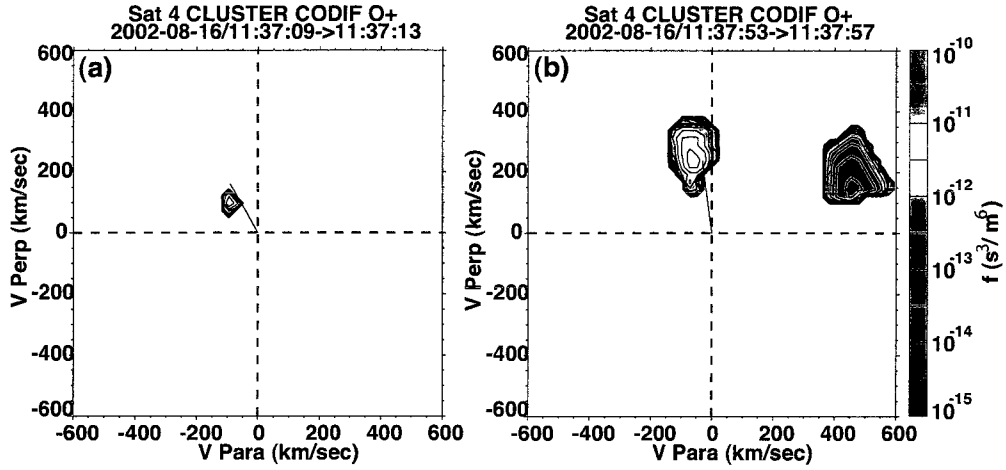
Figure 5-13: 2D Phase space density plots for (a) the start and (b) the end of the selected period as shown in the blue shadow in figure 5-12.

$V_\perp$ with a large velocity spread. It highly possible that the streaming O^+ observed here is from the same source as the one observed in the lobe region because they have the same $V_\parallel$. The shift of the center of the distribution in $V_\perp$ direction (220km/s) is mostly due to the $V_{E \times B}$, which has a mean value of 192 km/s during this period. The wide spread in the $V_\perp$ represents a high perpendicular temperature, indicating that it is the acceleration rather than drifting that is responsible for the high $V_{\perp, \parallel E}$ of O^+ ions and increased streaming O^+ peak energy. However, fast fluctuations of the drift speed can also lead to the same result. The other population with positive and high $V_\parallel$ is in earthward so it may be from the similar mechanism as discussed before for the earthward injection in PSBL/PS region at later time.

The most probable candidate for the acceleration mechanism is the perpendicular electric field acceleration. Theoretically, ions can accelerate along the perpendicular electric field if it is in non-adiabatic motion [12]. In a model in which the magnetic field is perpendicular to the electric field and the direction of the E field and its gradient is in x-axis, the ion motion will be non-adiabatic if

$$\frac{m_i \nabla E_\perp}{eB^2} > 1 \tag{5.2}$$

This condition is sensitive to ion mass and is easier to satisfied with heavy ions (O^+) than light ions (H^+). Once satisfied, the ion will be constantly gaining energy from the electric field rather than gyrating. The energy change can be calculated from $e\Phi$. We studied the period marked with blue shadow before. The method is the same as described in [49] and is shown in figure 5-14.
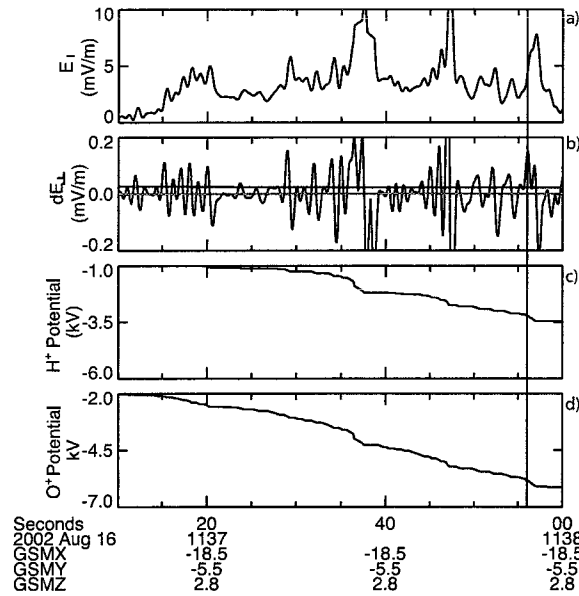
Figure 5-14: Perpendicular electric field study for the period marked in blue shadow figure 5-12. Panels from top to bottom are: a) Perpendicular electric field; b) Gradient of the perpendicular electric field. Blue and red lines show the critical value for O+ and H+ to be accelerated in non-adiabatic motion; c)-d) Calculated possible potential increase from perpendicular electric field for H^+ and O^+.

The panel a and b in figure 5-14 are the perpendicular electric field E and gradient of the perpendicular electric field $\nabla E_\perp$. Red and blue lines in panel b show the critical value, above which O^+ and H^+ become non-adiabatic. As stated before, the electric field in PSBL has large amplitude. Figure 5-14b shows the gradient of the perpendicular electric

94

field $\nabla E_\perp$. Blue and red lines shows the critical value for O^+ and H^+. When $\nabla E_\perp$ above the critical value, ions can be accelerated. Thus, while both ions can be accelerated from time to time, there is a longer time when O^+ ions are in non-adiabatic motion. Figure 5-14c and d show the possible acceleration for H^+ and O^+ from the perpendicular electric field acceleration mechanism if the boundary layer moves at the same speed as used in by Lindstedt et al. [49]. We could not determine the boundary layer speed with the method mentioned in the paper because the spacecraft were too far apart so that the observations from SC4 is not similar enough to the other spacecrafts to make the estimation. Moreover, because our PSBL passing is actually much longer than the one in the paper, a cusp/BL passing, it is not as accurate for us to assume that the PSBL was still during the whole period shown in 5-14. Hence, figure 5-14c-d are really just a rough estimation. However, the estimations do show that H^+ may increase 2.5 keV and O^+ may increase 4keV. They are within the range of O^+ beams energy increases (3~6 keV) but larger than the calculated $V_{\perp,\|E}$ (1.8 keV). Considering the $V_{E\times B}$ is about 3keV, the perpendicular acceleration seems to be large enough to provide the observed energy. However, a better way to estimate the PSBL structure is required in future studies. Due to the fluctuation properties of the electric field, a statistical study is not appropriate here.

Other candidates for the acceleration at this region includes wave heating mechanism and slow-mode shock acceleration [66]. However, because our study mainly focuses is on the streaming O^+ acceleration in the tail lobes, we will leave the detailed PSBL acceleration study to future work.

Chapter 6

SOLAR CYCLE DEPENDENCE

The Cluster satellites were launched in 2000 and 11 years later they are still operating in space. As a result, Cluster data covered the entire declining phase of solar cycle 23, from the solar maximum around 2001 to 2002 to the famous long deep solar minimum that finished in the end of 2008, and the start of the solar cycle 24, from 2009 until now. Thus, Cluster/CODIF is ideal for studying the solar cycle dependence of the transport path of the streaming O^+. In this chapter, we will discuss about how the occurrence frequency of the streaming O^+ at different locations changes from year to year and what this implies about the change in the outflow and of the transport path of cusp origin O^+ during the solar cycle. Data used in this chapter are from 2001 to 2009. We also include only the observations in the lobes (plasma beta less than 0.05) in this chapter so the result will clearly represent the transport path of cusp origin O^+ before they enter the plasma sheet.

As mentioned in chapter 3, the efficiency of CODIF has decreased over the years. As a result, low plasma fluxes that were captured by the detector in earlier years are now missing, which leads to a reduction of the O^+ occurrence frequency. In order to eliminate the effect so we are able compare the occurrence frequency between different years, we set a threshold using energy flux, which is proportional to counts, the unit of the raw data. A close investigation shows that in 2008-2009, the lowest energy flux that can be detected by all anodes is around 2000 $eVcm^{-2}s^{-1}sr^{-1}(eV/e)^{-1}$. Hence, we used this as the energy flux threshold for all years, so we can confidently compare the change of the O^+ occurrence frequency between years, to determine the evolution of its transport path from the cusp during the solar cycle declining phase.

6.1 Orbit Coverage

Figure 6-1 shows the orbits of Cluster satellites inside the magnetosphere in the XZ_{GSM} plane from 2001, figure 6-1a, to 2009, 6-1i. The definition of the magnetosphere is the same as in Chapter 3. The orbits are symmetrical in the north and south in 2001, slightly shifted southward from 2002 to 2004, and starting from 2006, the majority of the orbit was in the south of the magnetosphere. The change of the orbit allows the observation of the equatorial inner magnetosphere but it also limits our observation of the north lobe region in the later years. However, the comparison in the south lobe should be reliable considering the generous coverage Cluster has during all years.
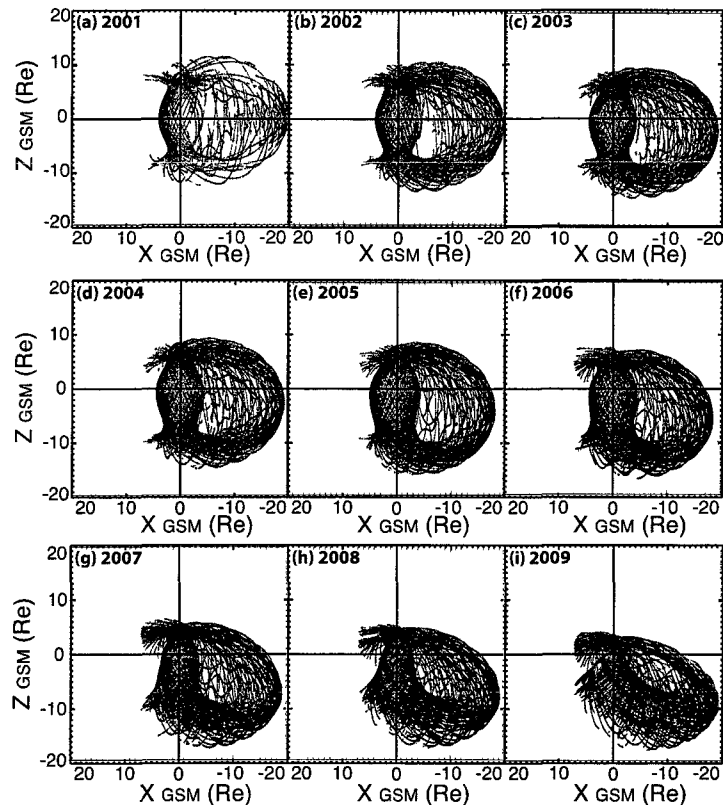
Figure 6-1: Cluster orbits inside magnetosphere from 2001 to 2009 in XZ_{GSM} plane. Upstream and magnetosheath are eliminated as described in Chapter 3.

6.2 Solar Conditions during Solar Cycle Declining Phase

As discussed in the introduction, the solar radiation flux, the solar wind and the IMF have driving effects on cusp outflows and the convection field, as well as on the O^+ concentration in different regions of the magnetosphere. The 10.7 cm solar radio flux, F10.7, which is a proxy for the solar EUV, has a strong positive correlation with ion outflow fluence, defined as the mean net outflow rate, and the correlation is stronger for O^+ than H^+. Ionospheric outflows also respond to the solar wind pressure, velocity, density and electric field [15]. Due to pressure balance, strong solar wind pressure compresses the magnetosphere so it becomes smaller, and thus pushes streaming ions closer to the center. Solar wind pressure is also associated with enhanced outflow, although the mechanism is not clear. Solar wind velocity, on the other hand, can directly influence the solar wind convection field, which will map into the magnetosphere through reconnection. As a result, a strong solar wind velocity will lead to a strong E cross B drift, which will pull the transport path of ions closer to the center. The polar cap potential drop is also found to increase with the magnetospheric activity index Kp [?]. Hence, before we study the dependence of the transport path of the cusp origin O^+ on solar cycle, we researched the values of some critical parameters that may influence the outflow and the transport path.

Figure 6-2 shows the external conditions from 2001 to 2009. Data are from the OMNI website except the EUV data that are from the CELIAS/ SEM experiment on SOHO. All data are averaged for every 27 days except the sunspot number (every hour) and F10.7 are averaged for every hour and EUV is averaged for each day. Blue lines indicate the year boundaries. As shown in figure 6-2a-c, EUV decreases as the sunspot number decreases and so as the F10.7 solar radio flux, indicating the solar cycle declining phase. There is a slight increase of both in 2009 compared with 2008. Other parameters have a more complicated behavior. Solar wind pressure, shown in figure 6-2d, does not follow the trend of sunspots. The value is around 2 nPa from 2001 to 2003 and in 2005, low at 1.5 nPa in 2004 and gradually drops from 1.7 nPa to 1.3 nPa during 2006-2009. Solar wind velocity is around 400 km/s during all years plotted except in 2003 it is around 500 km/s and in 2009 it drops
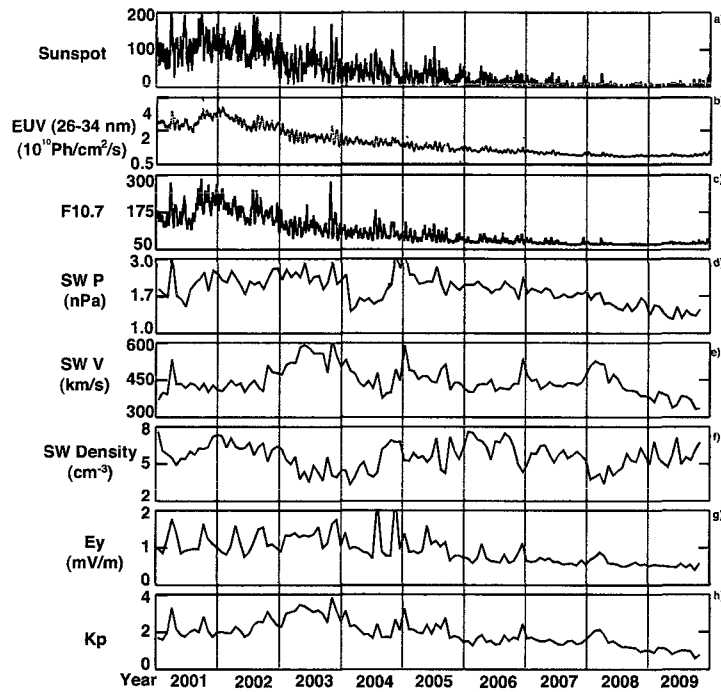
Figure 6-2: External conditions from 2001-2009. Panels from top to bottom: (a) Sunspot, (b) EUV, (c) F10.7, (d) Solar wind pressure, (e) Solar wind velocity, (f) Solar wind density, (g) Solar wind electric field Y component, (h) Kp index. All Data are from the OMNI website except the EUV data are from the CELIAS/ SEM on SOHO. Sunspot and F10.7 are averaged over every hour, EUV is averaged for each day and all other data are averaged for every 27 days.

close to 350 km/s. Solar wind density, 6-2f, is between 5 to 7 cm^{-3} during 2001-2009. Figure 6-2g shows the Y component of the solar wind convection field. The value of Ey is around 1 from 2001 to 2005 and then drops towards the end of 2005, to a value below 1 mV/m. The trend of the Kp index average values, as shown in the last panel in figure 6-2h, is similar to solar wind velocity: around 2 for 2001-2002 and 2004-2005, but higher at 2.5 in 2003 and lower at 1.5 in 2006-2009. Hence, although the ionosphere outflows is expected to decrease from 2001 to 2009 due to the declining solar UV in the declining phase of the solar cycle, because the change of solar wind pressure and velocity is so irregular, the change in the convection and, as a result, the transport path of the cusp outflows may be rather complicated.

6.3 Occurrence Frequency Changes from 2001 to 2009
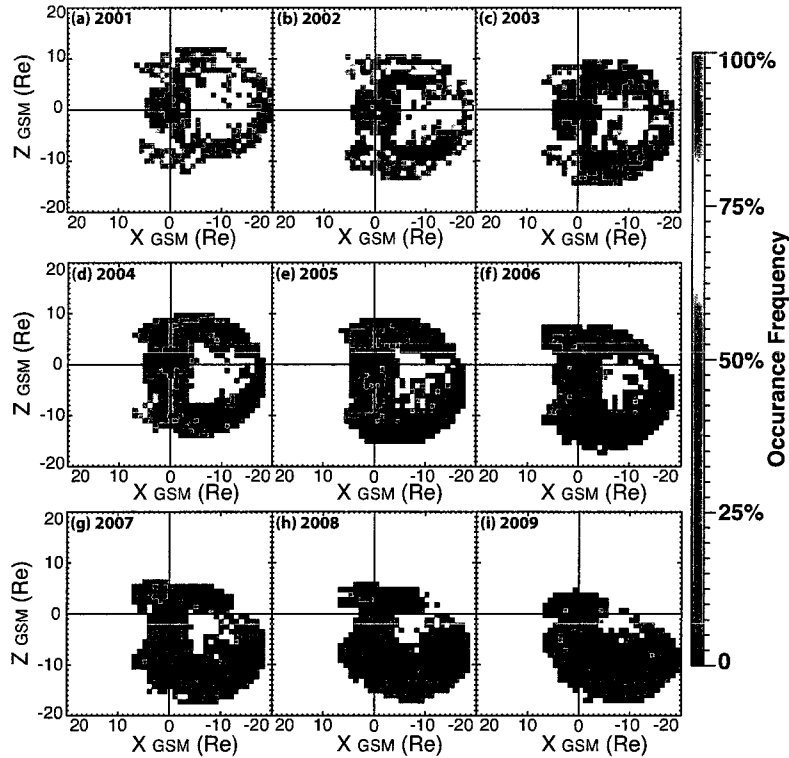
Figure 6-3: Occurrence frequency maps of streaming O^+ observed in the lobes from 2001 to 2009 in XZ_{GSM} plane for nonstorm times.

As discussed in earlier chapters, occurrence frequency can represent the most probable transport path for O^+. Figures 6-3 and 6-4 show the occurrence frequency maps for streaming O^+ observed in lobes from 2001 to 2009 in XZ_{GSM} plane for nonstorm and storm times. During nonstorm times, the occurrence frequency in the polar cap is similar during 2001 and 2002, ranging from 70% to 100%. It starts to decrease in 2003 and 2004 to about 50% to 70%, goes to around 25% in 2005 and drops lower and lower from 2006 to 2008. In 2002, more O^+ is observed in the south than in the north polar cap, but in 2008 there is almost no streaming O^+ observed in the southern polar cap but there are still some regions with 25% occurrence frequency in the north. During 2009, the start of the solar cycle 24
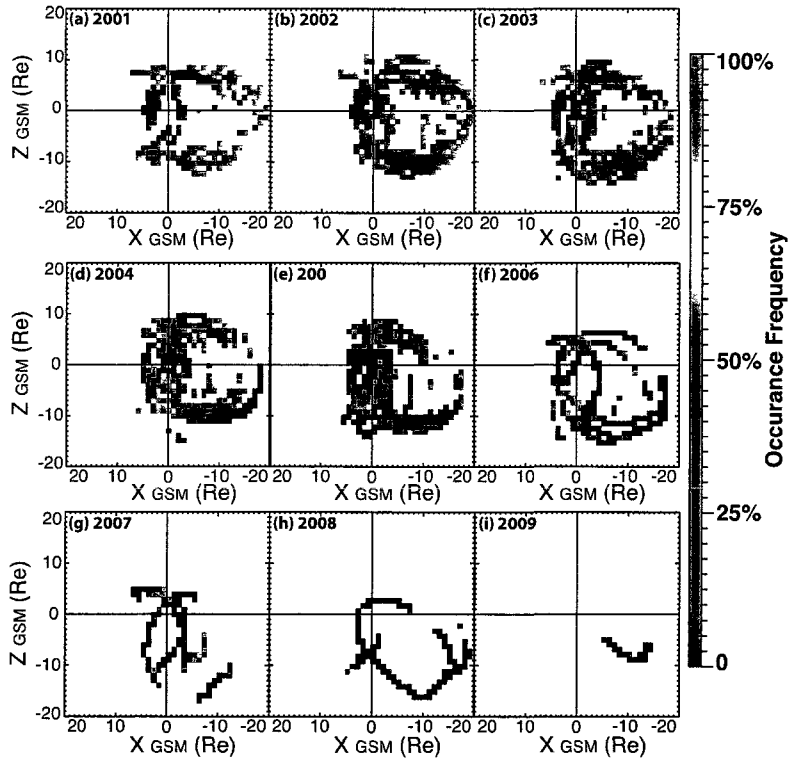
Figure 6-4: Occurrence frequency maps of streaming O^+ observed in the lobes from 2001 to 2009 in XZ_{GSM} plane for storm times.

rising phase, O^+ observed in the north is less than 2008 but in the south the probability to observe streaming O^+ went up a little. Compared to the graduate decrease of the occurrence frequency during the solar cycle declining phase, the drop in the tail lobes is more significant. During 2002, the chance of observing streaming O^+ in the tail lobes is around 60% but starting in 2004, there is already very little streaming O^+ observed in most of the regions inside the tail lobes. Most of the time during the nonstorm period of 2005-2009, Cluster did not observe any streaming O^+ inside the tail lobes.

Although the occurrence frequency during the storm times is much higher than nonstorm time, we see a similar story. The probability of observing streaming O^+ inside the polar cap gradually decreases from 100% in solar maximum, 2001-2002, to about 80% in 2003-2004, and then to 30% during 2005. Occurrence frequency is as high as 100% in the south tail

lobes and around 50% in the north during 2001 and 2002. During 2003, it drops to 50% in both lobes and during 2004-2006, it is varies from 0% to 30% depending on regions. Some high values around the edges are likely due to the low statistics. Because there are few storms from 2007 to 2009 due to the low solar activity, the coverage of data is also not good enough to make a statement in this case.

To sum up, during both storm and nonstorm times, the occurrence frequency of the streaming O^+ inside the polar cap decreases gradually along the solar cycle declining phase. It drops significantly in 2004, when the solar wind pressure is lower than all other years, and drops further during 2005-2007. Although it is reasonable to expect the reduction of the occurrence of streaming O^+ due to the lower and lower outflow rate, the stronger and more sudden decrease in the tail lobes indicates that the transport path is also changing during the solar cycle declining phase.
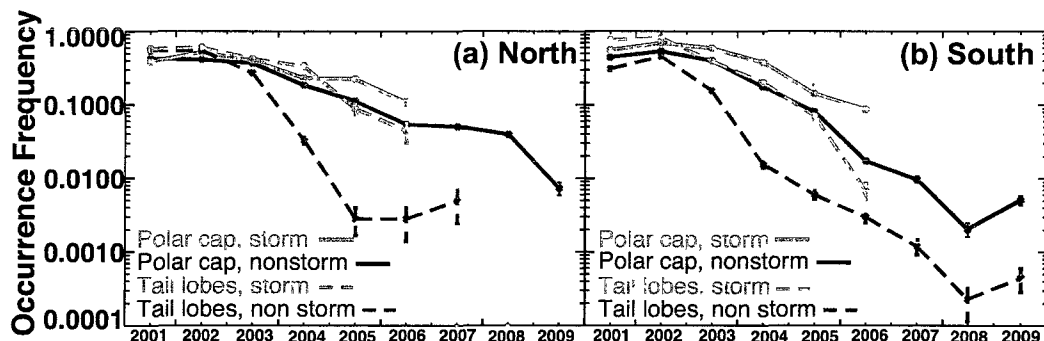
Figure 6-5: Occurrence frequency VS years plots for (a) north and (b) south. Pink and blue lines show the occurrence frequency during storm and nonstorm times respectively. Solid lines are from polar cap data and dashed lines are from tail lobes data. The error bar is one standard deviation. Results for the storm times in 2009 was discarded for statistics reasons.

In order to do a more quantitative analysis of the occurrence frequency drop in different regions during the solar cycle declining phase, we calculated the occurrence frequency for each year and categorized it into different regions as shown in figure 6-5. The error bar is one standard deviation. Results for storm times in 2009 have been discarded because the statistics are too low. We divided the magnetosphere into north and south with Z_{GSM}

because, as shown before, the orbit evolves more southward every year. However, it turns out that the trends for the changing of the occurrence frequency are similar for the north and south magnetosphere. Overall, the occurrence frequency, as can be also seen from figure 6-3 and figure 6-4, is going down during this declining phase of the solar cycle. The occurrence frequency decreases faster in the tail lobes than in the polar caps, during nonstorm times than during storm times. In 2001-2002, the occurrence frequency of O^+ beams observed in the polar cap is the same as that observed in the $-20R_E$ tail lobes, while in later years, although there is still a decent amount of O^+ beams in the polar cap, there are very few O^+ beams observed in the near-Earth tail lobes. In 2009, when the solar activity starts to increase, the occurrence frequency for nonstorm times starts to increase too, both in the polar cap and tail lobes.

	North Polar Cap	North Tail Lobes	South Polar Cap	South Tail Lobes
Nonstorm	8 (2007)	112 (2007)	252 (2008)	1743 (2008)
Storm	5 (2006)	14 (2006)	8 (2006)	123 (2006)

Table 6.1: Reduction factors of the occurrence frequency from solar maximum (2002) to solar minimum. For storm time, we consider 2006 as solar minimum because of the low statistics in the later years. For nonstorm time, we consider 2007 as solar minimum for north hemisphere because of the low orbit coverage for north tail lobe in 2008.

Table 6.1 sums up the reduction factor of the occurrence frequency from solar maximum (2002) to solar minimum (various and depending on availability). The reduction factor ranges from 5 to 252 for polar caps and from 14 to 1743 for tail lobes. During nonstorm times, the reduction factors are about 7 to 14 times bigger for tail lobes than polar cap and during storm times they are 3 to 15 times bigger. Hence, the differences between the reduction factors are comparable for storm and nonstorm time.

We explore three possible explanations for the significant difference between the reduction factors for the polar cap and for the tail lobes. As stated in the last chapter and shown in the bulk kinetic energy maps in figure 5-3, streaming O^+ observed in the tail lobes have

on average a higher velocity than those observed in the polar cap. Thus, if the outflow spectrum becomes softer, i.e. the distribution function decreases more at higher energies, this could preferentially affect the near-Earth tail lobes.
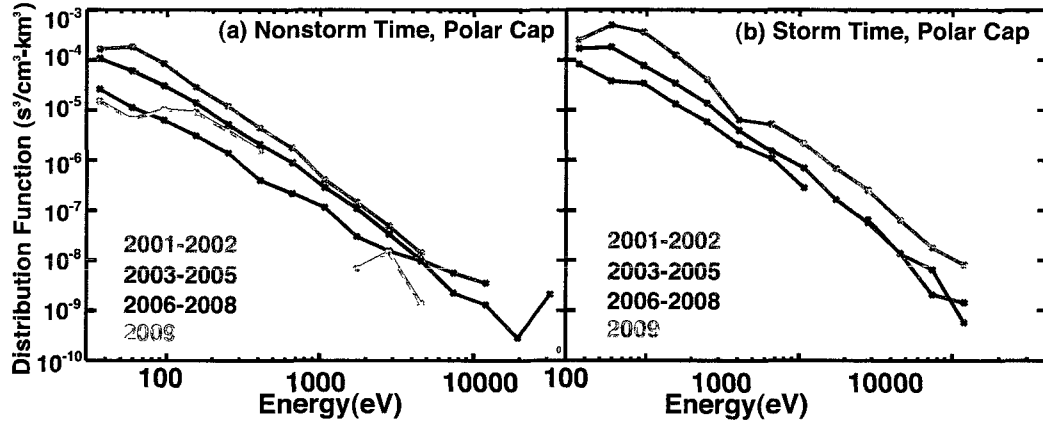
Figure 6-6: Median distribution function of the streaming O^+ inside the polar cap for solar maximum (2001-2002), transition time (2003-2005), solar minimum (2006-2008) and the start of the new solar cycle (2009).

Figure 6-6 shows the median distribution function for all steaming O^+ inside the polar cap for different years, where, as in figure 5-8, we have used the beam distribution function at the peak energy of the beam. During nonstorm times, it decreases at all energy ranges from solar maximum (2001-2002, in red) to the transition time (2003-2005, in green), and to the solar minimum (2006-2008, in blue). The difference is bigger for energies lower than 1keV and smaller for higher energies. The mean decreasing factor from the solar maximum to the solar minimum is about 8 and the biggest decreasing factor is about 16, which is for O^+ around 50eV. The trend of the distribution functions changes during storm times are similar to that at nonstorm time: the distribution function of low energy O^+ decreases more than the high energy O^+. The mean and max decreasing factors are 7 and 13 at storm time, which are slightly smaller than those for nonstorm time. As a result, the outflow distribution function becomes harder rather than softer in the solar cycle declining phase for all geomagnetic active level, so this cannot be the reason for the missing streaming O^+

104

in tail lobes. We also plotted the distribution function for 2009 in pink. There are no beams observed at storm times in 2009. For the O^+ beams observed at nonstorm times in 2009, the distribution function is higher than the one in at solar minimum for energy ranging from 100eV to 500eV. It implies that, as was observed for the occurrence frequency, the distribution function of the O^+ in polar cap increases as the solar cycle comes back up.
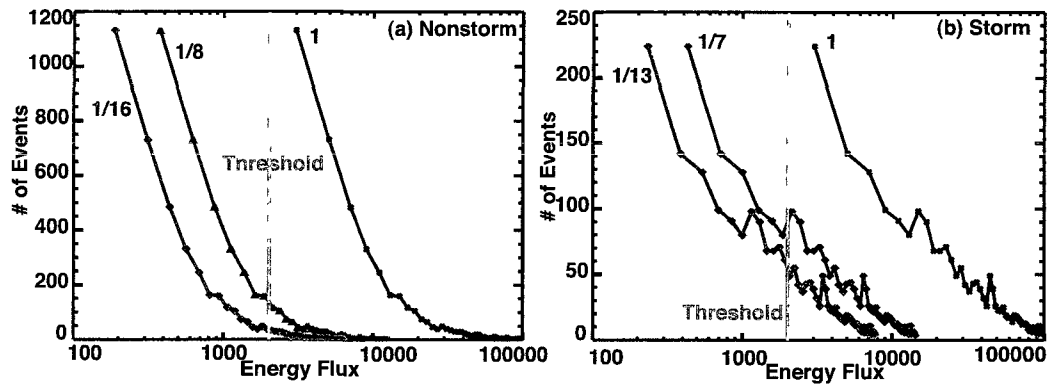
Figure 6-7: Occurrence distribution VS energy flux for O^+ beams in the tail lobes observed during (a) nonstorm times and (b) storm times of solar maximum time (2002). Black lines are the original distribution. Light blue and green lines are the distributions when the energy flux is reduced to a fraction (1/8 and 1/16 for nonstorm time, 1/7 and 1/13 for storm time) of the original values.

A second possibility is that if the distribution function of the beams decreased during the declining phase of the solar cycle, more beams now fall below the energy flux threshold, so that, although the beams are there, we no longer observe them. As stated at the start of this chapter, we introduced an energy flux threshold at 2000 $eVcm^{-2}s^{-1}sr^{-1}(eV/e)^{-1}$ to eliminate the effect of the decreasing efficiency of CODIF. If the flux of the outflow is reduced, a greater fraction of the O^+ will fall below the energy flux threshold in the tail because the flux tube is bigger in the tail lobes, and so the energy flux of the streaming O^+ is reduced. As discussed before, during nonstorm times the distribution function of the streaming O^+ in the polar cap during solar minimum time is usually about 1/8 (can be as low as 1/16) of the one observed during solar maximum and the reduction factor is about

1/7 (can be as low as 1/ 13) during storm times. If we assume that the energy flux of the

O^+ beams in the tail lobes has a similar change from solar maximum to solar minimum as in

the polar cap, we can calculate the fraction of O^+ beams that would still remain above the

energy flux threshold. Figure 6-7 shows the occurrence distribution of the O^+ beams versus

energy flux for streaming O^+ observed in the tail lobes during (a) nonstorm times and (b)

storm times of solar maximum time (2002). Black lines represent the original distribution.

Light blue and green lines show the occurrence distribution when the energy flux is reduced

to a certain fraction of the original one. The pink line represents the threshold. During

both quiet and storm times, a large fraction of the O^+ will fall below the threshold and

thus would be missing in the occurrence frequency analysis. A larger fraction of the O^+ is

missing during nonstorm times than during storm times.

Dropping Factor	1	1/8	1/16	1/7	1/13
# of Events above Threshold, Nonstorm	4115	871	334	/	/
% of Events above Threshold, Nonstorm	100%	21.2%	8.1%	/	/
# of Events above Threshold, Storm	2030	/	/	1266	810
% of Events above Threshold, Storm	100%	/	/	62.4%	39.9%

Table 6.2: List of the number of events above the energy flux threshold after flux deduction
and their fractions to the original distributions.

Table 6.2 lists the number of events above the threshold after the energy flux reduction

and its fraction of the original number of events. On average, the occurrence frequency

would be reduced to 21.2% of the original rate during nonstorm times. Even if we consider

the extreme case when the energy flux drops to 1/16 of the original value, there still should

be 8.1% of the total O^+ detected in the tail lobe, which is still much greater than the

occurrence frequency drop of 1/112 in the north lobe or 1/1743 in the south lobe as observed.

Similarly, during storm times, there should be at least 39.9% of the O^+ observed in the tail

lobes rather than 1/14 or 1/ 123 as observed in north and south. Hence, although it is clear

that the observed reduction in flux causes a large amount of streaming O^+ to fall below the

energy flux threshold, it is not large enough to explain the strong decrease of occurrence

frequency observed inside the tail lobes.
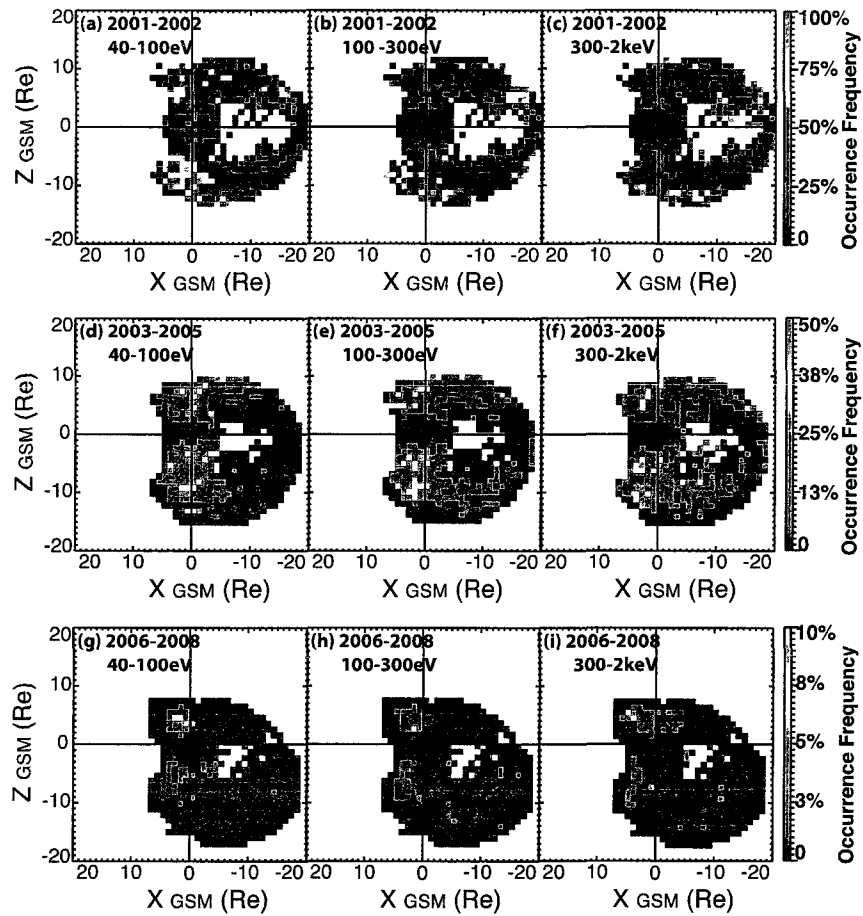
Figure 6-8: Nonstorm times occurrence frequency maps in XZ_{GSM} plane for streaming O^+ within bulk kinetic energy ranges at 40 eV – 100 eV, 100 eV – 300 eV and 300 eV – 2 keV during solar maximum time at 2001-2002 (a-c), transition time at 2003-2005 (d-f) and solar minimum time at 2006-2008 (g-i). Occurrence frequency maps are not in the same scale for different time periods.

The third possible cause is that the transport path to the lobe may have changed, so the outflow is going somewhere outside the orbits during later years. Indications can be found in figure 6-8, the nonstorm times occurrence frequency maps in XZ_{GSM} plane during solar maximum at 2001-2002 (a-c), transition time at 2003-2005 (d-f) and solar minimum at 2006-2008 (g-i) for the streaming O^+ in different bulk kinetic energy ranges.

Since the occurrence frequency can represent the probability to observe O^+ at different locations, locations with high occurrence frequency can be considered as part of the main transport path of O^+. We sorted the maps for different energy ranges because the velocity filter effect separates the transport path of the streaming O^+ within different energy ranges. Streaming O^+ with energy higher than 2keV are not a major contribution and as result it is hard to identify the transport path for them at this region. Similarly, the occurrence frequency in 2009 is also too weak for us to make any statement about the change of the transport path, so we left all of them out in figure 6-8. The scales for different time periods are different.

During solar maximum (2001-2002) for streaming O^+ with bulk kinetic energy between 40eV and 100eV, as shown in figure 6-8a, O^+ from the north cusp can be observed in the polar cap and tail lobes with a gradually decreased occurrence frequency while O^+ in the south has moved out of the orbital coverage location before $-10R_E$. For relatively faster O^+, from 100 to 300 eV, as shown in 6-8b, the transport path has changed. In the north, the occurrence frequency is lower than what is observed for the low energy beams at the region where X_{GSM} is closer than $-10R_E$ region but higher when X_{GSM} is further than $-10R_E$. There is also a region on the very dayside with a relatively high occurrence frequency on the dayside showing that those beams are transporting more sunward than the lower energy beams so they cannot be observed around the polar cap and they arrive the near-Earth lobe further then the beams around 40-100eV. The change of the streaming O^+ occurrence frequency is even more clear in the south, indicating that the transport path is higher in the altitude for faster beams, as expected. Similar, but even stronger, is the trend for streaming O^+ at even higher energy range (300 – 2k eV), as shown in figure 6-8c.

In the north streaming O^+ cannot be detected often in the polar cap but there is a higher probability for them to be observed in the tail lobe while in the south the transport is at even higher latitude.

During the transition time (2003-2005), as shown in figure 6-8d, the transport path of the streaming O^+ from 40 eV to 100 eV has clearly move more upward in the north, compared with 6-8a, and in the south, it seems that the transport path of the streaming O^+ is now moving from cusp to the dayside polar cap and even more sunward after that, where there is within the spatial coverage. The displacement of the transport path can be seen even more clearly for streaming O^+ at energy ranges at 100 eV – 300 eV and 300 eV – 2 keV, as shown in figure 6-8e and f, compared with figure 6-8b and c. The probability to observe O^+ in the tail lobes has dropped much lower at those time, although there still some of the streaming O^+ from 100 – 2 keV.

During solar minimum time (2006-2008), as shown in figure 6-8g-i, we mostly observe streaming O^+ in the polar cap even for all energy ranges in both north and south hemisphere, although the occurrence frequency is higher in the north than in the south.

Another approach to find the hint of the changes in the transport path is to check the asymmetry of the transport path. As discussed in chapter 4, during 2001-2002, O^+ from the cusp are transported with an asymmetry that is driven by IMF B_y and strongly influenced by ionosphere convection patterns. Figure 6-9 are IMF B_y sorted occurrence frequency maps in the YZ_{GSM} projection plane for different times in the solar declining phase. The occurrence frequency scales for different time periods are different. During solar maximum time, as shown in figure 6-9a-b, there is a clear north-dawn and south-dusk asymmetry when IMF B_y is greater than 3nT while the asymmetry is not so clear has reversed in the north when IMF B_y is less than -3 nT. During 2003-2005, as shown in figure 6-9c-d, for both conditions the occurrence frequency is mostly even in the south and enhanced on the dawnside in the north. Only when IMF is bigger than 3nT, as shown in figure 6-9d, the occurrence frequency in the north is similar to what is observed during the solar maximum time. There may be asymmetry in the transport path in the south as well but the lack
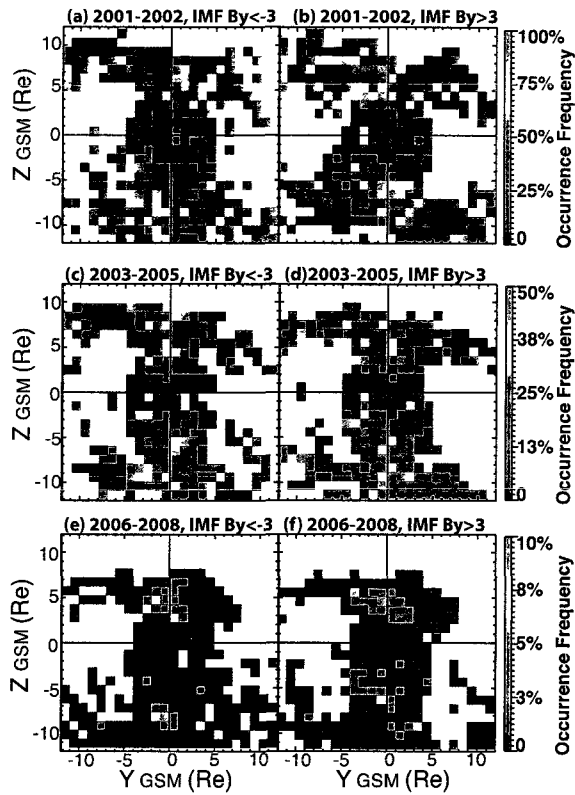
Figure 6-9: Occurrence frequency maps in YZ$_{GSM}$ plane for IMF B$_y$ > 3 nT, and IMF B$_y$ < -3 nT during solar maximum (2001-2002) in a-b , transition time (2003-2005) in c-d, solar minimum (2006-2008) in e-f. Occurrence frequency maps are not in the same scale for different time periods.

of observations in the south-dawn make it difficult to make this statement. When IMF is less than -3 nT, the asymmetry is even opposite than what we observed during the solar maximum time. One possible explanation is that the non-IMF B$_y$ elements that control the streaming O$^+$ transport path has becomes dominate during the transition time. During solar minimum, as shown in figure 6-9e-f, similar as in 2003-2005, the occurrence frequency maps are very alike for IMF greater than 3 nT and less than -3 nT. The location where O$^+$ is observed during the solar minimum time are mostly at the center over the polar cap where O$^+$ just comes out of the cusp, so it is reasonable not observing any asymmetry at this location. Overall, the asymmetry that was clearly observed in the solar maximum time has changed during the later years of the solar cycle declining phase, which supports the

conclusion we made before that the average transport path of cusp origin O^+ has moved away from the Cluster orbits in the later years of the solar cycle declining phase.

A reasonable guess of the cause of the transport path changes is the change of the convection field. Indeed, as shown in figure 6-2g, the averaged solar wind electric field does decrease slightly in 2005 and has a bigger drop in 2006-2009. However, Ruohoniemi [65] showed that there is little dependence of the mean convection pattern and value of the cross polar potential drop on the solar cycle. However, his study did not include this particular solar cycle. Further study on convection during this solar cycle may confirm our hypothesis. Similarly, the solar wind pressure, shown in figure 6-2d does not seem responsible for the transport path changes either since it does not have a clear dependence on the solar cycle, e.g. the averaged pressure did not decrease with the solar cycle declining phase.

To sum up, we have observed a clear decrease of the O^+ occurrence frequency from the solar maximum to the solar minimum of solar cycle 23 and a slightly return at the start of solar cycle 24. The decrease is especially dramatic in the tail lobe compared with in the polar cap. The distribution function over the polar cap has decreased as well during the solar cycle declining phase and the decrease is stronger for O^+ at low energy than at high energy. Because the magnetic flux tube volume is larger in the tail lobes than the polar cap due to the less strong magnetic field, the flux of the streaming O^+ is diluted in the tail lobes. As a result the distribution function decrease in the polar cap will lead to a larger effect in the tail lobes, which makes a large amount of O^+ fall below the energy flux threshold in the tail lobes in the later years. However, a quantitative comparison shows that this effect is not strong enough to explain the dramatic decease of the streaming O^+ in the tail lobes in the later years. A close look at the transport path changes for O^+ of different energies during different years shows that the transport path of the streaming O^+ has changed in a sense that O^+ from the north cusp tends to convect more upward and O^+ from the south cusp move more and more sunward. This is true for O^+ at all energy ranges. Although the question about what is the cause of this change of the transport path is still open, in this study we have concluded that O^+ from the cusp does not reach the

near-Earth lobe anymore in the solar minimum time, which will reduce their possibility of entering the near-Earth plasmasheet so they cannot feed the ring current effectively.

Chapter 7

SUMMARY

We have performed statistical studies on the transport path of O^+ from the cusp. In this chapter, we will briefly summarize all the important discoveries from those studies and their significance in improving our scientific understandings of magnetospheric dynamics.

7.1 Spatial Distribution of Streaming O^+

We used data from CLUSTER CIS/CODIF from Mar 2001 to Dec 2002 to study the transport path of O^+ from the dayside cusp/cleft to the plasma sheet under solar maximum conditions. We found that: (1) streaming O^+ is very common in the polar cap and tail lobes at all times; (2) the occurrence frequency of the O^+ is highest during storm main phase, and lowest during non-storm times; (3) IMF B magnitude is the main driver that brings O^+ from the cusp to the near-Earth tail lobes; (4) there is an overall asymmetry in the transport path in which ions in the north are transported towards dawn while ions in the south are transported towards dusk, which is partly controlled by IMF B_y. The asymmetry is strongest for positive IMF B_y, becomes symmetric for weakly negative IMF B_y, and reverses, at least in the north, for strongly negative IMF B_y. IMF B_z does not have a strong effect on the transport path. The effects of IMF B_y and B_z are consistent with configuration of the open field lines found in an empirical model (T04s). Both the asymmetric convection driven by IMF B_y and the lack of mirror symmetry, have been observed in the convection over the polar cap. They have been attributed to effects of the day-night gradient in the ionospheric conductivity, combined with the IMF B_y driven effect. The observations of the O^+ in the northern hemisphere are consistent with the polar

cap convection patterns. However in the southern hemisphere, the strongest asymmetry in the O^+ is observed for IMF B_y positive, while for the polar cap convection, the strongest asymmetry is observed for IMF B_y negative. This indicates there may be other causes for the symmetry breaking, in addition to the day-night conductivity gradient. This part of study has been published in [48].

7.2   Acceleration along the Transport Path

Comparisons between the O^+ cusp outflow distribution and the distribution function of the observed streaming O^+ during nonstorm and storm time shows there is no significant acceleration from the cusp to the polar cap and to the tail lobes during nonstorm times but some acceleration is required for the streaming O^+ observed during storm time. Streaming O^+ observed in the PSBL with energies from 500eV to 7keV, however, do requires a strong velocity increase. Further investigation of the acceleration mechanism of the O^+ in the PSBL shows that large $E \times B$ drift due to the enhanced electric field in the PSBL is the primary cause of the increased velocity of O^+. The perpendicular electric field is also shown as another possible candidate for the acceleration mechanism when O^+ enters the PSBL. Other acceleration mechanisms such as wave heating may also contribute.

7.3   Solar Cycle Dependence

The occurrence frequency of O^+ outflow from the dayside cusp decreased both over the polar cap and in the lobes during the declining phase of the solar cycle. However, the occurrence frequency dropped much more dramatically in the tail lobe compared with in the polar cap region. While the flux of the outflow is expected to decrease during the declining phase, this change in the flux level is not enough to explain the dramatic reduction of the lobe O^+. The most likely reason for the greater reduction in the lobe, compared to over the polar cap, is that the transport path has changed due to the reduced convection electric field. There were some indications in the spatial distributions of the observed O^+ that there is

a change in the predominant transport paths consistent with a reduced convection electric field, but we were not able to conclusively show the reason for it. Nevertheless, the flux of the outflow decreases significantly during the declining phase of the solar cycle, and in addition, we find that the outflow has reduced access to the near-earth tail. This in turn would impact the access of O^+ to the ring current region during solar minimum.

7.4 Importance

We have studied an aspect of magnetospheric dynamics that was not well understood before: the transport of the O^+ from the cusp, to the polar cap, to the tail lobes and into the plasmasheet through the PSBL. This statistical study provides comprehensive information about the spatial distribution of the streaming O^+ inside the polar cap and the tail lobes, as well as in the plasmasheet, which shows how ionospheric ions populate the magnetosphere. This information will be useful for validating the models of global magnetospheric dynamics. The determination of the drivers that control the outflow and the transport path improves our understanding of geomagnetic storm development. Acceleration of O^+ from the cusp to the polar cap, tail lobes and then the PSBL was studied. The findings clarified that most of the energetic O^+ beams observed in the tail lobes are not due to acceleration, but are due to the velocity filter effect. The discovery that the most significant acceleration occurs in moving from the lobe to the PSBL is important new information for understanding how the hot plasmasheet is formed. The discovery of the transport path change from the solar maximum to the solar minimum may help explain the dramatic reduction in the ionospheric content of the magnetosphere during solar minimum times. Overall, this study has improved our understanding of many different aspects of magnetosphere physics.

LIST OF REFERENCES

[1] ABE, T., WATANABE, S., WHALEN, B. A., YAU, A. W., AND SAGAWA, E. Observations of polar wind and thermal ion outflow by Akebono/SMS. *J. Geomagn. Geoelectr 48* (1996), 319 325.

[2] ATKINSON, G., AND HUTCHISON, D. Effect of the day night ionospheric conductivity gradient on polar cap convective flow. *J. Geophys. Res. 83* (Feb. 1978), 725-729.

[3] BAKER, D. N., FRITZ, T. A., BIRN, J., LENNARTSSON, W., WILKEN, B., AND KROEHL, H. W. The role of heavy ionospheric ions in the localization of substorm disturbances on March 22, 1979 - CDAW 6. *J. Geophys. Res. 90* (Feb. 1985), 1273-1281.

[4] BAKER, D. N., HONES, JR., E. W., YOUNG, D. T., AND BIRN, J. The possible role of ionospheric oxygen in the initiation and development of plasma sheet instabilities. *Geophys. Res. Lett. 9* (Dec. 1982), 1337-1340.

[5] BALOGH, A., CARR, C. M., ACUÑA, M. H., DUNLOP, M. W., BEEK, T. J., BROWN, P., FORNAÇON, K.-H., GEORGESCU, E., GLASSMEIER, K.-H., HARRIS, J., MUSMANN, G., ODDY, T., AND SCHWINGENSCHUH, K. The Cluster Magnetic Field Investigation: overview of in-flight performance and initial results. *Annales Geophysicae 19* (Oct. 2001), 1207-1217.

[6] BOUHRAM, M., KLECKER, B., MIYAKE, W., RÈME, H., SAUVAUD, J., MALINGRE, M., KISTLER, L., AND BLAGAU, A. On the altitude dependence of transversely heated O distributions in the cusp/cleft. *Annales Geophysicae 22* (May 2004), 1787-1798.

[7] BOUHRAM, M., KLECKER, B., PASCHMANN, G., RÈME, H., BLAGAU, A., KISTLER, L., PUHL-QUINN, P., AND SAUVAUD, J. Multipoint analysis of the spatio-temporal coherence of dayside O+ outflows with Cluster. *Annales Geophysicae 22* (July 2004), 2507-2514.

[8] BÜCHNER, J., AND ZELENY, L. M. Deterministic chaos in the dynamics of charged particles near a magnetic field reversal. *Physics Letters A 118* (Nov. 1986), 395-399.

[9] CHEN, Y., LIU, L., AND WAN, W. Does the $F_{10.7}$ index correctly describe solar EUV flux during the deep solar minimum of 2007-2009? *Journal of Geophysical Research (Space Physics) 116*, A15 (Apr. 2011), A04304.

[10] CLADIS, J. B. Parallel acceleration and transport of ions from polar ionosphere to plasma sheet. *Geophys. Res. Lett. 13* (Sept. 1986), 893-896.

[11] CLADIS, J. B., AND FRANCIS, W. E. Distribution in magnetotail of o^+ ions from cusp/cleft ionosphere: A possible substorm trigger. *J. Geophys. Res. 97*, A1 (1992), 123-130.

[12] COLE, K. D. Effects of crossed magnetic and (spatially dependent) electric fields on charged particle motion. *Planetary and Space Science 24*, 5 (1976), 515 - 518.

[13] COWLEY, S. W. H. Magnetospheric asymmetries associated with the y-component of the IMF. *Planetary and Space Science 29* (Jan. 1981), 79-96.

[14] COWLEY, S. W. H., MORELLI, J. P., AND LOCKWOOD, M. Dependence of convective flows and particle precipitation in the high-latitude dayside ionosphere on the X and Y components of the interplanetary magnetic field. *J. Geophys. Res. 96* (Apr. 1991), 5557–5564.

[15] CULLY, C. M., DONOVAN, E. F., YAU, A. W., AND ARKOS, G. G. Akebono/Suprathermal Mass Spectrometer observations of low-energy ion outflow: Dependence on magnetic activity and solar wind conditions. *Journal of Geophysical Research (Space Physics) 108* (Feb. 2003), 1093.

[16] DAGLIS, I. A. *The Role of Magnetosphere-Ionosphere Coupling in Magnetic Storm Dynamics.* American Geophysical Union, 1997, pp. 107–+.

[17] DAGLIS, I. A., AND AXFORD, W. I. Fast ionospheric response to enhanced activity in geospace: Ion feeding of the inner magnetotail. *J. Geophys. Res. 101* (Mar. 1996), 5047–5066.

[18] DELCOURT, D. C., CHAPPELL, C. R., MOORE, T. E., AND WAITE, JR., J. H. A three-dimensional numerical model of ionospheric plasma in the magnetosphere. *J. Geophys. Res. 94* (Sept. 1989), 11893–11920.

[19] EASTMAN, T. E., FRANK, L. A., AND HUANG, C. Y. The boundary layers as the primary transport regions of the earth's magnetotail. *J. Geophys. Res. 90* (Oct. 1985), 9541–9560.

[20] ELLIOTT, H. A., COMFORT, R. H., CRAVEN, P. D., CHANDLER, M. O., AND MOORE, T. E. Solar wind influence on the oxygen content of ion outflow in the high-altitude polar cap during solar minimum conditions. *J. Geophys. Res. 106* (Apr. 2001), 6067–6084.

[21] ENGWALL, E., ERIKSSON, A. I., CULLY, C. M., ANDRÉ, M., PUHL-QUINN, P. A., VAITH, H., AND TORBERT, R. Survey of cold ionospheric outflows in the magnetotail. *Annales Geophysicae 27* (Aug. 2009), 3185–3201.

[22] FAIRFIELD, D. H. On the average configuration of the geomagnetic tail. *J. Geophys. Res. 84* (May 1979), 1950–1958.

[23] FRANK, L. A. On the extraterrestrial ring current during geomagnetic storms. *J. Geophys. Res. 72*, 15 (1967), 3753–3767.

[24] FUSELIER, S. A., GHIELMETTI, A. G., MOORE, T. E., COLLIER, M. R., QUINN, J. M., WILSON, G. R., WURZ, P., MENDE, S. B., FREY, H. U., JAMAR, C., GERARD, J.-C., AND BURCH, J. L. Ion outflow observed by IMAGE: Implications for source regions and heating mechanisms. *Geophys. Res. Lett. 28* (Mar. 2001), 1163–1166.

[25] GOSLING, J. T., BAKER, D. N., BAME, S. J., FELDMAN, W. C., AND SMITH, E. J. North-south and dawn-dusk plasma asymmetries in the distant tail lobes - ISEE 3. *J. Geophys. Res. 90* (July 1985), 6354–6360.

[26] GUSTAFSSON, G., ANDRÉ, M., CAROZZI, T., ERIKSSON, A. I., FÄLTHAMMAR, C.-G., GRARD, R., HOLMGREN, G., HOLTET, J. A., IVCHENKO, N., KARLSSON, T., KHOTYAINTSEV, Y., KLIMOV, S., LAAKSO, H., LINDQVIST, P.-A., LYBEKK, B., MARKLUND, G., MOZER, F., MURSULA, K., PEDERSEN, A., POPIELAWSKA, B., SAVIN, S., STASIEWICZ, K., TANSKANEN, P., VAIVADS, A., AND WAHLUND, J.-E. First results of electric field and density observations by Cluster EFW based on initial months of operation. *Annales Geophysicae 19* (Oct. 2001), 1219–1240.

[27] HAALAND, S., PASCHMANN, G., FÖRSTER, M., QUINN, J., TORBERT, R., VAITH, H., PUHL-QUINN, P., AND KLETZING, C. Plasma convection in the magnetotail lobes: statistical results from Cluster EDI measurements. *Annales Geophysicae 26* (Aug. 2008), 2371–2382.

[28] HAALAND, S. E., PASCHMANN, G., FÖRSTER, M., QUINN, J. M., TORBERT, R. B., MCILWAIN, C. E., VAITH, H., PUHL-QUINN, P. A., AND KLETZING, C. A. High-latitude plasma convection from Cluster EDI measurements: method and IMF-dependence. *Annales Geophysicae 25* (Feb. 2007), 239–253.

[29] HAMILTON, D. C., GLOECKLER, G., IPAVICH, F. M., WILKEN, B., AND STUEDEMANN, W. Ring current development during the great geomagnetic storm of February 1986. *J. Geophys. Res. 93* (Dec. 1988), 14343–14355.

[30] HARDY, D. A., HILLS, H. K., AND FREEMAN, J. W. Occurrence of the lobe plasma at lunar distance. *J. Geophys. Res. 84* (Jan. 1979), 72–78.

[31] HEPPNER, J. P. Polar-Cap Electric Field Distributions Related to the Interplanetary Magnetic Field Direction. *J. Geophys. Res. 77* (1972), 4877–4887.

[32] HIRAHARA, M., NAKAMURA, M., TERASAWA, T., MUKAI, T., SAITO, Y., YAMAMOTO, T., NISHIDA, A., MACHIDA, S., AND KOKUBUN, S. Acceleration and heating of cold ion beams in the plasma sheet boundary layer observed with GEOTAIL. *Geophys. Res. Lett. 21* (Dec. 1994), 3003–3006.

[33] HOLZWORTH, R., AND MENG, C.-I. Auroral boundary variations and the interplanetary magnetic field. *Planetary and Space Science 32*, 1 (1984), 25 – 29.

[34] HORWITZ, J. L. The tail lobe ion spectrometer. *J. Geophys. Res. 91* (May 1986), 5689–5699.

[35] HORWITZ, J. L., AND LOCKWOOD, M. The cleft ion fountain - A two-dimensional kinetic model. *J. Geophys. Res. 90* (Oct. 1985), 9749–9762.

[36] KING, J. H., AND PAPITASHVILI, N. E. Solar wind spatial scales in and comparisons of hourly Wind and ACE plasma and magnetic field data. *Journal of Geophysical Research (Space Physics) 110* (Feb. 2005), A02104.

[37] KISTLER, L. M., GALVIN, A. B., POPECKI, M. A., SIMUNAC, K. D. C., FARRUGIA, C., MOEBIUS, E., LEE, M. A., BLUSH, L. M., BOCHSLER, P., WURZ, P., KLECKER, B., WIMMER-SCHWEINGRUBER, R. F., OPITZ, A., SAUVAUD, J.-A., THOMPSON, B., AND RUSSELL, C. T. Escape of O^+ through the distant tail plasma sheet. *Geophys. Res. Lett. 372* (Nov. 2010), L21101.

[38] KISTLER, L. M., IPAVICH, F. M., HAMILTON, D. C., GLOECKLER, G., AND WILKEN, B. Energy spectra of the major ion species in the ring current during geomagnetic storms. *J. Geophys. Res. 94* (Apr. 1989), 3579–3599.

[39] KISTLER, L. M., MOEBIUS, E., BAUMJOHANN, W., PASCHMANN, G., AND HAMILTON, D. C. Pressure changes in the plasma sheet during substorm injections. *J. Geophys. Res. 97* (Mar. 1992), 2973–2983.

[40] KISTLER, L. M., MOUIKIS, C., MÖBIUS, E., KLECKER, B., SAUVAUD, J. A., RÉME, H., KORTH, A., MARCUCCI, M. F., LUNDIN, R., PARKS, G. K., AND BALOGH, A. Contribution of nonadiabatic ions to the cross-tail current in an O^+ dominated thin current sheet. *Journal of Geophysical Research (Space Physics) 110*, A9 (June 2005), A06213.

[41] KISTLER, L. M., MOUIKIS, C. G., CAO, X., FREY, H., KLECKER, B., DANDOURAS, I., KORTH, A., MARCUCCI, M. F., LUNDIN, R., MCCARTHY, M., FRIEDEL, R., AND LUCEK, E. Ion composition and pressure changes in storm time and nonstorm substorms in the vicinity of the near-Earth neutral line. *Journal of Geophysical Research (Space Physics) 111*, A10 (Nov. 2006), A11222.

[42] KISTLER, L. M., MOUIKIS, C. G., KLECKER, B., AND DANDOURAS, I. Cusp as a source for oxygen in the plasma sheet during geomagnetic storms. *Journal of Geophysical Research (Space Physics) 115*, A14 (Mar. 2010), A03209.

[43] KIVELSON, M., AND RUSSELL, C. *Introduction to space physics*. Cambridge atmospheric and space science series. Cambridge University Press, 1995.

[44] KORTH, A., FRIEDEL, R. H. W., MOUIKIS, C. G., FENNELL, J. F., WYGANT, J. R., AND KORTH, H. Comprehensive particle and field observations of magnetic storms at different local times from the CRRES spacecraft. *J. Geophys. Res. 105* (Aug. 2000), 18729–18740.

[45] LE, G., RUSSELL, C. T., GOSLING, J. T., AND THOMSEN, M. F. ISEE observations of low-latitude boundary layer for northward interplanetary magnetic field: Implications for cusp reconnection. *J. Geophys. Res. 101* (Dec. 1996), 27239–27250.

[46] LENNARTSSON, O. W. Tail lobe ion composition at energies of 0.1 to 16 kev/e: Evidence for mass-dependent density gradients. *J. Geophys. Res. 99*, A2 (1994), 2387–2401.

[47] LI, W., RAEDER, J., THOMSEN, M. F., AND LAVRAUD, B. Solar wind plasma entry into the magnetosphere under northward imf conditions. *J. Geophys. Res. 113*, A4 (04 2008).

[48] LIAO, J., KISTLER, L. M., MOUIKIS, C. G., KLECKER, B., DANDOURAS, I., AND ZHANG, J. C. Statistical study of o+ transport from the cusp to the lobes with cluster codif data. *J. Geophys. Res. 115* (12 2010).

[49] LINDSTEDT, T., KHOTYAINTSEV, Y. V., VAIVADS, A., ANDRÉ, M., NILSSON, H., AND WAARA, M. Oxygen energization by localized perpendicular electric fields at the cusp boundary. *Geophys. Res. Lett. 37* (May 2010), L09103.

[50] LOCKWOOD, M., WAITE, JR., J. H., MOORE, T. E., CHAPPELL, C. R., AND CHANDLER, M. O. The cleft ion fountain. *J. Geophys. Res. 90* (Oct. 1985), 9736–9748.

[51] MAGGIOLO, R., SAUVAUD, J. A., FONTAINE, D., TESTE, A., GRIGORENKO, E., BALOGH, A., FAZAKERLEY, A., PASCHMANN, G., DELCOURT, D., AND RÈME, H. A multi-satellite study of accelerated ionospheric ion beams above the polar cap. *Annales Geophysicae 24* (July 2006), 1665–1684.

[52] MOORE, T. E., CHAPPELL, C. R., CHANDLER, M. O., CRAVEN, P. D., GILES, B. L., POLLOCK, C. J., BURCH, J. L., YOUNG, D. T., WAITE, JR., J. H., NORDHOLT, J. E., THOMSEN, M. F., McCOMAS, D. J., BERTHELIER, J. J., WILLIAMSON, W. S., ROBSON, R., AND MOZER, F. S. High-altitude observations of the polar wind. *Science 277* (July 1997), 349–351.

[53] MOORE, T. E., PETERSON, W. K., RUSSELL, C. T., CHANDLER, M. O., COLLIER, M. R., COLLIN, H. L., CRAVEN, P. D., FITZENREITER, R., GILES, B. L., AND POLLOCK, C. J. Ionospheric mass ejection in response to a CME. *Geophys. Res. Lett. 26* (Aug. 1999), 2339–2342.

[54] MOSES, J. J., GORNEY, D. J., SISCOE, G. L., AND CROOKER, N. U. IMF B_y and day-night conductivity effects in the expanding polar cap convection model. *J. Geophys. Res. 92* (Feb. 1987), 1193–1198.

[55] NILSSON, H., ENGWALL, E., ERIKSSON, A., PUHL-QUINN, P. A., AND ARVELIUS, S. Centrifugal acceleration in the magnetotail lobes. *Annales Geophysicae 28* (Feb. 2010), 569–576.

[56] NILSSON, H., WAARA, M., MARGHITU, O., YAMAUCHI, M., LUNDIN, R., RÈME, H., SAUVAUD, J.-A., DANDOURAS, I., LUCEK, E., KISTLER, L. M., KLECKER, B., CARLSON, C. W., BAVASSANO-CATTANEO, M. B., AND KORTH, A. An assessment of the role of the centrifugal acceleration mechanism in high altitude polar cap oxygen ion outflow. *Annales Geophysicae 26* (Feb. 2008), 145–157.

[57] NODA, H., BAUMJOHANN, W., NAKAMURA, R., TORKAR, K., PASCHMANN, G., VAITH, H., PUHL-QUINN, P., FÖRSTER, M., TORBERT, R., AND QUINN, J. M. Tail lobe convection observed by Cluster/EDI. *Journal of Geophysical Research (Space Physics) 108* (July 2003), 1288.

[58] NOSÉ, M., TAGUCHI, S., HOSOKAWA, K., CHRISTON, S. P., McENTIRE, R. W., MOORE, T. E., AND COLLIER, M. R. Overwhelming O^+ contribution to the plasma sheet energy density during the October 2003 superstorm: Geotail/EPIC and IMAGE/LENA observations. *Journal of Geophysical Research (Space Physics) 110*, A9 (Aug. 2005), A09S24.

[59] ORSINI, S., CANDIDI, M., STOCKHOLM, M., AND BALSIGER, H. Injection of ionospheric ions into the plasma sheet. *J. Geophys. Res. 95* (June 1990), 7915–7928.

[60] PEDERSEN, A., KNOTT, K., CATTELL, C. A., MOZER, F. S., FALTHAMMAR, C.-G., LINDQVIST, P.-A., AND MANKA, R. H. Electric fields in the plasma sheet and plasma sheet boundary layer. *J. Geophys. Res. 90* (Feb. 1985), 1231–1242.

[61] PETERSON, W. K., ANDERSSON, L., CALLAHAN, B., ELKINGTON, S. R., WINGLEE, R. W., SCUDDER, J. D., AND COLLIN, H. L. Geomagnetic activity dependence of O^+ in transit from the ionosphere. *Journal of Atmospheric and Solar-Terrestrial Physics 71* (Nov. 2009), 1623–1629.

[62] PETERSON, W. K., COLLIN, H. L., LENNARTSSON, O. W., AND YAU, A. W. Quiet time solar illumination effects on the fluxes and characteristic energies of ionospheric outflow. *Journal of Geophysical Research (Space Physics) 111*, A10 (Sept. 2006), A11S05.

[63] RÈME, H., AOUSTIN, C., BOSQUED, J. M., DANDOURAS, I., LAVRAUD, B., SAUVAUD, J. A., BARTHE, A., BOUYSSOU, J., CAMUS, T., COEUR-JOLY, O., CROS, A., CUVILO, J., DUCAY, F., GARBAROWITZ, Y., MEDALE, J. L., PENOU, E., PERRIER, H., ROMEFORT, D., ROUZAUD, J., VALLAT, C., ALCAYDÉ, D., JACQUEY, C., MAZELLE, C., D'USTON, C., MÖBIUS, E., KISTLER, L. M., CROCKER, K., GRANOFF, M., MOUIKIS, C., POPECKI, M., VOSBURY, M., KLECKER, B., HOVESTADT, D., KUCHAREK, H., KUENNETH, E., PASCHMANN, G., SCHOLER, M., SCKOPKE, N., SEIDENSCHWANG, E., CARLSON, C. W., CURTIS, D. W., INGRAHAM, C., LIN, R. P., McFADDEN, J. P., PARKS, G. K., PHAN, T., FORMISANO, V., AMATA, E., BAVASSANO-CATTANEO, M. B., BALDETTI, P., BRUNO, R., CHIONCHIO, G., DI LELLIS, A., MARCUCCI, M. F., PALLOCCHIA, G., KORTH, A., DALY, P. W., GRAEVE, B., ROSENBAUER, H., VASYLIUNAS, V., McCARTHY, M., WILBER, M., ELIASSON, L., LUNDIN, R., OLSEN, S., SHELLEY, E. G., FUSELIER, S., GHIELMETTI, A. G., LENNARTSSON, W., ESCOUBET, C. P., BALSIGER, H., FRIEDEL, R., CAO, J.-B., KOVRAZHKIN, R. A., PAPAMASTORAKIS, I., PELLAT, R., SCUDDER, J., AND SONNERUP, B. First multispacecraft ion measurements in and near the Earth's magnetosphere with the identical Cluster ion spectrometry (CIS) experiment. *Annales Geophysicae 19* (Oct. 2001), 1303–1354.

[64] RUOHONIEMI, J. M., AND GREENWALD, R. A. Statistical patterns of high-latitude convection obtained from Goose Bay HF radar observations. *J. Geophys. Res. 101* (Oct. 1996), 21743–21764.

[65] RUOHONIEMI, J. M., AND GREENWALD, R. A. Dependencies of high-latitude plasma convection: Consideration of interplanetary magnetic field, seasonal, and universal time

factors in statistical patterns. *Journal of Geophysical Research (Space Physics) 110*, A9 (Sept. 2005), A09204.

[66] SAITO, Y., MUKAI, T., TERASAWA, T., NISHIDA, A., MACHIDA, S., HIRAHARA, M., MAEZAWA, K., KOKUBUN, S., AND YAMAMOTO, T. Slow-mode shocks in the magnetotail. *J. Geophys. Res. 100* (Dec. 1995), 23567–23582.

[67] SEKI, K., ELPHIC, R. C., THOMSEN, M. F., BONNELL, J., LUND, E. J., HIRAHARA, M., TERASAWA, T., AND MUKAI, T. Cold flowing O^+ beams in the lobe/mantle at Geotail: Does FAST observe the source? *J. Geophys. Res. 105* (July 2000), 15931–15944.

[68] SEKI, K., HIRAHARA, M., TERASAWA, T., MUKAI, T., SAITO, Y., MACHIDA, S., YAMAMOTO, T., AND KOKUBUN, S. Statistical properties and possible supply mechanisms of tailward cold o^+ beams in the lobe/mantle regions. *J. Geophys. Res. 103*, A3 (1998), 4477–4489.

[69] SEKI, K., TERASAWA, T., HIRAHARA, M., AND MUKAI, T. Quantification of tailward cold O^+ beams in the lobe/mantle regions with Geotail data: Constraints on polar O^+ outflows. *J. Geophys. Res. 1032* (Dec. 1998), 29371–29382.

[70] SHARP, R. D., CARR, D. L., PETERSON, W. K., AND SHELLEY, E. G. Ion streams in the magnetotail. *J. Geophys. Res. 86* (June 1981), 4639–4648.

[71] TANAKA, T. Interplanetary magnetic field B_y and auroral conductance effects on high-latitude ionospheric convection patterns. *J. Geophys. Res. 106* (Nov. 2001), 24505–24516.

[72] TSYGANENKO, N. A., AND SITNOV, M. I. Modeling the dynamics of the inner magnetosphere during strong geomagnetic storms. *Journal of Geophysical Research (Space Physics) 110*, A9 (Mar. 2005), A03208.

[73] VILLANTE, U. Neutral sheet observations at 1000 earth radii. *J. Geophys. Res. 81* (Jan. 1976), 212–215.

[74] WEIMER, D. R. Models of high-latitude electric potentials derived with a least error fit of spherical harmonic coefficients. *J. Geophys. Res. 100* (Oct. 1995), 19595–19608.

[75] WEIMER, D. R. Maps of ionospheric field-aligned currents as a function of the interplanetary magnetic field derived from Dynamics Explorer 2 data. *J. Geophys. Res. 106* (July 2001), 12889–12902.

[76] WINGLEE, R. M. Circulation of ionospheric and solar wind particle populations during extended southward interplanetary magnetic field. *Journal of Geophysical Research (Space Physics) 108* (Oct. 2003), 1385.

[77] YAU, A. W., AND ANDRÉ, M. Sources of ion outflow in the high latitude ionosphere. *Space Science Reviews 80* (1997), 1–25. 10.1023/A:1004947203046.

[78] YAU, A. W., PETERSON, W. K., AND SHELLEY, E. G. Quantitative parametrization of energetic ionospheric ion outflow. *Washington DC American Geophysical Union Geophysical Monograph Series* (1988), 211–217.

[79] ZHANG, J.-C., KISTLER, L. M., MOUIKIS, C. G., MATSUI, H., KLECKER, B., DANDOURAS, I., AND DUNLOP, M. W. Shock-driven variation in ionospheric outflow during the 11 October 2001 moderate storm. *Journal of Geophysical Research (Space Physics) 116*, A15 (Jan. 2011), A00J18.